EMISSION FROM HOT GAS IN PRE-MAIN SEQUENCE OBJECTS: THE ACCRETION SHOCK AND THE INNER DISK

by

Laura D. Ingleby

A dissertation submitted in partial fulfillment
of the requirements for the degree of
Doctor of Philosophy
(Astronomy and Astrophysics)
in The University of Michigan
2012

Doctoral Committee:

Professor Nuria Calvet, Chair
Professor Fred Adams
Professor Edwin Bergin
Professor Lee Hartmann
Associate Professor Jon Miller

ACKNOWLEDGMENTS

This thesis was made possible by invaluable contributions from collaborators, most significantly from my thesis advisor, Nuria Calvet. Under her guidance I learned the practices of a professional astronomer and how to be successful in tasks from publishing my research to making important contacts in the community. I am thankful for her support during my graduate career and her positive influence over the last few years. I would also like to thank my committee members, Ted Bergin, Jon Miller, Lee Hartmann and Fred Adams for their feedback and help in shaping my thesis.

Among my collaborators, I would like to thank Cesar Briceno, Gregory Herczeg, Catherine Espaillat, Jesus Hernandez, Melissa McClure and Lucia Adame in particular, for supplementing my education on observing and data analysis techniques. In addition, I would also like to acknowledge my co-authors for providing valuable comments and suggestions to help improve published papers; including, Herve Abgrall, Richard Alexander, David Ardila, Thomas Bethell, Alexander Brown, Joanna Brown, John Carpenter, Nathan Crockett, Suzan Edwards, Kevin France, Jeffrey Fogel, Scott Gregory, Lynne Hillenbrand, Gaitee Hussain, Christopher Johns-Krull, Jeffrey Linsky, Michael Meyer, Ilaria Pascucci, Evelyne Roueff, Jeff Valenti, Frederick Walter, Hao Yang and Ashwin Yerasi.

This thesis was supported in part by the University of Michigan's Rackham One Term Dissertation Fellowship. Funding was also provided by NASA grants for the Guest Observer program (GO-08317, 09081, 09374, 011145, 11616 and 12211) to the University of Michigan and Chandra Awards GO8-9028X and GO8-9029X issued by the Chandra X-ray Observatory Center, which is operated by the Smithsonian Astrophysical Observatory for and on behalf of NASA under contract NAS8-03060.

CONTENTS

LIST OF FIGURES

Figure

LIST OF TABLES

Table

ABSTRACT

High energy (X-ray and ultraviolet) emission traces hot gas produced by energetic phenomena in T Tauri stars. These phenomena include magnetic heating of the stellar atmosphere and magnetospheric accretion of disk gas onto the stellar surface. High energy emission irradiates the planet-forming disk during a key time for the origin of planets, so an understanding of these energetic processes and their evolution is crucial for theories of disk evolution and planet formation

In this thesis, I analyze X-ray and ultraviolet observations of young stars to study high energy events and follow their evolution. I confirm that X-ray emission is saturated during the T Tauri phase and suggest that far ultraviolet emission is also saturated at this age, possibly because the same mechanism heats both the chromosphere and corona.

I compare accretion diagnostics for a large sample of T Tauri stars to characterize the properties of magnetospheric accretion. For the first time, I use models of the accretion emission which have contributions from multiple accretion hot spots, characterized by varying energy fluxes in the accretion columns. Models of T Tauri magnetospheres and the magnetic footprints on the star physically motivate this multi-component description of accretion.

For RECX-11, a source near the final stage of disk depletion, I show that it has a very low mass accretion rate. If theories that predict the circumstellar disk is losing mass at very high rates are correct, the disk of RECX-11 would have a gap or hole in it, which it does not.

I also present observations of hot H_2 gas in the inner circumstellar disk. I find that the strength of the H_2 emission is correlated with the accretion luminosity of the T Tauri star and show that for young stars in which accretion has ceased, there

is no H_2 left in the inner disk. I show this is true even for non-accreting young stars at 1–3 Myr, indicating rapid disk removal.

Observations of circumstellar gas, combined with knowledge of the radiation fields, are crucial for studying disk evolution. Here, I provide timescales for gas depletion and constraints to disk dissipation models.

CHAPTER 1

Introduction

The study of young stars and the disks which surround them is important for understanding the timescales and environments in which planets may form. Theories of star formation agree on a general picture which starts with a large molecular cloud, in which there is a region with a density enhancement (Shu et al., 1987; Evans, 1999). The enhancement grows to form a cloud core which then collapses under its own gravity until a central object exists surrounded by an envelope of gas and dust. Because the molecular cloud core has some initial angular momentum which must be conserved during the infall process, most of the material generally is not accreted directly onto the star, but arrives first on a disk and then flows through the disk toward the star. The structure of the innermost regions of the disk are complicated by the presence of strong stellar magnetic fields in young stars (Johns-Krull et al., 2000). The field lines truncate the inner disk; at this point gas is lifted from the disk and channeled onto the star along the magnetic field lines (Uchida & Shibata, 1984), a process referred to as magnetospheric accretion (see Figure 1.1). At the stellar surface, the free-falling material, moving at 200–300 km/s, forms an accretion shock which irradiates the infalling material and the star below. As a result, the accretion shock emits high energy radiation, which peaks in the ultraviolet or UV (Calvet & Gullbring, 1998).

Young stars are classified based on their evolutionary status in two main ways, either by the properties of the circumstellar matter, or by the state of accretion onto the star. First, sources are split into Class I - Class III, based on their infrared (IR) spectral energy distributions (SED). Figure 1.2, based on work by Adams et al. (1987), indicates what the IR SED looks like for each stage of star formation. Class I objects

are heavily obscured by the dusty, infalling envelope material and, therefore, have a spectrum peaked at far-IR wavelengths ($\sim$100–200 μm) understood if the infalling $\sim$10K envelope is heated by the accretion luminosity of the protostar (Adams & Shu, 1985). As the envelope is either accreted or dissipated due to radiation from the protostar, the star becomes visible and the source becomes a Class II object, where the spectrum is a composite of the stellar photosphere and the emission from a dusty circumstellar disk, observed as a near to mid-IR excess, between 10 and 100 μm (Calvet et al., 1994). Class III objects have little to no IR excess; IR fluxes are photospheric, indicating that any initial disk material has been accreted onto the star, into planets, or dispersed. Quantitatively, the Class of an object is defined by the slope, $\alpha = \delta\log(\lambda F_\lambda)/\delta\log(\lambda)$, of the IR spectrum between two wavelengths, initially 2.2 and 25 μm, with $-2 < \alpha < 0$ for Class II objects and $\alpha < -2$ for Class III objects (Kenyon & Hartmann, 1995).

In the second classification, based on the status of accretion onto the star, pre-main sequence objects are separated into accreting, or Classical T Tauri stars (CTTS), and non-accreting, or weak T Tauri stars (WTTS). Conventionally, a source is identified as a CTTS or a WTTS based on the strength of its Hα emission. In absence of accretion from the disk, Hα emission from the chromosphere is often detected. The emission is relatively weak and narrow in velocity (see LkCa 7 in Figure 1.3). When accretion is actively occurring the Hα emission can be strongly enhanced and have a large velocity width of order of free-fall speeds (Muzerolle et al., 1998b). Classically, CTTS and WTTS were distinguished based on an Hα equivalent width, EW(Hα), cutoff at 10 Å, with the higher EW(Hα) indicating accretion. It was later shown that this cutoff is spectral type dependent and larger EW(Hα) are needed to indicate accretion in later type stars (White & Basri, 2003). Alternatively, the width of Hα at 10% of the maximum flux may act as a discriminator between CTTS and WTTS (White & Basri, 2003). The large, free-fall velocities of the accreting material result in widths in the Hα wings of hundreds of km/s for CTTS. The boundary between CTTS and WTTS differs between studies, with values from 200 – 270 km/s (Natta et al., 2004; White & Basri, 2003), so there is still some ambiguity where the transition

occurs. Almost always, a CTTS is also a Class II object and a WTTS is a Class III object, even though the definitions were derived independently. WTTS may have an IR excess at long wavelengths, past the wavelengths in the IR SED which are used to identify Class II from Class III sources, produced by remaining cool dust in the outer disk (Padgett et al., 2006; Furlan et al., 2006, 2009).

1.1 Origin of High Energy Emission in T Tauri Stars

Constraining the types and strengths of high energy emission is key for the understanding of young stars because it traces hot gas, produced in energetic phenomena like magnetospheric accretion (Uchida & Shibata, 1984; Calvet & Gullbring, 1998). High energy emission is important for understanding disk physics, as it impacts disk chemistry and circumstellar gas evolution. The disk chemistry involved in the formation and longevity of water in protoplanetary disks is of great interest to those looking for the presence of life in other planetary systems. The characteristics of the far UV (FUV) spectrum between 912 and 2000 Å, most importantly Lyα line emission, determine whether or not water can survive in the disk, with both dissociation rates and the probability of shielding dependent on the FUV luminosities (Bergin et al., 2003; Bethell & Bergin, 2009). X-rays are also an important driver of disk chemistry because they are a strong source of ionization and play a role in destroying molecules (Najita et al., 2011). Furthermore, high energy radiation affects the disk because, as will be discussed in Section 1.3.2, it is likely responsible for mass loss from the disk through photoevaporation, important for the final evolution of the circumstellar disk.

1.1.1 X-rays from T Tauri stars

X-ray emission is commonly divided into two energy regimes, the hard and soft X-rays, separated at about 10 keV. For T Tauri stars, we typically study the soft X-rays, which have contributions from both the stellar corona and the accretion shock (Günther et al., 2007; Dupree et al., 2012). Fast rotating T Tauri stars have strong magnetic fields, produced by the dynamo mechanism, which heat the coronal plasma to temperatures >10–20 MK (Preibisch & Feigelson, 2005). The accretion related

X-rays are produced in the shock itself; the shocked gas is heated to ∼1 MK and emits soft X-rays into the post and pre-shock regions (Calvet & Gullbring, 1998; Argiroffi et al., 2011; Brickhouse et al., 2010). It is typically assumed that they are completely absorbed in the pre-shock material (see Figure 1.4); however, lower density accretion columns may allow some of the soft X-rays to escape. Figure 1.5 shows the XMM-Newton X-ray spectrum of the nearest, well studied CTTS, TW Hya. Günther et al. (2007) modeled the X-ray spectrum with both coronal and accretion shock components and found that the corona dominates at higher energies than the shock, >1 keV. Robrade & Schmitt (2006) compared the shape of the X-ray spectrum for four young stars and found that TW Hya was the only source with X-ray emission dominated by accretion while the others were dominated by coronal X-ray production (Figure 1.6). However, even the sources which are dominated by coronal X-ray emission have evidence for accretion related X-rays observed as an enhanced O VII/O VIII ratio, with O VII produced in the post-shock plasma, compared to WTTS and main sequence stars (Güdel & Telleschi, 2007; Brickhouse et al., 2010).

1.1.2 Ultraviolet Emission from T Tauri stars

The UV spectrum of pre-main sequence stars has contributions from the accretion shock, the stellar chromosphere and gas in the inner circumstellar disk. It is often difficult to disentangle these three components; however, recent high spectral resolution UV instruments have allowed for significant advances. The UV spectrum can be divided into three spectral regions, the extreme UV (EUV) at wavelengths <1200 Å, the far UV (FUV) between 1200 and 2000 Å and the near UV (NUV) at wavelengths from 2000 to 4000 Å. Each spectral region reveals interesting properties of the T Tauri star and disk system; however, the EUV is nearly impossible to observe because it is easily absorbed by interstellar hydrogen. Even though it is not well constrained, theories predict that EUV emission may be a significant contributor to the mechanism driving disk dispersal through photoevaporation (Clarke et al., 2001; Alexander et al., 2006).

NUV emission has several contributions, mainly the active stellar chromosphere

and the accretion shock. Similar to the corona which produces X-rays, the chromosphere of a young star is heated by the strong magnetic fields and short rotation periods characteristic of pre-main sequence objects. Typical rotation periods are on the order of a few days, compared to ∼25 days for the Sun's equator, and magnetic field strengths are a few kG (Johns-Krull et al., 2000). The increased activity of the chromosphere is observed as an NUV excess over a dwarf star photosphere (Houdebine et al., 1996) as well as through lines in emission which are typically in absorption for main sequence stars (e.g. Hα and the Ca II infrared triplet). The peak of the accretion shock emission is in the UV, specifically the NUV; decreasing quickly toward shorter wavelengths (Calvet & Gullbring, 1998). Therefore, the NUV is the easiest spectral region to observe the shock continuum excess for late type stars, after the excess from the active chromosphere has been accounted for, because the stellar photospheric emission is not strong (Figure 1.7), except when extinction along the line of sight to the star is very high, making the UV emission hard to detect.

Contributions to the FUV spectrum include H_2 emission along with hot lines and continuum emission produced in the accretion shock and chromosphere. Figure 1.8 shows the rich spectrum of H_2 in the FUV, contributing to both the lines and adding emission through H_2 dissociation to the FUV continuum (Bergin et al., 2004). Lyα is responsible for much of the H_2 emission, producing a fluorescent H_2 spectrum (Herczeg et al., 2002). From the observed H_2 line ratios in TW Hya, it was found that the H_2 is hot, ∼2500 K and because it is spatially unresolved, it must be close to the star, within a few AU (Herczeg et al., 2004). Bergin et al. (2004) also showed that H_2 may be excited by free electrons in the disk, producing a unique FUV spectrum. FUV emission lines like C IV and He II have contributions from the accretion shock, evidenced from broad line wings, tracing fast moving material in the accretion flows (Ardila et al., 2002, Figure 1.9).

1.2 Evolution of High Energy Emission

The early phases of pre-main sequence evolution are characterized by high energy phenomena like magnetospheric accretion and strong magnetic fields; exceeding the

activity levels of older dwarf stars. Compared to the Sun and other main sequence stars, it is clear that as young stars evolve, the high energy radiation decays, with the highest energy fields decreasing the fastest (Ribas et al., 2005, Figure 1.10). Based on the contributors to the high energy emission discussed above, we can understand that some of the decline comes from the spin down of pre-main sequence stars. The magnetic activity-rotation relation shows that as the rotation period of the star lengthens, indicators of magnetic activity (like coronal and chromospheric emission) decline, after an initial saturation period (Wright et al., 2011). As activity diminishes, the heating of the chromosphere and corona will become less important and we observe this as a decay in the X-ray luminosity with age (Preibisch & Feigelson, 2005; Mercer et al., 2009). Although ongoing energetic flares may temporarily increase a source's X-ray luminosity during the X-ray luminosity decay period, these flares occur only a few percentage of the time (Stelzer et al., 2000). Whether or not the observed luminosity decay for the X-rays is the case for the chromospheric UV emission is unclear, as UV observations of WTTS are significantly rarer than X-ray.

Also, accretion is expected to decrease as the star ages and the reservoir of circumstellar disk material available to accrete declines. Figure 1.11 shows that older sources have lower mass accretion rates (Calvet et al., 2005), with typical values around 10^{-8} $M_\odot\,yr^{-1}$ at 1 Myr and 10^{-10} $M_\odot\,yr^{-1}$ by 10 Myr. Furthermore, Fedele et al. (2010) showed that the fraction of accreting sources in a cluster ebbs with age (Figure 1.12). As the accretion rate drops, the contribution to the NUV excess will recede; however, there may be a short time period where soft X-ray emission actually increases due to the ability to escape the lower density accretion columns. Likewise, EUV photons require mass accretion rates $< 10^{-8}$ $M_\odot\,yr^{-1}$ before they may penetrate the accretion columns (Gorti et al., 2009) so there may be a period of enhanced EUV irradiation of the disk.

1.3 Evolution of Circumstellar Disks

As the fraction of accreting sources in a cluster is observed to decline with age, so does the fraction of sources with circumstellar disks, as seen in Figure 1.12 and

Hernández et al. (2007b). The evolution of circumstellar disks has been well studied by following the properties of the dust in the disk (Weidenschilling, 1997; Dullemond & Dominik, 2004). The dust is traced using the shape of the IR SED; the IR fluxes probe dust at different temperatures, corresponding to different radii and heights in the disk. A possible sequence of disk evolution starts with a full disk of gas and dust. As the dust in the disk settles, the scale height of the disk decreases resulting in less IR dust emission (Lada et al., 2006). Models which best fit the IR SEDs include some flaring, where the disk height increases with radius because the internal temperature distribution in the disk falls off as $T_d \propto R^{-1/2}$. In flared disks, the outer disk intercepts more stellar radiation and increases the IR excess when compared to a flat disk (Kenyon & Hartmann, 1987).

After the dust settles in the disk, it may form a pre-transitional disk, which has an SED characterized by IR fluxes which are below the median fluxes for full disks in Taurus in the mid-IR wavelengths (5–20 μm) yet fluxes which are in excess of the photosphere at near-IR (2–5 μm) and at long wavelengths $> 20\mu$m (Espaillat et al., 2010). The characteristics of the pre-transitional SED are understood if there is optically thick material in the inner region of the disk, followed by a gap in the disk which is typically tens of AU in size for the sources which have been detected so far, and finally an outer disk of dust. After further evolution, the optically thick material in the inner disk of the pre-transitional disk is removed, forming a transitional disk, which is seen in the SED as photospheric IR fluxes both in the near and mid-IR, interpreted as an inner disk hole, and dust in the outer disk (Calvet et al., 2002; Espaillat et al., 2008). An example of a transitional disk is shown in Figure 1.13. However, while the dust has provided invaluable insight into disk evolution, it comprises only 1% of the total disk mass. The rest of the disk mass is in the gas, primarily in H_2; therefore, the mechanism which dissipates gas is key to the evolution of circumstellar disks. Several mechanisms have been suggested for dissipating the disk, including planet formation and photoevaporation by high energy emission from the central star.

1.3.1 Planet Formation

There are several processes in the disk which have been used to explain the switch from full to pre-transitional disks, and one possible mechanism is planet formation. After the disk forms and the dust settles, a planet may form in the disk. Once there, the planet will accrete material in its vicinity, clearing a gap (Artymowicz & Lubow, 1994; Paardekooper & Mellema, 2004) and forming a pre-transitional disk. Espaillat et al. (2010) showed that other types of disk dissipation mechanisms proceed in an inside - out direction instead of forming a gap, making planet formation the most likely way to form a pre-transitional disk. Though a gap is formed in the dust, gas is still able to flow through the gap, though at a diminished rate (Zhu et al., 2011), indicating that the planet is not efficiently clearing disk gas. Observations show that pre-transitional disks have large gaps and accretion rates similar to full disks. According to Zhu et al. (2011), it is possible to open the large gaps using multiple planets, but the mass accretion rate would drop well below the observed values, so these sources are still difficult to describe with planets.

1.3.2 Photoevaporation

Photoevaporation is the most promising mechanism for dispersing the gas in the outer circumstellar disk. While external irradiation of the disk by massive nearby stars in clusters may contribute to the gas dispersal (Adams et al., 2004), here we focus on the irradiation of the disk by the central star which dominates in distributed populations of young stars like the Taurus Molecular Cloud. The theory assumes that high energy radiation from the star and accretion shock irradiate the disk, heating the gas until it has enough energy to escape the potential well and leaves the system in an outflow (Shu et al., 1993). As the source evolves and the accretion rate through the disk decreases, eventually the mass loss rate due to photoevaporation exceeds the mass accretion rate and material can no longer flow toward the star, forming a gap in the disk (Clarke et al., 2001). After the gap is formed, the inner disk is no longer replenished and accretes quickly onto the star leaving an inner cleared disk (Alexander et al., 2006). Owen et al. (2012a) showed that, for low mass stars, once

the inner disk is accreted, the outer disk is exposed to more direct radiation from the star and is eroded in short timescales.

The details of photoevaporation depend on the type of emission which is responsible for the mass loss and possibilities include EUV only, X-ray + EUV or FUV emission (Clarke et al., 2001; Font et al., 2004; Alexander et al., 2006; Owen et al., 2010, 2012a; Gorti et al., 2009; Gorti & Hollenbach, 2009). Figure 1.14 shows the region in the disk where the mass loss peaks, assuming each type of photoevaporation is more efficient at different disk radii. As indicated in Figure 1.14 the photoevaporative flow has velocities of tens of km/s and evidence for this flow has been seen in blue-shifted forbidden line emission (Pascucci et al., 2011), so while it is accepted that photoevaporation is occurring, there are controversies over the actual mechanisms at play. Early models of EUV photoevaporation predicted low mass loss rates of $\sim 10^{-10}$ $M_{\odot}\,yr^{-1}$ (Clarke et al., 2001; Alexander et al., 2006) but recent models including X-ray and FUV emission find mass loss rates up to 100× higher than for the EUV photoevaporation models (Gorti & Hollenbach, 2009; Owen et al., 2010).

The actual values of mass loss rates will have important implications for not only disk dispersal but also for planet formation. If extremely high mass loss rates are ongoing during circumstellar disk evolution, a larger initial disk mass may be needed to explain the survival of disks. For example, by 1 Myr, a disk which has been exposed to photoevaporation at rates of 10^{-8} $M_{\odot}\,yr^{-1}$ will have already lost ∼0.01 $M_{\odot}$, representing 10 to 100% of initial disk masses (Eisner, 2012). If circumstellar gas is dispersed too quickly, it is not available to complete its role in circularizing planetary orbits (Kominami & Ida, 2002); however, Matsuyama et al. (2003) showed that removing the gas may be necessary to stop planetary migration into the star, so there may be an ideal time period for the gas to be completely removed. To constrain the evolution of the circumstellar disk and its planets, better understanding of the gas properties and the mechanisms involved in gas dissipation is needed.

1.4 Summary of Thesis

In this thesis, we expand upon the wealth of knowledge regarding high energy emission in T Tauri stars, described in previous sections. We approach these topics primarily by assembling large samples of objects to study the general properties of high energy processes in T Tauri stars, but in some cases we focus on interesting individual sources to test an idea or concept. The types of sources included are those from well studied star forming regions, like the Taurus Molecular Cloud and the Chamaeleon I star forming region, in addition to those from the large population of sources in the Orion OB1 association (Briceño et al., 2001, Figure 1.15). In general, the regions we focus on contain a distributed population of low mass stars and have little extinction, necessary for observing the UV.

In Chapter 2, we observe the evolution of high energy radiation fields, specifically X-ray and FUV, for a large sample of young stars in the 1–2 Myr Taurus, 2–3 Myr Chamaeleon I, 7–10 Myr 25 Ori aggregate and $\sim$ 10 Myr TW Hydra star forming regions, including a population of older pre-main sequence objects between 10 and 100 Myr. The time period of 1–100 Myr, in particular the first 10 Myr, is an important era for circumstellar disk evolution because during this time period planets are formed, disks are dispersed and accretion ends. Observations include new X-ray data of the 7–10 Myr stellar aggregate, 25 Ori, inside the Orion OB1a region, which increases the number of young stellar populations nearing 10 Myr with well characterized X-ray luminosities. Other 8–10 Myr star forming regions, including η Chamaeleon and the TW Hydra association, have small numbers of sources, whereas we observed $\sim$ 40 sources in 25 Ori. The 10 Myr age is interesting for young stars; not only does the X-ray luminosity become un-saturated sometime between 10 and 30 Myr, but it is also the age past when we rarely see sources which are accreting or are surrounded by full disks (Fedele et al., 2010; Hernández et al., 2007b). We show, for the first time, the evolution of FUV radiation between 1 and 100 Myr and compare our observations with the assumptions of FUV photoevaporation models of Gorti et al. (2009) and Gorti & Hollenbach (2009). The decay of FUV radiation can be understood in terms

of accretion; as the mass accretion rate ($\dot{M}$) drops, the shock emission in the FUV does as well. Also, as $\dot{M}$ decreases, there is less gas in the inner disk and less Lyα radiation to illuminate it, so the H_2 contribution to the FUV also declines. This explains why FUV luminosities of non-accretors are $\sim$2 orders of magnitude lower than accretors at the same age. We use a small sample of 10–100 Myr pre-main sequence stars with spectral types similar to the Sun to compare the rate of decay of high energy emission to the rate found for older solar type stars in Ribas et al. (2005) and show that the same decay rate can describe both the sources >1 Gyr and our 10–100 Myr sample.

In Chapter 3 we use the FUV sample discussed in Chapter 2 (comprised of 1–10 Myr CTTS and $\geq$ 10 Myr WTTS and debris disks) but focus on detecting H_2 in the spectra. Using low resolution spectra obtained with the Advanced Camera for Surveys/ Solar Blind Channel (ACS/SBC) PR130L prism, we identify a continuum feature produced when H_2 excited by free electrons dissociates. The strength of this feature is correlated with the accretion luminosity and is absent when the source is no longer accreting. The X-rays needed to produce free electrons with the energies required to excite H_2 are present even in the non-accretors, so we would see the H_2 if present in the disks of WTTS and debris disks. We place very low upper limits on the amount of H_2 that may remain in the inner disks of non-accreting pre-main sequence objects, $< 10^{-7}$ earth masses. Therefore, we show that the inner disk dissipates on timescales consistent with the end of accretion onto the star.

In Chapter 4 we expand upon the results of Chapter 3 where we showed that WTTS and debris disks at $\geq$ 10 Myr lack gas in the inner circumstellar disk. In order to determine if the same is true for younger WTTS, we obtained ACS/SBC PR130L spectra for WTTS in the 1–2 Myr Taurus and the 2–3 Myr Chamaeleon I star forming regions. We found no evidence for remaining H_2, confirming that the presence of inner disk gas is tied to the accretion properties of the source. IR and sub-mm observations show that in addition to the gas, the dust is gone from the disks of these WTTS. While there are several possible explanations for rapid disk dispersal, we explore the possibility of WTTS forming from molecular cloud

cores with very low angular momenta. With initial low angular momentum, envelope material falls onto the disk very close to the star, accreting onto the star in short timescales (Hartmann, 2009). Finally, we show that the FUV luminosity of young stars may saturate at ages similar to the observed saturation of X-ray emission, at a level of $L_{FUV}/L_{bol} = -4.1 \pm 0.1$.

In Chapter 5 we analyze the final stages of accretion and the inner disk by focusing on one source which has a very low mass accretion rate and evidence for evolution of dust in the disk, RECX-11. RECX-11 is in the 5–9 Myr region, η Chamaeleon and was identified as a low accretor from its small EW(Hα) (Jayawardhana et al., 2006). Closer analysis revealed that it has little to no NUV excess when compared to a WTTS of the same spectral type and age, yet FUV spectra showed the presence of H_2 in the disk and, therefore, ongoing accretion. High resolution observations of Hα and near IR He I λ10830 Å are characterized by complex and variable red-shifted absorption features, providing additional evidence for accretion. Assuming that the remaining accretion emission is dwarfed by the active chromosphere, we estimate an upper limit of $\dot{M} \leq 3 \times 10^{-10}$ $M_\odot\,yr^{-1}$. The IR SED of RECX-11 shows evidence that dust has settled, but there is no sign that the disk has a gap or hole in it. If mass loss rates are as high as predicted in recent models of X-ray and FUV photoevaporation, up to 10^{-8} $M_\odot\,yr^{-1}$ (Gorti & Hollenbach, 2009; Owen et al., 2010), RECX-11 would have a gap in the disk and likely the inner disk would have drained onto the star for the 5–9 Myr source. Since we do not see this, photoevaporation at such high rates cannot be occurring; however, photoevaporation at the rates predicted in EUV models, 10^{-10} $M_\odot\,yr^{-1}$ (Clarke et al., 2001; Alexander et al., 2006), cannot be ruled out.

In Chapter 6 we analyze the accretion properties of a large sample of young stars, observed as a part of the large *HST* program (PI: G. Herczeg), the Disks, Accretion and Outflows of T Tau stars (the DAO). The DAO obtained simultaneous *HST* spectra from the FUV to the optical in order to observe the excess emission produced in the accretion shock. WTTS were also observed to use as templates, which is vital for obtaining accurate accretion rates for low accretors. New to this

work, multiple components of the accretion shock described in Calvet & Gullbring (1998) are used to fit the observed spectra, combining hot accretion columns with emission which peaks in the UV and cool columns whose emission peaks in the optical. Two important consequences of these multi-component models are; 1) a better fit to observed red excesses (Edwards et al., 2006; Fischer et al., 2011) and 2) large expected filling factors. Recent models of the magnetospheric region find that accretion shocks should cover a large portion of the stellar surface (Gregory & Donati, 2011; Donati et al., 2008), so these multi-component accretion models are in better agreement with the physical geometry. Using nearly simultaneous estimates of $\dot{M}$ and observations of Hα, it is clear that the EW(Hα) is not an accurate tracer of the accretion rate, although the luminosity of Hα is. Likewise emission lines of Hβ and the Ca II K line are correlated with the accretion properties of the sources, showing that they are good proxies for accretion and may be used when UV excess observations are unavailable. Finally, NUV lines of C II] and Mg II strongly correlate with L_{acc}, indicating an accretion origin, and indeed, C II] is only observed in CTTS.

In Chapter 7 we discuss the main conclusions of this thesis and some steps for future research on this topic.

The material in Chapters 2, 3, 4 and 5 has been published in Ingleby et al. (2011a), Ingleby et al. (2009), Ingleby et al. (2012) and Ingleby et al. (2011b), respectively, and the material Chapter 6 is in preparation for submission to ApJ.

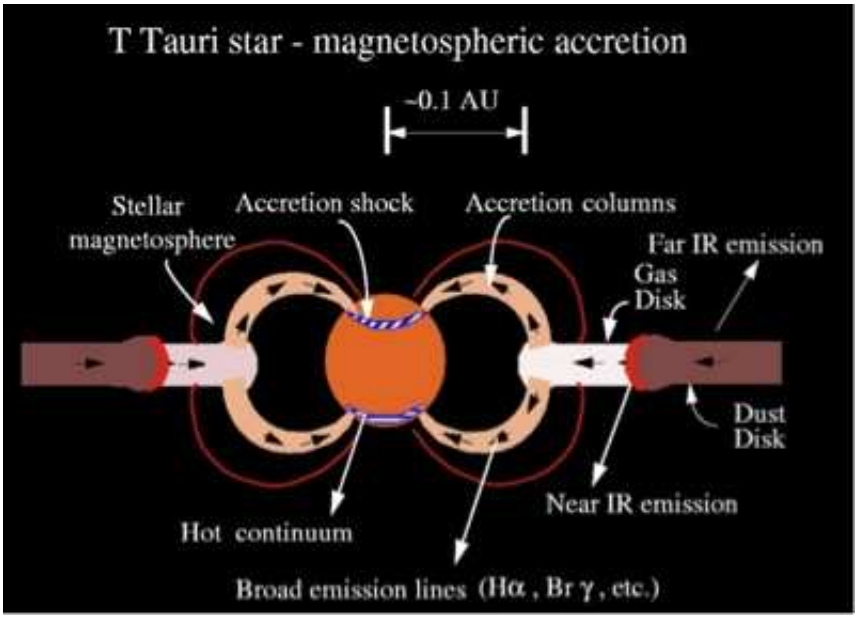

Figure 1.1. Magnetospheric accretion on T Tauri stars. In the current picture of star formation the circumstellar disk is truncated by the stellar magnetic field. The disk gas is accreted along the magnetic field lines, impacting the stellar surface and creating an accretion shock. Figure taken from Hartmann (2001).

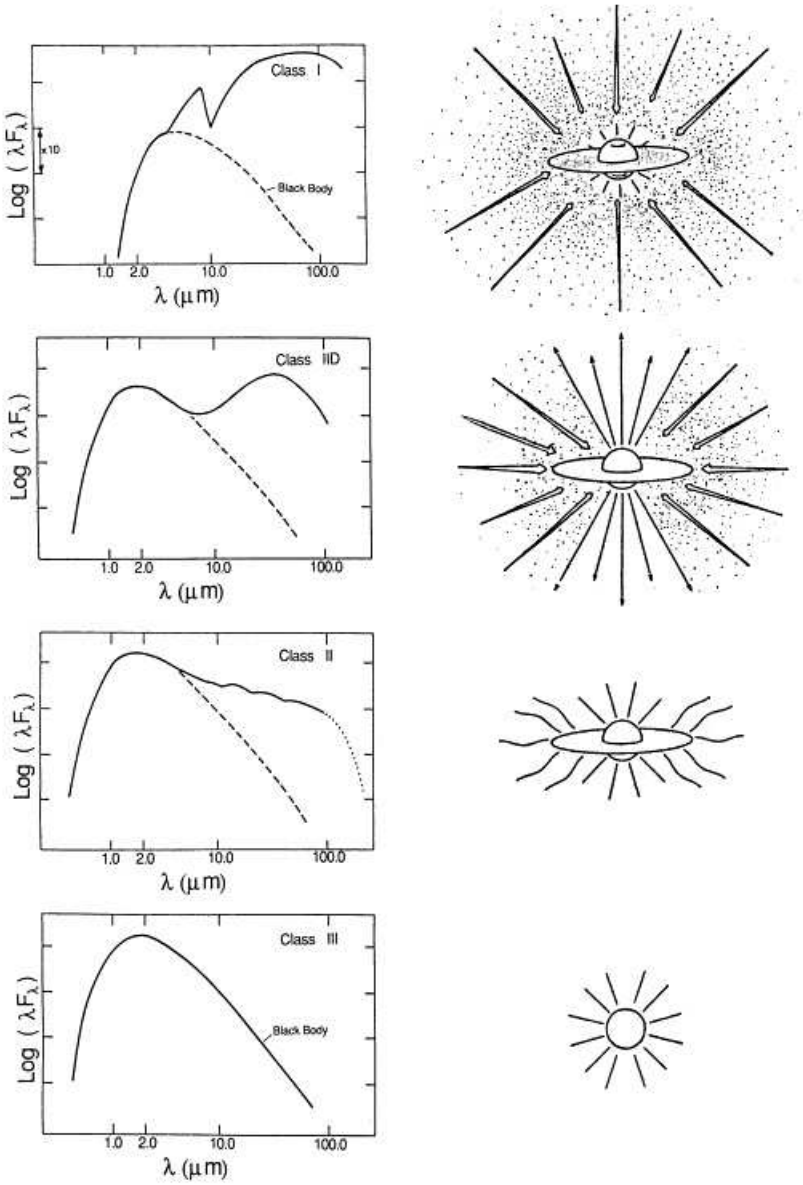

Figure 1.2. Spectral energy distributions for Class I – Class III objects. The panels of the left show the IR SED of young stars during the star formation process. The evolutionary sequence goes from top to bottom with the nature of the object pictured on the right. The evolution between the final two stages (Class II and Class III) is interesting because it represents the dispersal of the circumstellar disk (seen in the SED as a lack of an IR excess in Class III sources). Figure taken from Wilking (1989).

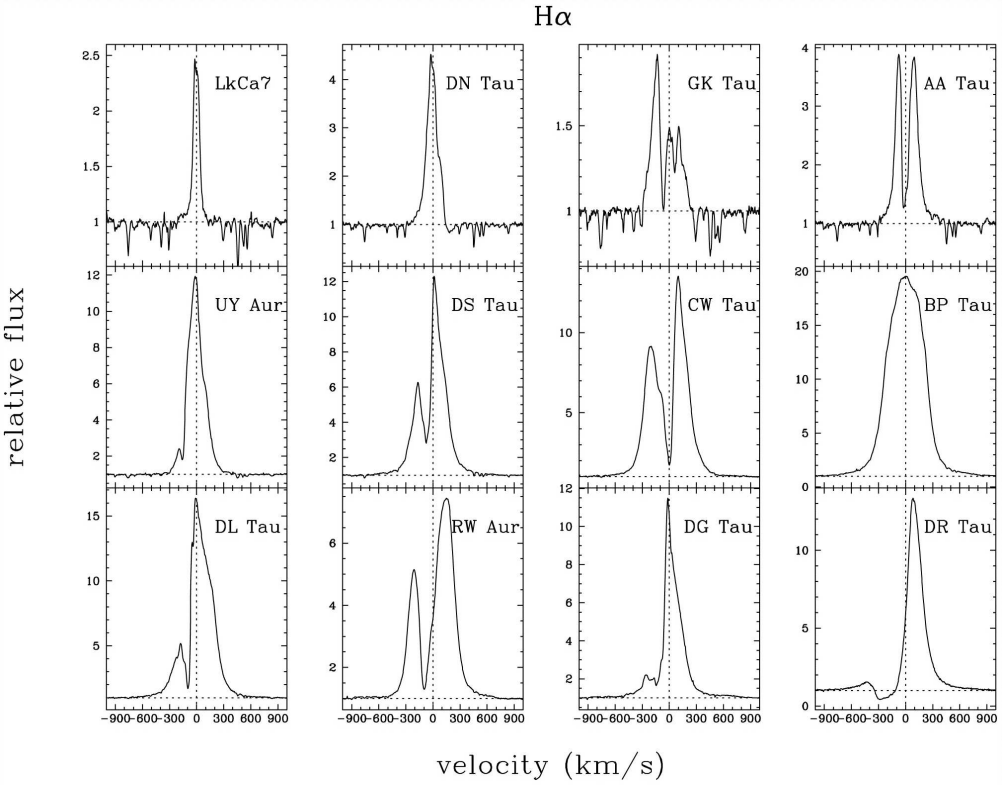

Figure 1.3. Hα profiles of CTTS. The Hα emission from a variety of T Tauri stars is shown. Sources with no accretion have narrow profiles (LkCa 7), whereas strong accretors are characterized by wide, complex line profiles (DR Tau). Figure taken from Muzerolle et al. (1998b).

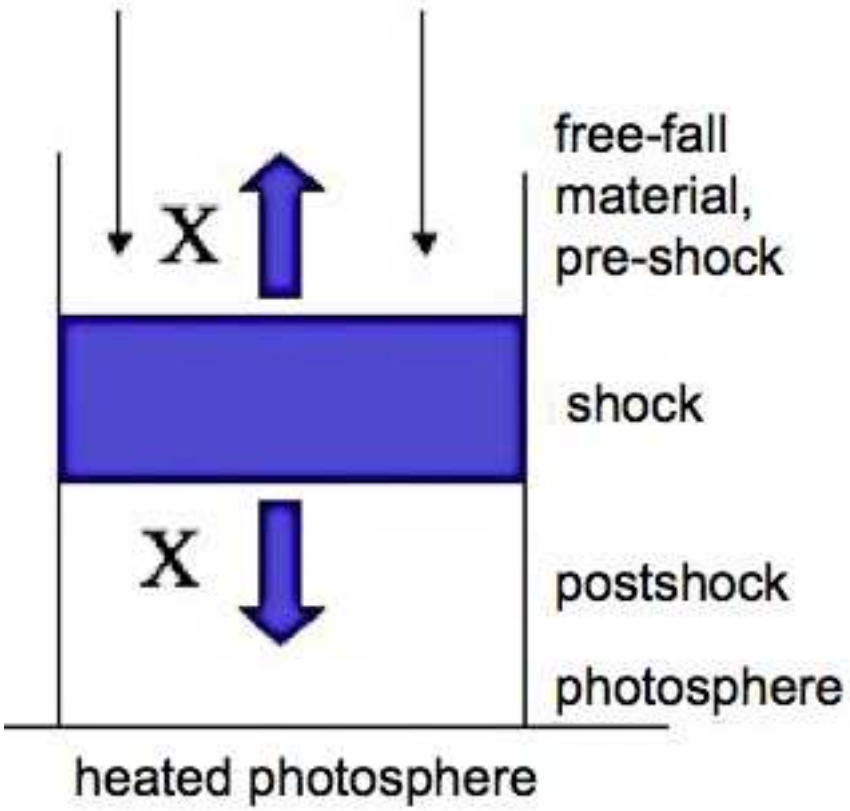

Figure 1.4. Accretion shock geometry. In the simple geometry assumed for the Calvet & Gullbring (1998) accretion shock models, the shock region is assumed to be plane parallel to the star and covering a very small percentage of the stellar surface so that the curvature of the star is not important. The free-falling material forms a shock which emits soft X-rays into the pre- and post-shock regions where they are completely absorbed and re-emitted at UV and optical wavelengths.

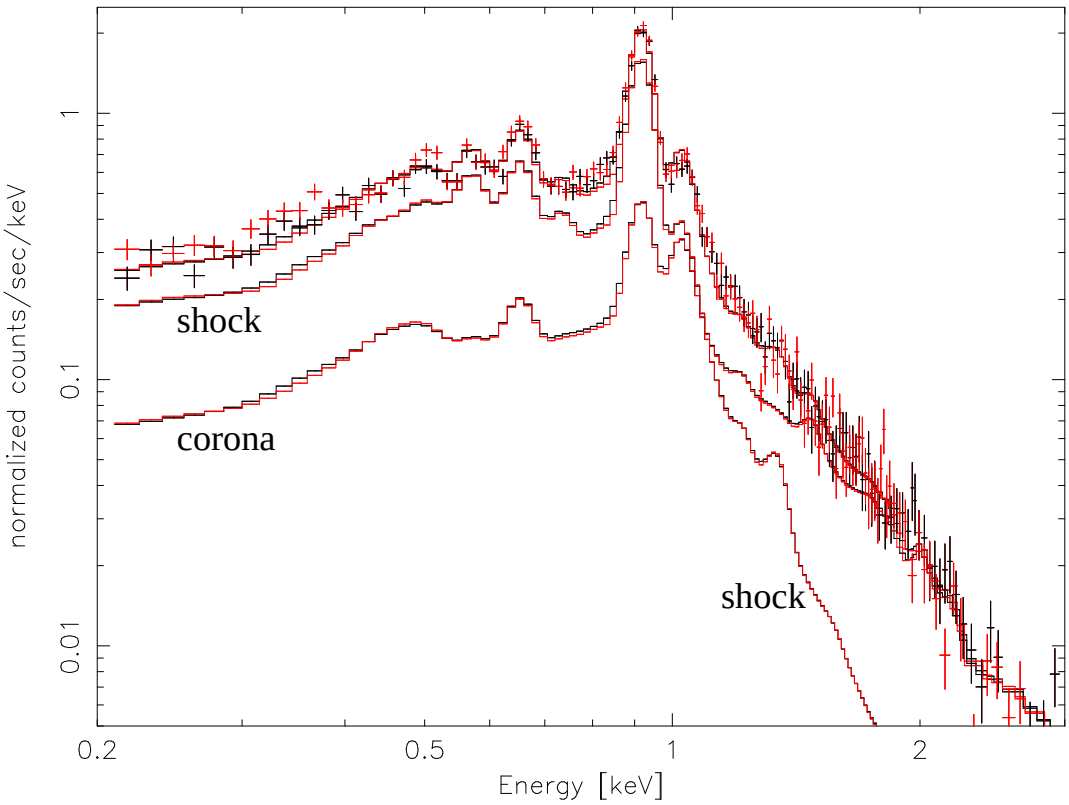

Figure 1.5. XMM Newton X-ray spectrum of TW Hya. The black crosses show the observed XMM-Newton spectrum. The red lines represent shock and coronal X-ray emission. Both components are needed to fit the X-ray spectrum. Figure taken from Günther et al. (2007).

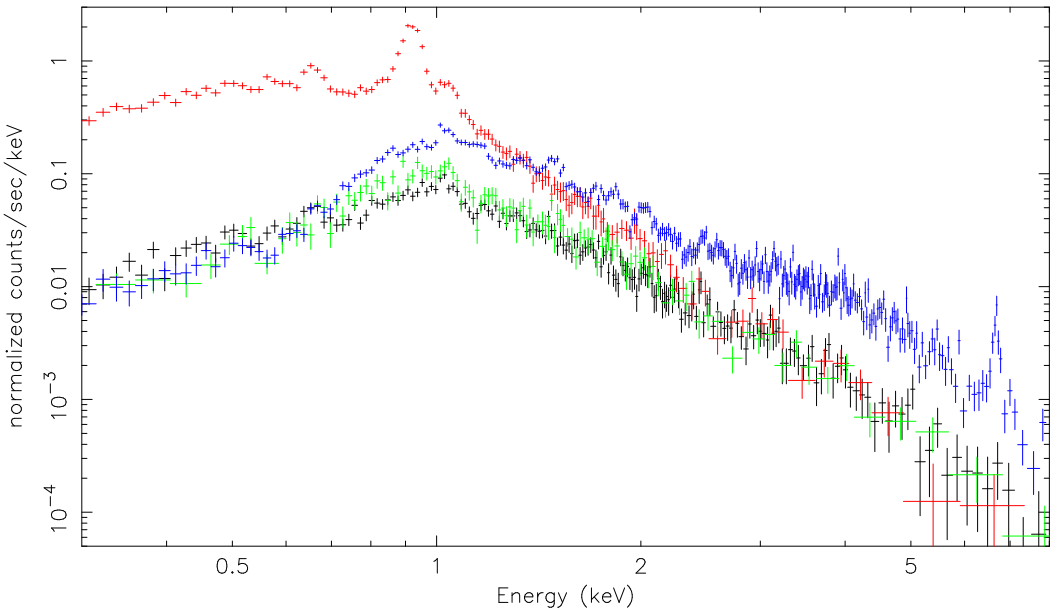

Figure 1.6. XMM Newton X-ray spectra of four CTTS. The X-ray spectra of TW Hya (red), SU Aur (blue), CR Cha (green) and BP Tau (black) exhibit different properties based on whether the emission is dominated by the shock or corona. TW Hya has a soft X-ray excess produced in the shock, whereas SU Aur has a harder X-ray spectrum, typical of coronal emission. Figure taken from Robrade & Schmitt (2006).

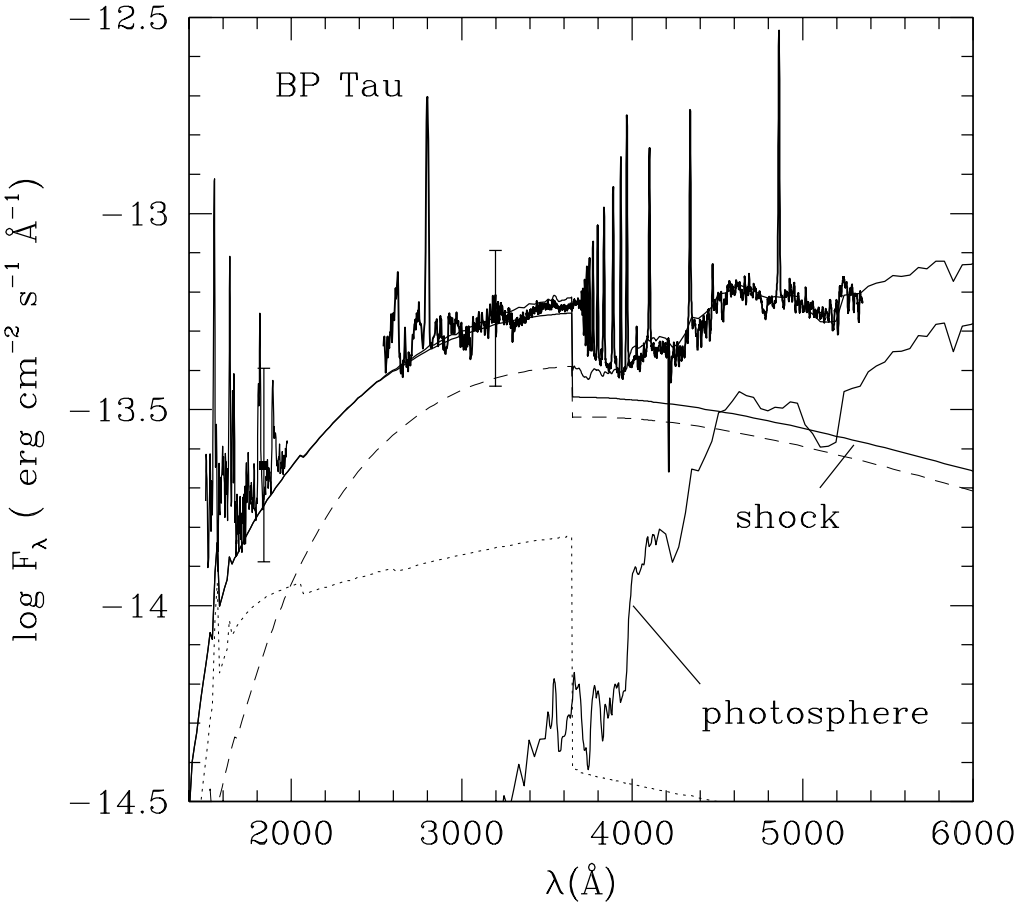

Figure 1.7. Spectrum of the shock excess observed for BP Tau. The IUE spectrum of BP Tau reveals that there is a significant excess over the photosphere in the UV region. The spectrum of the accretion shock accurately describes this excess, providing evidence for magnetospheric accretion. Figure taken from Gullbring et al. (2000).

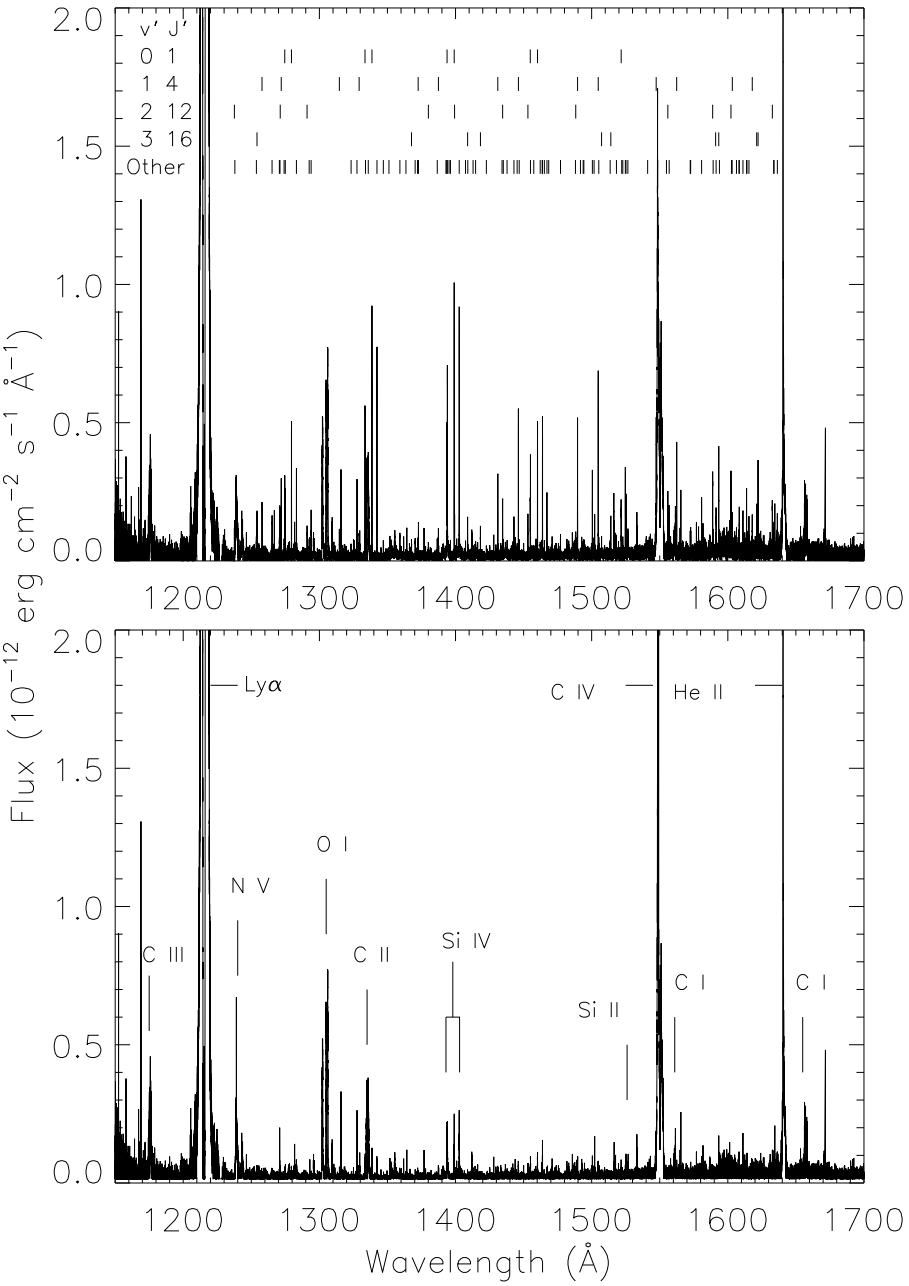

Figure 1.8. FUV spectrum of TW Hya. The top panel shows the full FUV spectrum, with lines of H_2 identified by dash marks. In the bottom panel, the H_2 lines have been removed, demonstrating the prevalence of H_2 emission in the FUV. Figure taken from Herczeg et al. (2002).

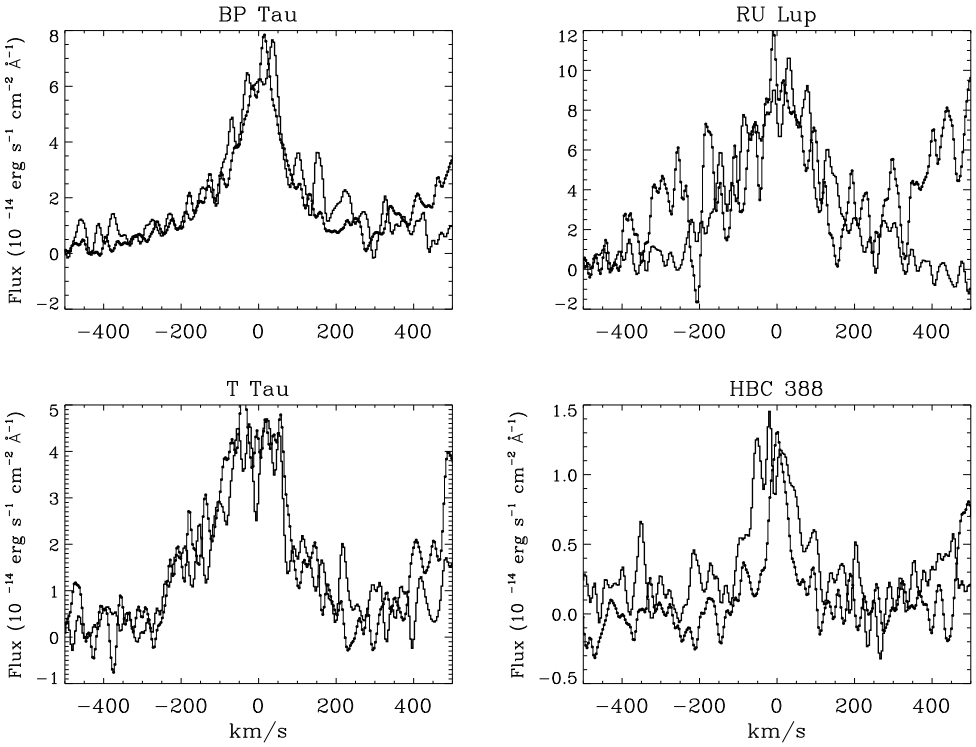

Figure 1.9. FUV emission lines of T Tauri stars. C IV (thick line) and Si IV (thin line) are compared for four T Tauri stars. The broad wings of the lines, extending to several hundred km/s indicate an origin in the accretion flows. Figure taken from Ardila et al. (2002).

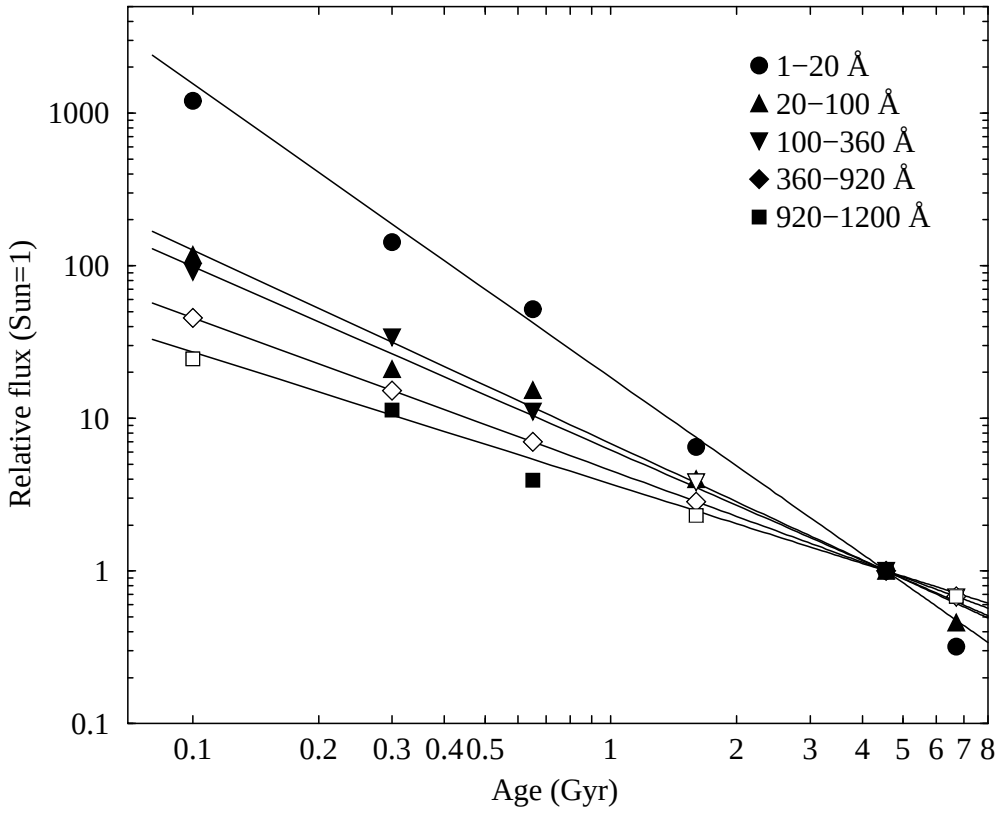

Figure 1.10. Evolution of solar radiation fields. High energy emission for young Sun-like stars, broken into several energy bins, is observed to decay as the source ages. The higher the energy (or shorter the wavelength) of emission, the faster it decays. Figure taken from Ribas et al. (2005).

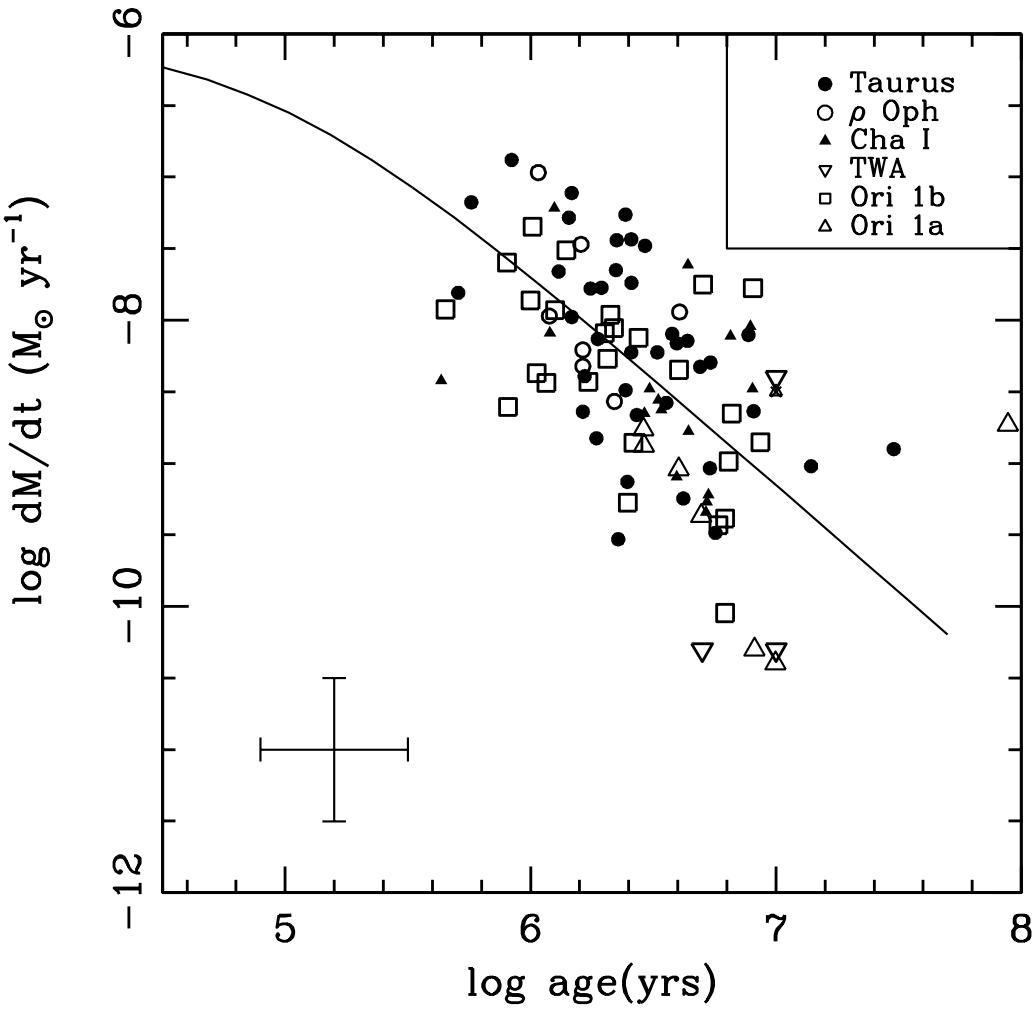

Figure 1.11. Evolution of the mass accretion rate. When comparing accretion rates of sources in star forming regions of different ages, it is observed that the accretion rate decreases with the age of the source. Figure taken from Calvet et al. (2005).

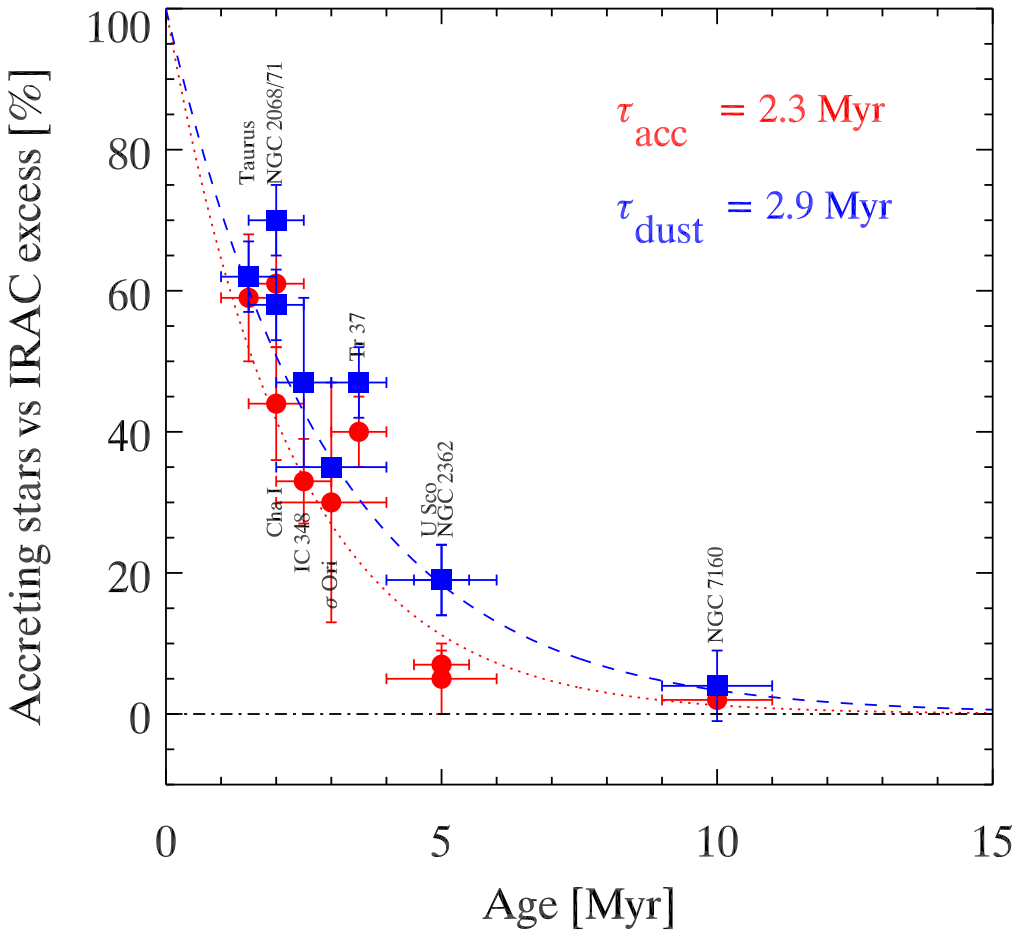

Figure 1.12. Fraction of accreting sources versus age. In addition to the accretion rate declining with age, the number of sources which are accreting in a given region decreases with the age of the stellar association. Figure taken from Fedele et al. (2010).

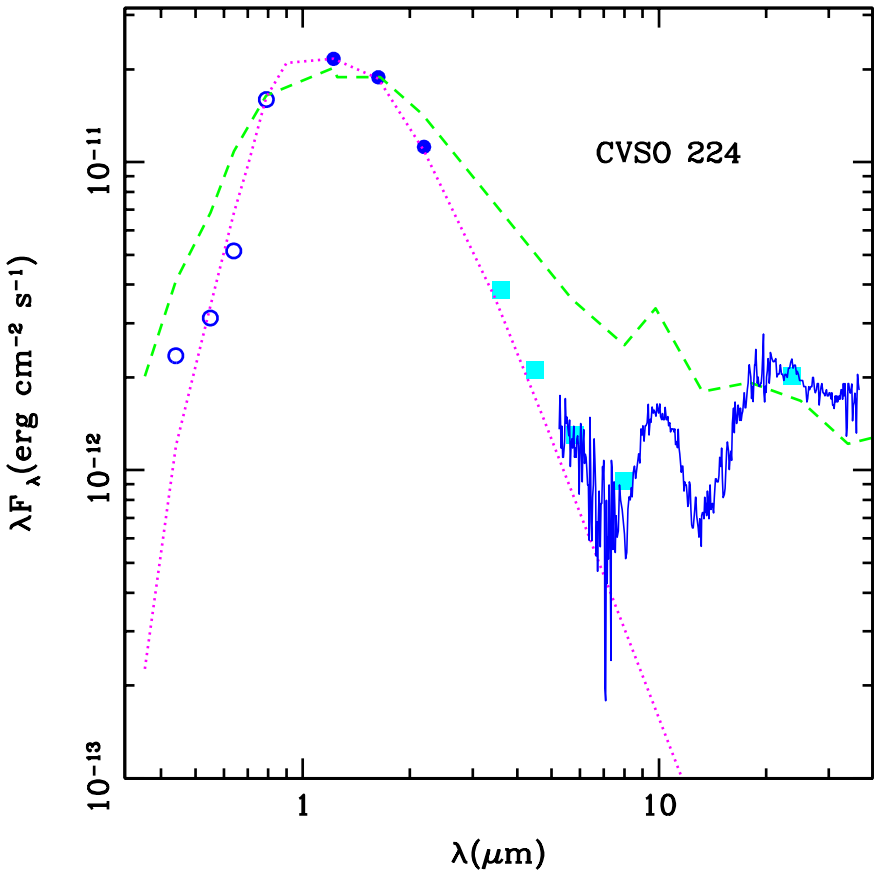

Figure 1.13. SED of a 10 Myr transitional disk. This source was identified as a transitional disk based on IR fluxes from *Spitzer* (cyan points and blue spectrum), which have a deficit when compared to typical fluxes of full disks in taurus (green dashed line). In fact, they are fit by a photospheric spectrum (pink dotted line) at short wavelengths indicating an inner disk hole. Figure taken from Espaillat et al. (2008).

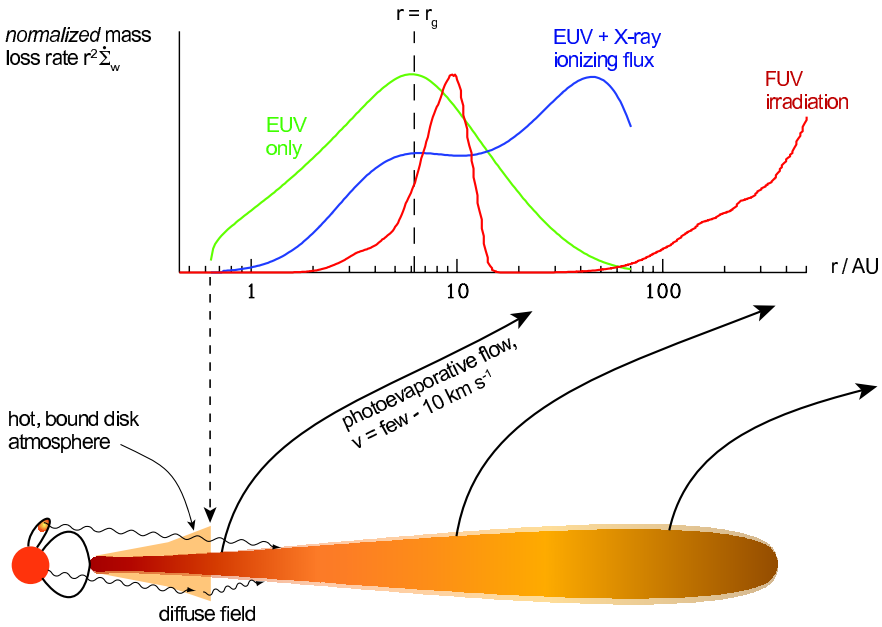

Figure 1.14. Picture of mass loss by photoevaporation. Comparing EUV, EUV + X-ray and FUV photoevaporation models, the region of the disk with the highest mass loss for each model is shown in the top panel. A pictorial description of the process is in the bottom panel, showing an inner bound region to the disk with photoevaporative flows occurring at larger radii in the disk. Figure taken from Armitage (2011).

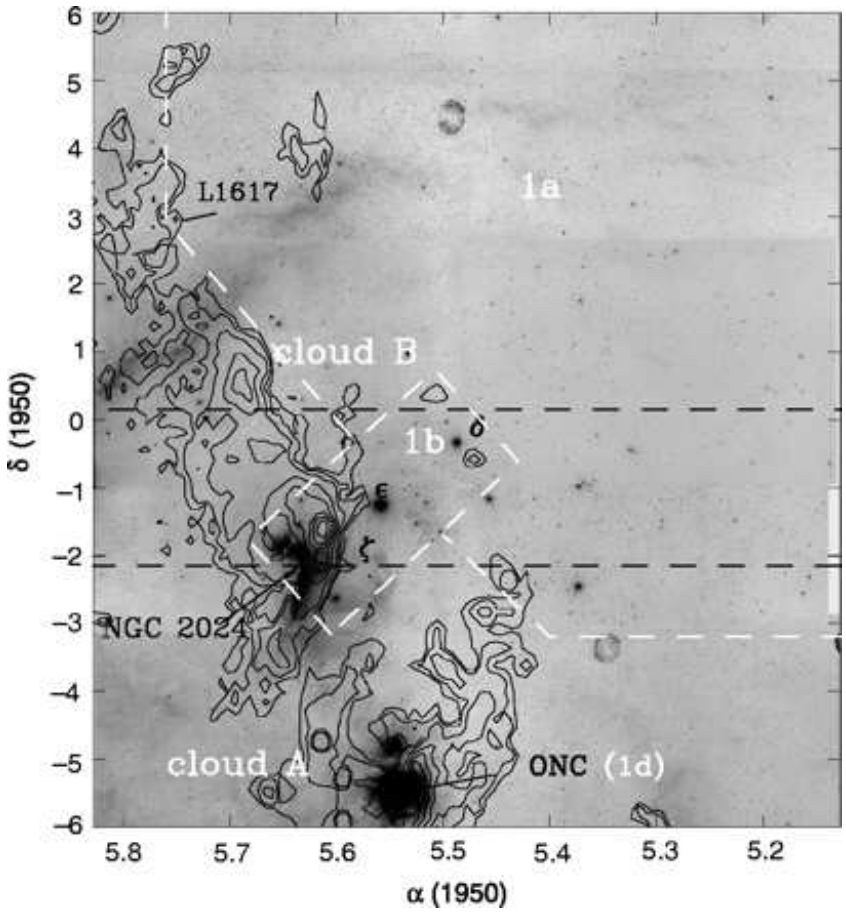

Figure 1.15. A region of the Orion OB1 association. The Orion OB region covers a large area on the sky and is composed of several kinematically distinct sub-associations. The dashed lines distinguish the 10 Myr Orion OB1a, which includes the 25 Ori stellar aggregate and Orion OB1b, a ∼5 Myr sub-association. Figure taken from Briceño et al. (2001).

CHAPTER 2

Evolution of X-ray and FUV Disk-Dispersing Radiation Fields

2.1 Introduction

Circumstellar disks, formed as a consequence of the star formation process, evolve from an initially gas rich phase to a system composed of small, planetary sized bodies, with little remaining gas. The physical processes responsible for depleting circumstellar gas from the initial minimum mass solar nebula (Weidenschilling, 1997, MMSN) to the low quantities remaining in debris disks, those with significant dust evolution and gas depletion, have been the focus of gas dispersal models (Clarke et al., 2001; Alexander et al., 2006; Gorti et al., 2009; Gorti & Hollenbach, 2009; Owen et al., 2010). Models for the evolution of the dust (Dullemond & Dominik, 2005; D'Alessio et al., 2006; Robitaille et al., 2007) have been successfully utilized in the interpretation of a variety of Infrared (IR) spectral shapes (Sargent et al., 2006; Hernández et al., 2007b; Espaillat et al., 2007; Currie, 2008; Furlan et al., 2009; Najita et al., 2010). These models indicate that while some of the material is locked into planets and still more is accreted onto the star through viscous evolution, it is likely that photoevaporation is the most significant process playing a role in the dispersal of the gas disk. There are several contributors to photoevaporation, including X-rays or Extreme Ultraviolet (EUV) photons from the central star and Far Ultraviolet (FUV) emission produced in an accretion shock at the stellar surface of classical T Tauri stars, or CTTS (Owen et al., 2010; Gorti & Hollenbach, 2009). At any given time, contributions from several different photoevaporation mechanisms will occur, but the overall timescales when each contribution is greatest may vary. For example, accretion

related radiation fields will decay as the mass accretion rate ($\dot{M}$) decreases. Alternatively, X-ray emission may increase as the accretion related radiation fields drop due to increased magnetic activity in non-accreting T Tauri stars (WTTS), observed as a possible increase in X-ray luminosity from 1-100 Myr in the *Chandra* Orion Ultradeep Project (COUP) survey of young stars (Preibisch & Feigelson, 2005). The changing environment may play a role, as FUV and X-rays dominate photoevaporation early at $\dot{M} < 10^{-6}$ $M_\odot\,yr^{-1}$, while EUV photons are absorbed in the accretion streams and do not become a significant contributor until $\dot{M}$ drops to $< 10^{-8}$ $M_\odot\,yr^{-1}$ (Gorti et al., 2009).

With the large number of factors to consider in gas disk evolution, the intensity of UV and X-ray radiation fields and the timescales relevant to their evolution are essential parameters in the theory of photoevaporation. Not only observations of the radiation fields, but observations of the frequency of circumstellar disks place constraints on disk evolution theory, with only 10% of sources retaining disks at 10 Myr (Hernández et al., 2007a). Full (or primordial) disks and debris disks are observed at both 5 and 10 Myr (Hernández et al., 2006, 2009), indicating that disk dispersal mechanisms must occur on a number of timescales in a single star forming region. Transitional and pre-transitional disks, which due to the presence of a gap are interpreted as an intermediary stage between full and debris disks (Strom et al., 1989; Calvet et al., 2002; Espaillat et al., 2008), are observed to have a low frequency indicating that when disk dissipation begins it occurs quickly, taking as little as 0.5 Myr (Luhman et al., 2010; Hernández et al., 2010; Muzerolle et al., 2010). Alternatively, disk evolution may proceed along another path in which a similar decline in IR fluxes from all disk radii indicates that no gap or hole is formed (Sicilia-Aguilar et al., 2010; Manoj, 2010; Hernández et al., 2010). With the diversity observed in disk evolution, different dispersal mechanisms may be necessary. In this chapter we investigate the relevant timescales for the evolution of disk dispersing emission from T Tauri stars with new X-ray and FUV observations spanning 1-10 Myr, and include previous observations of a larger sample of observations extending to young stars at 1 Gyr.

While EUV emission is almost impossible to observe due to interstellar hydrogen absorption, X-ray observations are numerous. X-ray emission in T Tauri stars is significantly stronger, up to 1000 times, than the X-ray emission from main sequence stars, and comes from hot plasma with temperatures up to 60 MK or energies up to 5 keV (Feigelson et al., 2002). The current paradigm is that this hot plasma is produced through enhanced magnetic activity, with stronger magnetic reconnection events the likely cause of observed short period flaring activity (Feigelson et al., 1993). There is some evidence that strong soft X-ray emission is produced in an accretion shock on the stellar surface (Günther et al., 2007). Currently observations of a soft X-ray component which dominates over the coronal emission are unique to the star TW Hya, although other sources have exhibited accretion produced X-ray emission, though at a significantly lower level (Robrade & Schmitt, 2006). Surveys of young, <10 Myr star forming regions have shown no evidence of a decline in the X-ray emission between 0.2 and 10 keV as $\dot{M}$ decreases, indicating that accretion related X-ray emission is not a significant contributor to the total X-ray flux in most circumstances (Preibisch & Feigelson, 2005; Mercer et al., 2009). While roughly constant between 1 and 10 Myr, eventually the X-ray emission does decrease. When this decline begins has not been well characterized so far because the only 10 Myr old X-ray sources studied were the eleven sources in the TW Hydra Association (Webb et al., 1999, TWA). Previously, the cluster nearest in age to TWA with well characterized X-ray properties was the 6–8 Myr η Chamaeleon cluster (López-Santiago et al., 2010), with fourteen sources. In this chapter we analyze X-ray observations from another older cluster, the 25 Ori aggregate in the Orion OB1a subassociation (Briceño et al., 2007). At 7–10 Myr, 25 Ori still has 4-5 remaining CTTS and a large number of WTTS, making it the most populous ∼10 Myr old star forming region known. Extinction in this off-cloud area is low, making it an ideal region for studying X-rays from T Tauri stars in older, evolved populations.

Less is known about FUV emission from T Tauri stars than X-ray emission because, until recent instruments like the Cosmic Origins Spectrograph (COS) on the Hubble Space Telescope (HST), most FUV detectors lacked the sensitivity to observe

dim sources. Large FUV samples have been obtained with the International Ultraviolet Explorer (IUE) through which FUV line emission has been well characterized (Valenti et al., 2000; Johns-Krull et al., 2000), but little to no signal was achieved in the continuum at $\lambda < 1750$ Å for the WTTS. Space Telescope Imaging Spectrograph (STIS) observations of T Tauri stars have also been analyzed; however, long exposure times were required for all but the brightest sources, limiting the ability of STIS to observe a large population (Calvet et al., 2004; Herczeg et al., 2002, 2006). Even though IUE and STIS observations are limited, the T Tauri properties observed in these high resolution spectra were used to interpret low resolution spectra obtained in a large sample of CTTS, WTTS, and debris disks using the Advanced Camera for Surveys Solar Blind Channel (ACS/SBC) prism on HST. While low in resolution, with its excellent sensitivity ACS/SBC obtained some of the first observations of WTTS in the FUV with the continuum detected from 1230 – 1800 Å (Chapter 3).

The origin of FUV emission in T Tauri stars has contributions from several sources. In addition to an accretion shock component (Calvet et al., 2004), H_2 in the inner region of CTTS disks contributes to the FUV line and continuum emission (Abgrall et al., 1997; Bergin et al., 2004; Herczeg et al., 2004, 2002; France et al., 2010). The evolution of FUV emission has not been well studied, as FUV spectra of T Tauri stars greater than 1-3 Myr are rare, and previously included only four T Tauri stars in the TWA region and older debris disks (Herczeg et al., 2004, Chapter 3).

In this chapter, we discuss the evolution of high energy radiation fields by analyzing the X-ray and FUV luminosities of a large sample of sources (the largest FUV sample to date) with ages between 1 Myr and 10 Myr, including a small sample of post T Tauri objects with ages up to 1 Gyr. In § 2.2 we discuss the new X-ray, FUV, and optical observations used in our analysis. In § 2.3.1 we present new X-ray selected T Tauri stars in 25 Ori and Chamaeleon I. In § 2.3.2 we present results of spectral analysis performed on high count rate X-ray sources and we discuss the calculation of X-ray and FUV luminosities in § 2.3.3 and § 2.3.4. Finally, in § 2.4 we analyze the high energy radiation fields and discuss whether the observed evolution is consistent with current disk evolution theories.

2.2 Source Sample and Observations

2.2.1 X-ray Data

Chandra observations of four fields in the 7–10 Myr 25 Ori star forming association were obtained in 2008 January with ACIS-I and S chips. Observations were done in FAINT mode with 10 ks exposures in GO Program 09200907 (PI: Hartmann). Additionally, observations of two fields in the 2.5 Myr Chamaeleon I star forming region were obtained in 2009 February with ACIS-I and S chips. Again, the observations were taken in FAINT mode in GO Program 09200909 (PI: Calvet) with 25 ks exposure times. We analyzed the evt2 files provided from the *Chandra* version 7.6.11.4 processing pipeline. X-ray detections were identified using the *Chandra* Interactive Analysis of Observations software (Fruscione et al., 2006, CIAO) script WAVDETECT with the default significance threshold set to 10^{-6}. We cross-correlated the X-ray detections with the Luhman (2004), Luhman et al. (2008), and the CIDA Variability Survey of Orion (Briceño et al., 2005, CVSO) optical catalogs and identified previously studied T Tauri sources.

In Chamaeleon I, the selected fields focused on two CTTS with disks showing evidence for inner clearing, SZ Cha (T6) and T35 (Kim et al., 2009). We detected 15 known T Tauri stars in the two fields (out of ∼60 X-ray sources identified by WAVDETECT), five of which are accretors (Luhman, 2004). The sources are listed in Table 2.1 and their positions in the H-R diagram are shown in Figure 2.1 based on spectral types and luminosities from the literature (see references in Table 2.1). Using the evolutionary tracks of Siess et al. (2000), we determine that the sample covers a large range of T Tauri masses from a 1–1.5 $M_{\odot}$ upper limit down to almost substellar masses, with a lower limit of 0.1–0.2 $M_{\odot}$. This mass range is similar to that used in Preibisch & Feigelson (2005), in which the evolution of X-ray emission in the low mass population of the COUP sources was analyzed.

Each of the four fields in the 25 Ori aggregate was centered on a known CTTS, specifically CVSO 35, CVSO 206, OB1a 1630 (Briceño et al., 2005; Hernández et al., 2007b), and the transitional disk CVSO 224 (Espaillat et al., 2008). Of ∼150 X-

ray sources located by WAVDETECT, we identified 36 previously known T Tauri stars, in addition to the 4 targeted sources, from the catalogs of Briceño et al. (2005, 2007), Briceño et al. (2010), and Hernández et al. (2007b) for a total of 40 7–10 Myr classical and weak T Tauri stars. Of the remaining unidentified X-ray detections, six are possible newly detected T Tauri stars (see §2.2.3 for further discussion). The locations of the 25 Ori sources in the H-R diagram are shown in Figure 2.2. Sources published in Calvet et al. (2005) had known spectral types and luminosities but sources published in Briceño et al. (2007), Hernández et al. (2007b), and Briceño et al. (2010) had only spectral types and optical colors. To get luminosities for those sources, we first used $V - I$ colors to get the reddening (A_V) assuming photospheric colors from Kenyon & Hartmann (1995). With A_V, we corrected Two Micron All Sky Survey (Skrutskie et al., 2006, 2MASS) J magnitudes for reddening using the Mathis extinction law with $R_V = 3.1$ (Mathis, 1990) and calculated the bolometric fluxes (Kenyon & Hartmann, 1995). Our sample of 25 Ori sources is similar to the CTTS masses of Taurus, from $\sim$0.2–1.0 $M_\odot$. Table 2.1 lists the complete set of sources detected in the Chamaeleon I and 25 Ori fields which are discussed in this chapter, along with published spectral types and disk classifications.

After matching X-ray detections to previously identified T Tauri stars, we used the CIAO script DMEXTRACT to obtain the counts within the extraction regions determined by WAVDETECT for each known T Tauri source. We included a background region defined as a 5" annulus around each extraction region, allowing us to determine the net counts and calculate the poisson errors which we used to estimate uncertainties in the X-ray luminosities (§ 2.3.3). Of the 15 Chamaeleon sources, 5 had greater than 250 counts and the spectra of these sources were extracted using the CIAO script PSEXTRACT, using the 3σ detection regions determined in WAVDETECT, and the 5" background annuli. Each extracted spectrum was re-binned to 20 counts per bin using the GRPPHA task in FTOOLS. The re-binned spectra were then analyzed in the X-ray spectral fitting package, XSPEC (Arnaud, 1996). Only three of the 25 Ori sources had counts in excess of 250, likely due to the shorter exposure times and greater distance to the sources, and were analyzed with PSEXTRACT and

XSPEC.

2.2.2 UV Data

We present new FUV observations of ten sources in the 2.5 Myr Chamaeleon I and two in the 4 Myr Chamaeleon II star forming regions obtained with the PR130L grating on the Advanced Camera for Surveys (ACS) Solar Blind Channel (SBC). These observations were completed between 2008 December and 2009 February in GO Program 11145 (PI: Calvet). The FUV coverage extends from 1230–1800 Å with R$\sim$300 at 1230 Å and $\sim$50 at 1700 Å. The *Chandra* and ACS/SBC Chamaeleon I samples have some overlap but there are sources unique to each sample. We show all the Chamaeleon I and II sources in Figure 2.1, identifying the X-ray and FUV sources and those included in both samples. With ACS/SBC we observed sources from 0.3–2.0 $M_{\odot}$ in Chamaeleon I and approximately solar mass sources in Chamaeleon II.

We combine these new observations with previously observed ACS/SBC and STIS samples of T Tauri stars analyzed in Chapter 3, Calvet et al. (2004), and Herczeg et al. (2002, 2004). The total sample of sources with FUV spectra consists of 56 sources, eleven of which are WTTS or debris disks, and these are listed in Table 2.1, with sources observed by STIS distinguished in bold font.

2.2.3 Optical Data

A large number of X-ray detections corresponded to unidentified counterparts in IR and optical catalogs. Using 2MASS and CVSO photometry (Briceño et al., 2005), we produced color-magnitude diagrams in V and $V-J$ to select sources which fell above the main sequence. In Chamaeleon I, one such object met the color requirements (K. Luhman, personal communication) and in 25 Ori there were six possible new T Tauri stars detected.

For three of the six T Tauri candidates in 25 Ori, we followed up the X-ray observations by obtaining optical spectra with the Magellan Echellete (MagE) on the Magellan- Clay telescope at Las Campanas Observatory (Marshall et al., 2008). MagE provides R$\sim$4100 spectra from 3200–9800 Å, including the Li 6707 line, for

confirmation that the sources are young, and Hα necessary to classify them as T Tauri stars. In addition to the MagE spectra of new T Tauri stars, we obtained R$\sim$ 35,000 MIKE (The Magellan Inamori Kyocera Echelle) observations of 16 sources in our sample, primarily of accretors in the 25 Ori and Chamaeleon I and II regions.

The optical data were reduced using the Image Reduction and Analysis Facility (Tody, 1993, IRAF) tasks "ccdproc", "apflatten" and "doecslit". Bias corrections were completed with "ccdproc". Flats were created using "apflatten", in which the orders were traced using observations of a quartz lamp for the MIKE flat frames and the 10 reddest orders of MagE. For the five bluest orders of MagE, we observed a Xe lamp with a wide slit (5" as opposed to the science slit at 1") and out of focus for the trace. The task "doecslit" was used to extract the science spectrum, extinction correct for airmass, subtract the background, and dispersion correct the spectra using a ThAr comparison lamp. The blaze function was fit using a bright O or B standard star and used to correct for the blaze in the science exposures.

2.3 Analysis of Observations

2.3.1 Results from Optical Observations

MIKE optical spectra were used to confirm status of WTTS or CTTS and obtain accretion rates for the CTTS using the relation between $\dot{M}$ and Hα 10% width of Natta et al. (2004). We show Hα line profiles in Figure 2.3 for the accreting sample of MIKE sources. The relation between Hα width and $\dot{M}$ is more appropriate for low values of the mass accretion rate.

The three candidate members of 25 Ori with MagE optical spectra, discussed in § 2.2.3, showed Li absorption and but only two (2MASS J05243490+0154207 and 2MASS J05270173+0139157) had weak Hα emission, indicating that they are newly identified WTTS. The third source (2MASS J05244265+0154116) has Hα in absorption but may be a young member of 25 Ori still, due to its early spectral type; additional analysis is needed for confirmation. This final source is not included in any further analysis of the 25 Ori X-ray observations. The Li and Hα equivalent

widths, along with the derived spectral types are listed in Table 2.2 for those sources which have optical spectra. All of the candidate X-ray selected T Tauri stars, in both Chamaeleon I and 25 Ori, are listed in Table 2.2. MagE spectra will be obtained for the remaining sources in need of optical spectra.

2.3.2 X-ray Spectral Analysis

Eight sources in our Chamaeleon I and 25 Ori samples had strong X-ray fluxes allowing for spectral analysis to determine temperatures for the emitting plasmas. Three of these sources are accreting (CR Cha, SZ Cha, and TW Cha) and the remaining five sources are not (Luhman, 2004; Calvet et al., 2005). With this sample of high count sources, we looked for any observable distinction between the CTTS and WTTS. In XSPEC, each source spectrum was fit using either one or two APEC (Astrophysical Plasma Emission Code) models characterized by different temperatures; the choice of models was motivated by the two-temperature plasma observed in X-ray emission from Pleiades sources (Briggs & Pye, 2003). Assuming a model which includes multiple temperatures also allows for the distinction of a soft accretion related emission component, if present, similar to that observed in TW Hya (Günther et al., 2007). We included an absorption component using the XSPEC model, PHABS, with the equivalent neutral hydrogen column density[1] obtained from the HEASARC (High Energy Astrophysics Science Archive Research Center) N_H calculator (Kalberla et al., 2005; Dickey & Lockman, 1990).

The models with the best statistical fit to the observations (or lowest χ^2_{red}) are given in Table 2.3. The best fit models for CR Cha, SY Cha, SZ Cha, and TW Cha produced good χ^2_{red}'s, but the remaining sources had either poor fits or model properties discrepant from the larger sample. For CHXR 30A, when the absorption model was forced to have a column density of $N_H = 8 \times 10^{20}$ cm^{-2} (Kalberla et al., 2005; Dickey & Lockman, 1990), a 64 keV plasma was necessary to fit the spectrum,

[1]The equivalent neutral hydrogen column density (defined as N_H) is the column density of hydrogen required to give the same opacity as that resulting from the true composition of the absorbing gas, which has contributions from He, C, N, O, and Ne in addition to less abundant gasses.

greater than ten times higher than the highest expected plasma temperatures (Feigelson et al., 2002). Allowing the column density to vary, we found a best fit model with $N_H = 12.2 \times 10^{21}$ cm^{-2}, fifteen times higher than N_H in the four Chamaeleon sources with good fits. While high, a greater value for N_H is consistent with CHXR 30A being extincted by $A_J \sim 3$ magnitudes while the other sources have $A_J = 0.0 - 0.5$ (Luhman, 2007). The APEC model fits to CVSO 38 resulted in a large temperature for the hot component, a temperature typical of flares in T Tauri stars (Getman et al., 2008), indicating that the observations may have caught it while flaring. The APEC components and best model fit to the highest count rate X-ray source (CR Cha) are shown in Figure 2.4. For CR Cha we find that a two-temperature model improves the χ^2_{red} by a factor of 3 compared to a single temperature model. Like CR Cha, the models of the four sources with the best χ^2_{red} fits are each comprised of a cool, 0.3-0.9 keV, component and a hotter 2-5 keV component. We note that the hottest emission (excluding the possible flare component from CVSO 38) comes from SZ Cha which, as a G2, is the source with the earliest spectral type.

Previous analyses of X-ray spectra from CTTS have shown that the presence of accretion alters the X-ray spectrum by producing emission lines formed in the high densities of the accretion shock (Robrade & Schmitt, 2006; Brickhouse et al., 2010). Also, cool X-ray components with kT ∼0.2–0.3 have been attributed to accretion (Günther et al., 2007; Robrade & Schmitt, 2006). We see no clear evidence of accretion related soft X-ray emission in CR Cha, SZ Cha, and TW Cha, the known accretors in our sample. The cool APEC components are ∼2–10 times hotter than the temperatures expected of plasmas heated in an accretion shock, even when considering material falling faster than the free fall velocity which is necessary to produce the soft X-ray shock emission in TW Hya (Günther et al., 2007). Brickhouse et al. (2010) obtained high resolution Chandra spectra of TW Hya and identified line emission which is attributed to accretion. Additional observations obtained with XMM-Newton of a sample of four CTTS, including both TW Hya and CR Cha (which we analyze in Figure 2.4), showed that shock formed line emission may be needed to confirm accretion for sources unlike TW Hya, where the soft accretion component

does not strongly exceed the coronal emission. The resolution of our ACIS spectra prohibited accretion line analysis, which would be informative, particularly for TW Cha, the accretor with a cool component most similar to that in TW Hya. Interestingly, the sources with the coolest components (SY Cha, 2MASS J05244498+0159465 and RX J0526+0143) are WTTS and have been identified as such by observations of Hα, indicating that a detection of a cool component alone cannot confirm accretion and likely line detections are needed as well (Robrade & Schmitt, 2006).

Instead, our results are consistent with the two-temperature coronal emission observed in Pleiades sources (Briggs & Pye, 2003); however, for Chamaeleon, the temperatures of the hot component are approximately 2 times higher than the hot components in the Pleiades sources. This may be indicative of theorized cooling coronal gas, producing a softer spectrum as X-ray sources evolve (Kastner et al., 2003). The results of our spectral analysis show that we can use the same treatment to find X-ray luminosities for both the WTTS and CTTS since we see no evidence for an accretion related component.

2.3.3 X-ray Luminosities

The majority of the X-ray sources had <250 counts, so instead of attempting detailed spectral analysis on dim sources we assume typical X-ray temperatures as determined for the sources discussed in § 2.3.2. We assume there is no discernible difference between the X-ray properties of the CTTS and WTTS in the spectral region observed by ACIS, as indicated by the results shown in Table 2.3. Using WebPIMMS on the HEASARC website we calculated unabsorbed fluxes between 0.2 and 10 keV for the entire sample, correcting for $N_H = 0.8 \times 10^{21}$ and $N_H = 1.1 \times 10^{21}$ cm^{-2} for Chamaeleon I and 25 Ori, respectively (Kalberla et al., 2005; Dickey & Lockman, 1990). We assumed a single temperature APEC model with kT=2.2 keV and solar abundance. From the unabsorbed fluxes, X-ray luminosities were calculated assuming distances of 160 and 330 pc for Chamaeleon I and 25 Ori, respectively; the results are listed in Table 2.1. For the sources in Table 2.3, which were fit with XSPEC, we find that the when using WebPIMMS to find fluxes, the discrepancy is a factor of

2–3. The distribution of unabsorbed X-ray luminosities is shown in Figure 2.5, which indicates that our Chamaeleon I sample is not complete. To increase the sample, we include X-ray observations of this region from Feigelson et al. (1993) in our analysis. The ROSAT count rates from Feigelson et al. (1993) were converted to ACIS-S count rates using WebPIMMS before luminosities were calculated.

In addition to the X-ray luminosities calculated here, we include X-ray luminosities from the literature for sources with FUV spectra which were not observed with *Chandra*, primarily in Taurus, TWA, and nearby debris disks (shown in italics in Table 2.1). X-ray fluxes of Taurus sources were calculated as part of the XMM Newton Extended Survey of Taurus (XEST) project (Güdel et al., 2007). Güdel et al. (2007) gives count rates for the PN camera with the medium filter and these were converted into *Chandra* ACIS-S count rates using WebPIMMS, assuming an input XMM-Newton energy range of 0.4-10 keV and output *Chandra* energy range of 0.2-10 keV, and using the same model parameters as were used to calculate the fluxes from our *Chandra* observations. X-ray fluxes for sources in Taurus not provided by Güdel et al. (2007), along with sources in Chamaeleon I and II, TWA, and field debris disks were converted from ROSAT PSPC count rates (Feigelson et al., 1993; Voges et al., 1999, 2000) into *Chandra* ACIS-S count rates, again using WebPIMMS but using the softer input energy of ROSAT (0.1-2 keV). Once converted to ACIS-S count rates, the unabsorbed X-ray fluxes were calculated as discussed for our new *Chandra* observations and the luminosities are given in Table 2.1. We also include X-ray luminosities from other young clusters in our analysis of X-ray evolution; those from the $\sim$ 4 Myr cluster, Trumpler 37 (Mercer et al., 2009), and the 6–8 Myr η Cha region (López-Santiago et al., 2010).

2.3.4 FUV Luminosities

Our FUV sample contains sources in Taurus, the Chamaeleon I and II clouds, 25 Ori, TWA, objects in the outskirts of the Orion Nebular Cluster (ONC), and nearby WTTS or debris disks. We calculated FUV luminosities for these sources between 1230 and 1800 Å after degrading the resolution of the STIS spectra to that of

ACS/SBC for comparison. Spectra were corrected for reddening using A_V's provided in Chapter 3 and Calvet et al. (2004) for Taurus, ONC, 25 Ori, and the nearby WTTS and debris disks. For the Chamaeleon I and II sources, A_V's were calculated from published photometry (Gauvin & Strom, 1992). For sources in Taurus, the ONC, and Chamaeleon I and II we corrected for reddening using the extinction curve observed along the line of sight towards HD 29647 with $R_V = 3.6$, appropriate for regions with associated molecular clouds (Whittet et al., 2004). For sources in the dispersed 25 Ori association, we used the Mathis extinction law with $R_V = 3.1$ (Mathis, 1990). We note that UV extinction laws, especially in the FUV, are very uncertain and introduce the largest error in our FUV luminosity calculations. We assume a ± 0.2 magnitude error in A_V, which dominates other sources of error. For four Chamaeleon sources, we failed to detect the FUV emission and upper limits are provided for these sources. We calculated the flux in the detector noise and de-reddened the noise by the calculated A_V's. In this manner, we are accounting for any FUV emission washed out by extinction. Calculated FUV luminosities are given in Table 2.1, with upper limits on the luminosities provided when appropriate.

2.4 Implications of Observations

2.4.1 Evolution of X-ray and UV Emission

The intensity of high energy emission from T Tauri stars has important implications for the dispersion of circumstellar disks and the planets which may be forming within them. Over a time period of 1-10 Myr, during which these processes are expected to occur, we investigate the evolution of the X-ray and FUV radiation fields. Figure 2.6 shows the median and full range of X-ray luminosities for the sources in each star forming region with spectral type K5 or later. The sample of Tr37 may include sources with earlier spectral types (early K); however, spectral types are not well established for this sample. In addition, it was confirmed that several of the Tr37 sources were flaring during the observations (Mercer et al., 2009), contributing to the high X-ray luminosities. Figure 2.6 reveals that there is no decrease with age in either total

X-ray luminosity or the X-ray luminosity normalized by the stellar luminosity, up to 10 Myr. Most importantly, our addition of the 7–10 Myr 25 Ori X-ray observations supports previous claims that X-ray radiation from the central star remains strong throughout the disk dispersal phase (Mercer et al., 2009; Preibisch & Feigelson, 2005). While there does appear to be a slight increase in the normalized X-ray luminosity with age, the trend is statistically insignificant, with a Pearson correlation coefficient of only 0.2.

Figure 2.7 shows the evolution of FUV luminosities from 1 Myr T Tauri stars to 1 Gyr young stars and debris disks. While there is an observed decrease in FUV luminosity out to 1 Gyr, a decrease with age can also be seen among the 1-10 Myr sources, with the WTTS characterized by the lowest FUV luminosities. By the WTTS phase, FUV luminosities are expected to be entirely chromospheric. With no additional accretion, FUV emission is no longer produced in an accretion shock and because the end of accretion indicates the depletion of inner disk gas, FUV emission from hot molecular gas no longer contributes to the FUV flux (Pascucci et al., 2006, see also Chapter 3). In addition to the decline with age, a correlation between FUV luminosity and L_{acc} is observed, with a Pearson correlation coefficient of 0.78 (calculated with the exclusion of sources with only upper limits), indicating that FUV emission is strongly correlated with L_{acc}. Values of L_{acc} were obtained from the literature (see references in Table 2.1) or calculated from Hα 10% line widths (Natta et al., 2004, § 2.3.1).

This correlation between FUV luminosity and L_{acc} is not surprising, given results that FUV emission is produced in the hot gas of the accretion shock (Calvet et al., 2004; Calvet & Gullbring, 1998; Herczeg et al., 2002). Therefore, the decrease in FUV luminosity between 1 and 10 Myr can be understood in terms of the decrease of $\dot{M}$ in this time period (Hartmann et al., 1998; Calvet et al., 2005; Sicilia-Aguilar et al., 2006; Fedele et al., 2010). We use the model of Calvet & Gullbring (1998) to predict the amount of FUV emission produced in the accretion column. This model assumes that the circumstellar disk is truncated at a few stellar radii by the stellar magnetic field. At the truncation radius, gas is channeled along the magnetic fields

lines from the disk to the star, impacting the stellar surface at approximately the free fall velocity. Such fast moving material produces an accretion shock on the surface of the star which heats the gas to ∼1 MK. Emission from this hot gas heats both the photosphere below the shock and the pre-shock material, producing an accretion column spectrum with a significant excess over the photospheric emission in the UV (Calvet & Gullbring, 1998).

As inputs to the accretion column model, we assume a $0.8M_{\odot}$ source evolving along the Siess et al. (2000) evolutionary tracks, from which we obtain the radius, effective temperature, and luminosity of the source from 1–10 Myr. We assume the percentage of the stellar surface covered by accretion columns, the filling factor, remains constant at 1% and vary the energy flux in the accretion column for a given $\dot{M}$ (Calvet & Gullbring, 1998). Using these quantities we calculate the column emission and integrate the flux from 1230–1800 Å for the highest and lowest $\dot{M}$'s observed at each age (Calvet et al., 2005). We also calculated the FUV accretion emission for the $\dot{M}$'s predicted from a viscously evolving disk with an initial mass of $0.1M_{\odot}$ (Hartmann et al., 1998). Using this technique, we find we can approximate the range of observed FUV luminosities well (left panel of Figure 2.7), but for typical CTTS masses, the predicted FUV fluxes from the viscously evolving disk are too low (right panel of Figure 2.7).

The missing FUV emission is probably due to several sources which are not included in our accretion column models. First, emission from H_2 gas was observed in the FUV spectra of CTTS and was necessary to explain the FUV continuum between 1500 and 1700 Å. The contribution of gas emission can be a significant portion (∼ 30%) of the total FUV emission, although it does not contribute to the disk heating, since it likely originates in the upper layers of the disk (Bergin et al., 2004; Herczeg et al., 2002, 2004; France et al., 2010, Chapter 3). In addition, we measure the flux in the strong FUV atomic lines of existing spectra, which our accretion column models do not attempt to reproduce and find that ∼ 35% of the total FUV flux comes from hot lines. Another contribution necessary for re-producing the short wavelength FUV continuum ($\sim 1300 - 1400$ Å) could originate in post-shock emission escaping

absorption by the pre-shock material. The post shock spectrum peaks in the soft X-rays but extends into the FUV around 1300 Å (Calvet & Gullbring, 1998). This emission would be important for disk photoevaporation models as soft X-rays can efficiently heat disk gas (Owen et al., 2010), but may only play a role when the $\dot{M}$ drops and the accretion columns become less dense (Gorti & Hollenbach, 2009). Additional observations are required to determine if this is a viable contribution to the FUV spectrum.

After accretion has ended and the gas has been dissipated at >10 Myr, FUV luminosities continue to decline. This is also observed in magnetically active young stars; all high energy radiation fields decrease as the sources evolve towards and even along the main sequence (Ribas et al., 2005). Given this fact, we looked for any relation between the FUV and X-ray emission in the CTTS and non-accretors. In Figure 2.8 we distinguish non-accretors (diamonds) from CTTS (squares) and indicate hotter stars by larger symbols. We see no correlation between FUV and X-ray emission in the CTTS (with Pearson correlation coefficients of 0.3 and -0.2 for total and normalized luminosities, respectively) but we note that the sources with earlier spectral types tend to have the strongest total FUV and X-ray emission, as they are observed to occupy the upper right hand corner in the left panel of Figure 2.8. FUV and X-ray luminosities normalized by the stellar luminosity are indistinguishable by spectral type (right panel of Figure 2.8). We do observe a weak correlation between both total and normalized X-ray and FUV luminosities when considering only the non-accreting sample, with Pearson correlation coefficients of 0.74 and 0.80, respectively.

We compare results from our sample of non-accreting young stars (excluding the low mass TWA sources) to an analysis of solar analogs between 0.1 and 10 Gyr (Ribas et al., 2005), which showed that high energy fields between 1 and 1200 Å decreased with age, with emission from hotter plasmas diminishing more quickly. For our sample of non-accreting solar type sources between 15 Myr and 1 Gyr, classified as young suns in the Formation and Evolution of Planetary Systems survey (FEPS; Meyer et al. 2006), we compare the observed luminosities to those predicted assuming the power

law relations between flux in a given energy range and age from Ribas et al. (2005). The predicted decay of X-ray luminosities is similar to that which we observe for the youngest of the solar type non-accretors in our sample but fail to re-produce the 1 Gyr source, HD 53143 (see Figure 2.9). We also compare the slope of the predicted FUV fluxes between 920–1180 Å to the slope of our observations which cover 1230–1800 Å. The total predicted luminosities were scaled, due to the use of different wavelength bins, but the slope was held constant. Again, the younger sources follow the predicted slope but the 1 Gyr source has an unexpectedly high FUV luminosity. It is unclear why HD 53143 is discrepant in both X-rays and FUV fluxes for its age, with several different age indicators providing consistent values (Song et al., 2000).

Our young solar analogs extend the radiation evolution observed in Ribas et al. (2005) to younger ages, and agree with their result that the higher energy radiation fields decline more quickly than the cooler fields. Combining our results with those of Ribas et al. (2005), we see evidence that even past the 10 Myr time period for disk dispersal and planet formation, high energy fields strongly in excess of the solar values persist and may have an effect on evolving disks and planets.

2.4.2 The He II λ1640 and C IV λ1549 lines

Using observations for a limited number of T Tauri stars, Alexander et al. (2005) have investigated the origin of the He II λ1640 and C IV λ1549 lines and their relationship to the continuum flux, responsible for photoevaporation of the gas disk. In particular, Alexander et al. (2005) propose that the ratio of the He II to C IV is a probe of the EUV radiation field. They base their conclusion on the fact that single temperature and density models of collisionally ionized plasmas cannot reproduce the observed strengths of the He II line, from which they infer that the line must be produced by radiative recombination. Since the ionization threshold for He I is 228 Å, they conclude that the line is a probe of the strength of the radiation field around this wavelength, namely, the EUV.

Here, we revisit these lines using our larger sample of FUV spectra of T Tauri stars. We measure the He II and C IV fluxes in our ACS/SBC and STIS samples of

sources with the STIS observations degraded to the low resolution of ACS/SBC. As a result of the resolution, we are measuring a blend of emission lines in each line feature, including both components of the C IV doublet and numerous H_2 lines present in the vicinity of C IV and He II. While adding to the scatter in our measurements, the dominant line in each region is the He II or the C IV line, with H_2 line contributions $< 10\%$. As discussed in § 2.3.4, the largest source of uncertainty comes from the reddening correction of the FUV spectra, so to estimate errors on the He II and C IV line luminosities we assume a range of ± 0.2 magnitudes in A_V. Figure 2.10 shows He II and C IV line luminosities and their dependence on age and L_{acc}. Both He II and C IV line luminosities are observed to decrease with age with the lowest values obtained for non-accretors. We find strong correlations between line luminosities and L_{acc}, with Pearson coefficients ~ 0.84 and 0.88 for He II and C IV, respectively. The strength of both lines is clearly related to accretion, as was previously found by Calvet et al. (2004) and Johns-Krull et al. (2000).

In the left panel of Figure 2.11 we show the He II to C IV ratio for the CTTS and non-accretors of our sample as a function of age. The value of the ratio is higher in non-accretors than in the CTTS, confirming the trend found by Alexander et al. (2005). These authors suggest that this trend indicates that the ionizing flux is not powered by accretion, since the ratio would be expected to decrease if that were the case. We suggest, instead, that the difference between the He II to C IV ratio between the CTTS and the non-accretors arises from the different formation mechanisms of the lines in each type of star. The He II λ1640 and C IV λ1549 lines in non-accretors must form in the transition region, as they do in the Sun and in magnetically active stars, indicated by the similarity of the ratio in the two classes of stars (Hartmann et al., 1979; Byrne & Doyle, 1989). In contrast, the correlations between line luminosity and L_{acc} found in CTTS indicate that these lines must form in the accretion flows or at least in regions powered by accretion energy. However, despite the line luminosity dependence on L_{acc}, we find no correlation between the He II to C IV ratio and L_{acc}, as shown in the right panel of Figure 2.11. Studies of the optical and infrared lines of He I and He II in CTTS indicate that the lines have multiple components arising

in the accretion shocks, the magnetospheric infall regions, and the winds (Beristain et al., 2001; Edwards et al., 2006). No comparable analysis of the C IV line has been done, but it is also likely that this line has contributions from the accretion shock and from the infall region, given its large velocity width (Ardila et al., 2002). This diversity may be responsible for the large dispersion of the He II to C IV ratios in CTTS. We therefore caution against using the He II to C IV ratio as an indicator of EUV emission without a careful treatment of accretion related emission in these lines.

Regardless of the effectiveness of the He II to C IV line ratio in tracing the EUV emission, strong EUV emission is likely present in the high energy spectrum of T Tauri stars. Ribas et al. (2005) showed that EUV emission decreases with age, or increases with the spin of the source. They also showed that younger sources have enhanced EUV line emission, in particular strong He II and Fe lines around 300 - 350 Å. Whether the EUV emission continues to increase at <10 Myr like the FUV emission or flattens and remains constant like the X-ray emission is not clear, but in either case the EUV emission is expected to be strong. In our model of the accretion column which contributes emission to the FUV spectrum (§2.4.1), we find that the EUV luminosity produced in the shock is $\sim 10^{31}$ ergs^{-1}. In the current model, only ∼2% of this emission escapes the high density material which is still accreting; however, recent work has shown that varying accretion properties, like the accretion rate or infall velocity, affects the amount of shock emission which can be observed (Sacco et al., 2008). Future models of the emission from the accretion column which take this into account will provide better estimates of the EUV emission which is available for photoevaporation.

2.4.3 High Energy Radiation Fields and Photoevaporation

In contrast to early photoevaporation models in which the primary mechanism for dispersing the disk utilized EUV radiation from the star producing winds with mass loss rates of $\sim 10^{-10}$ $M_\odot\,yr^{-1}$ (Hollenbach et al., 1994), recent models stress that either FUV or X-ray radiation fields are significantly more important in dispersing

the disk with mass loss rates 100 times higher than in the pure EUV case (Owen et al., 2010, 2012a; Gorti et al., 2009; Gorti & Hollenbach, 2009). While in agreement on the values of the mass loss rate, Owen et al. (2010) achieve these high rates with X-ray radiation while Gorti & Hollenbach (2009) find the FUV radiation drives the photoevaporation. With the large range of ages in our X-ray and FUV samples, we explore the photoevaporation theories in the context of our observations.

Our results agree with previous findings by Preibisch & Feigelson (2005) and Mercer et al. (2009) showing that the X-ray luminosity remains roughly constant during the first 10 Myr. Regarding models of X-ray photoevaporation, Owen et al. (2010) use $L_X = 2 \times 10^{30}$ ergs^{-1} for $h\nu > 0.1$ keV as their X-ray luminosity. We find similar, though consistently lower, X-ray luminosities for the typical CTTS mass sources in our sample. Owen et al. (2010) note that their input X-ray luminosity is large and that further analyses will include lower X-ray luminosities.

An important new result in this work is the evolution of the FUV radiation, where we see that the luminosity between 1230 and 1800 Å clearly drops between 1 and 10 Myr. Gorti & Hollenbach (2009) incorporate the evolution of FUV luminosity in their models for disk dispersal, assuming that $\dot{M}$ evolves viscously and the FUV luminosity is 0.4 L_{acc}. In Figure 2.7 we showed the evolution of the FUV luminosity along with the predicted FUV emission produced in an accretion column from a viscously evolving disk onto a $0.8M_{\odot}$ star. We found that the predicted FUV accretion emission is lower than the observed FUV fluxes, although, within an order of magnitude (assuming typical mass CTTS have $L_{acc} < 0.5\ L_{\odot}$) and we discussed origins for the remaining FUV emission in § 2.4.1. The FUV fluxes used by Gorti & Hollenbach (2009) are similar to those we observe, but we found that $\sim$1/3 of this emission may be produced by H_2 in the circumstellar disk and therefore not directly irradiating the gas in the disk.

Our observations support the requirements of both the X-ray and the FUV dominated photoevaporation models of Owen et al. (2010) and Gorti et al. (2009); however, several issues remain unresolved. For example, circumstellar disks of gas and dust have been observed around much older sources, including the 10 Myr CTTS TW

Hya which maintains a 0.06 $M_{\odot}$ disk, albeit a transitional disk (Calvet et al., 2002; Najita et al., 2010). Full disks of gas and dust are also observed around the 7–10 Myr CTTS in 25 Ori (Hernández et al., 2007b, see also Chapter 3). According to Owen et al. (2010), the continued existence of full disks at late stages could be explained by the range of X-ray luminosities observed, with lower X-ray luminosities increasing the disk lifetime and, alternatively, the presence of young WTTS may be due to high X-ray luminosities in those sources. In our 25 Ori observations in which ∼90% are WTTS, we find that the median X-ray luminosity (log L_X) is 29.7 erg s^{-1} and the four accreting sources have only marginally lower or, in one case, even higher X-ray luminosities. With similar X-ray luminosities to the WTTS, these accreting sources should have cleared their inner gas disks in similar timescales. If we look at the X-ray luminosities of the WTTS in the 2.5 Myr Chamaeleon region, we find a median log $L_X = 29.0$ s^{-1}, lower than all of the 25 Ori accretors, indicating that if these X-ray luminosities may disperse an inner gas disk in ∼2.5 Myr, they would clearly be gone by 10 Myr. An additional parameter, besides a range of X-ray luminosities, is necessary to explain the diversity of disks observed at a given age.

When including the time evolution of the FUV radiation fields and their dependence on disk properties, like $\dot{M}$, Gorti & Hollenbach (2009) find FUV fields evolving on a range of timescales related to differences in the accretion properties. Therefore, photoevaporation dominated by evolving FUV fields may disperse disks in a range of timescales. With FUV driven photoevaporation and evolving FUV fields, the diversity of disks observed at any age may be expected. This appears to be a plausible scenario given the large range of observed FUV luminosities and inferred $\dot{M}$'s. Again, the full disks in the 25 Ori association present an obstacle to the theory. The observed FUV luminosities of the 25 Ori accretors are $\sim$ 2 orders of magnitude higher than the WTTS in the 10 Myr TWA association, and given our results and those of Ribas et al. (2005), were likely stronger at 1 Myr. These FUV luminosities should be high enough to photoevaporate the gas disk, if FUV emission was responsible for the gas depletion in the TWA WTTS. Possible explanations for the remaining full disks in 25 Ori, in the context of both X-ray and FUV photoevaporation theories, include low

disk viscosities or high initial disk masses which increase the time for disk dispersal (Owen et al., 2010).

2.4.4 FUV Radiation and Dust Evolution

So far, we have focused on the gas in circumstellar disks; however, it is unclear if gas and dust evolution proceed concurrently or independently (Pascucci et al., 2006). Alexander & Armitage (2007) modeled the affect of photoevaporation on the gas and dust in the circumstellar disk and found that the removal of gas from the disk has significant effects on the dust. When photoevaporation creates a gap in the gas disk, the inner disk dust is also removed. Also, pressure gradients formed when gas is removed cause the dust to migrate and may enhance grain growth. For these reasons, we may expect to see dust evolution dependent on the strength of the photoevaporative fields. With constant X-ray fields throughout disk evolution, we focus on the accretion related FUV radiation fields.

Fedele et al. (2010) find that dust dissipation and accretion are characterized by different timescales and to test this further, we compare FUV luminosities to 2MASS J, H, K (Skrutskie et al., 2006), IRAC (*Spitzer* InfraRed Array Camera), and MIPS (*Spitzer* Multiband Imaging Photometer) colors. IRAC and MIPS photometry, along with disk classifications for our source sample, were taken from the literature: Taurus (Luhman et al., 2010), Chamaeleon I (Luhman et al., 2008), Chamaeleon II (Alcalá et al., 2008), 25 Ori (Hernández et al., 2007b), TWA (Low et al., 2005; Hartmann et al., 2005), and debris disks (Carpenter et al., 2008; Chen et al., 2005). Figure 2.12 shows the relations between FUV luminosity and inner disk dust tracers. At $\lambda < 24$ μm we are tracing the dust in the inner regions of the disk; as shown in D'Alessio et al. (2006), 60% of the 24 μm emission is coming from inside 10 AU when the dust has not settled towards the midplane. The percentage of emission coming from within 10 AU increases when observing at the shorter IRAC wavelengths, or when observing a disk in which some degree of dust settling has occurred.

Among the CTTS (circles) in Figure 2.12, we find tentative correlations between FUV luminosity and each of the disk evolution tracers, with the most convincing

correlation in $J-K$. However, we are likely observing two quantities which correlate with L_{acc}. We showed in Figure 2.7 that the sources with highest FUV luminosities are also the strongest accretors. Disk properties also depend on the accretion rate through the disk and the IR spectral energy distributions reflect this; models predict that lower $\dot{M}$'s will produce bluer IR colors and that the IR spectrum becomes increasingly flatter as $\dot{M}$ increases (D'Alessio et al., 2006; Espaillat, 2009). Therefore, it is likely that these apparent trends are a result of accretion affecting both the FUV luminosities and the tracers of dust in the disk instead of a consequence of direct processing of the dust by FUV radiation. This seems to indicate that if it is the FUV that is responsible for gas dispersal, the gas and dust are evolving independently. Supporting this conclusion, the transitional (Calvet et al., 2002, 2005; Kim et al., 2009) and pre-transitional (Espaillat et al., 2008, 2010) disks, the sources likely to have undergone dust processing and evolution, have the same FUV luminosities as the full disks, indicating that the FUV is not likely having a strong effect on the dust.

2.5 Summary and Conclusions

We present new observations of T Tauri stars in the Chamaeleon I and II and the 25 Ori star forming regions. Included are *Chandra* X-ray and ACS/SBC FUV observations which provide constraints on the photoevaporative fluxes present in young stars. Combined with previously published X-ray and FUV observations, we explored the evolution of high energy radiation fields with the following results:

- With the addition of ∼40 sources with X-ray observations in the 7–10 Myr 25 Ori star forming association, a significant addition to the ∼25 previously observed 6–10 Myr T Tauri stars (above the substellar limit), we confirm results that there is no decay in the X-ray luminosity between 1 and 10 Myr. With consistently strong X-ray radiation fields, disk photoevaporation, if driven by X-rays, should proceed on short timescales. However, observations of sources with remaining disk gas emission and strong X-ray luminosities at 7–10 Myr and previous observations of TW Hya (a source with a transitional disk and

strong X-ray luminosity) still cannot be explained by X-ray photoevaporation.

- We show, for the first time, the observed evolution of the FUV radiation fields in pre-main sequence stars from 1 Myr to 1 Gyr. We find that the FUV luminosity decline can be explained, in part, by the decline of the accretion rate onto the star but note that some FUV emission must come from an additional source which is likely gas in the inner disk regions. If FUV drives photoevaporation of the gas disk, the diversity of disks observed at 1 Myr can be understood by the large range of $\dot{M}$'s observed at 1 Myr. However, gas disks at 7–10 Myr require additional explanation, as viscous $\dot{M}$ evolution predicts that these sources should have had strong FUV radiation in the past, so disk dispersal by FUV radiation should have proceeded quickly.

- We show that the power law relations for the decay of high energy radiation fields in solar type active stars described by Ribas et al. (2005) extend to the significantly younger sample discussed here. With both the X-ray luminosities and the slope of the FUV relation accurately predicted, we expect that the difficult to observe EUV radiation fields will similarly obey the power law trends. This result tells us that strong radiation fields, necessary to remove the gas, are present throughout the disk dispersal phase.

- We find no correlation between FUV luminosities and tracers of dust evolution in the disk and furthermore, we find that sources with significant dust processing, the transitional disks, have similar FUV luminosities to full disk sources. Therefore, if FUV radiation is the key emission field in gas evolution, it is not driving the dust depletion. This would indicate that gas and dust evolution occur independently, though interestingly on similar timescales.

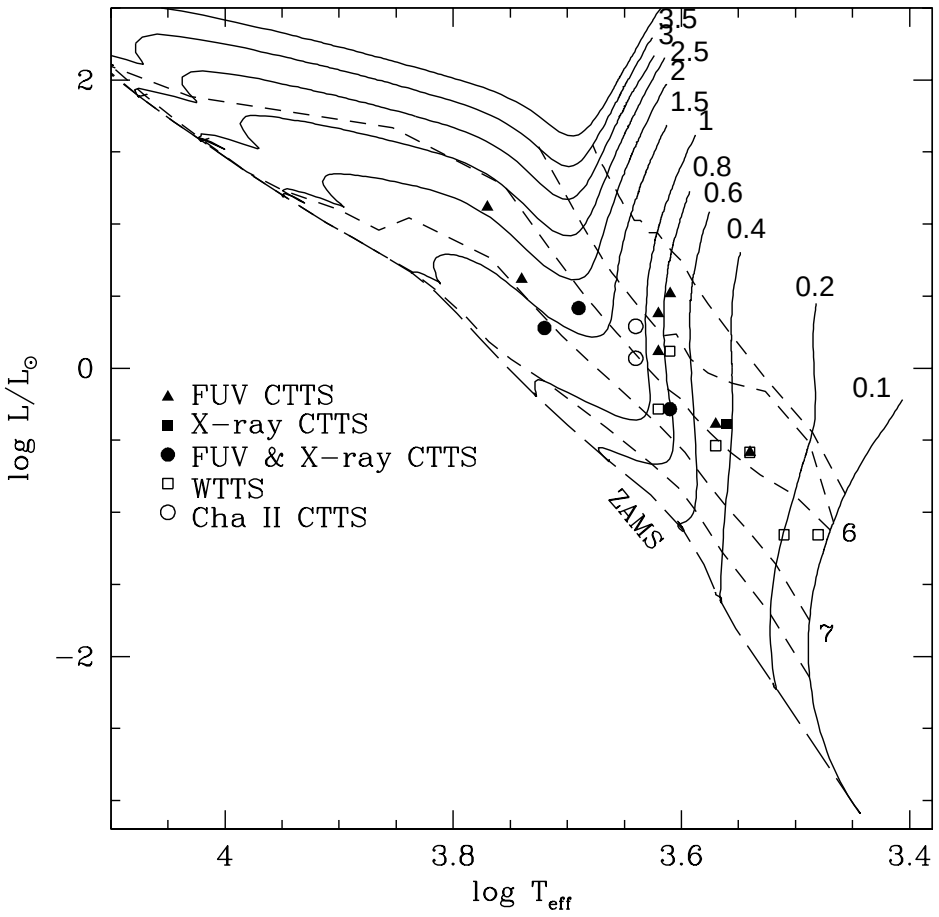

Figure 2.1. H-R diagram of X-ray and FUV samples of Chamaeleon sources. We show the locations on the H-R diagram of Chamaeleon I X-ray and FUV sources and identify those with both X-ray and FUV observations. All WTTS were observed in X-rays and do not have FUV spectra. We also show the location of the older Chamaeleon II sources which were observed with ACS/SBC. Solid lines are evolutionary tracks from Siess et al. (2000) and are labeled in units of solar masses. Dashed lines are isochrones and correspond to log age = 5.5, 6, 6.5, 7, and 7.5 years.

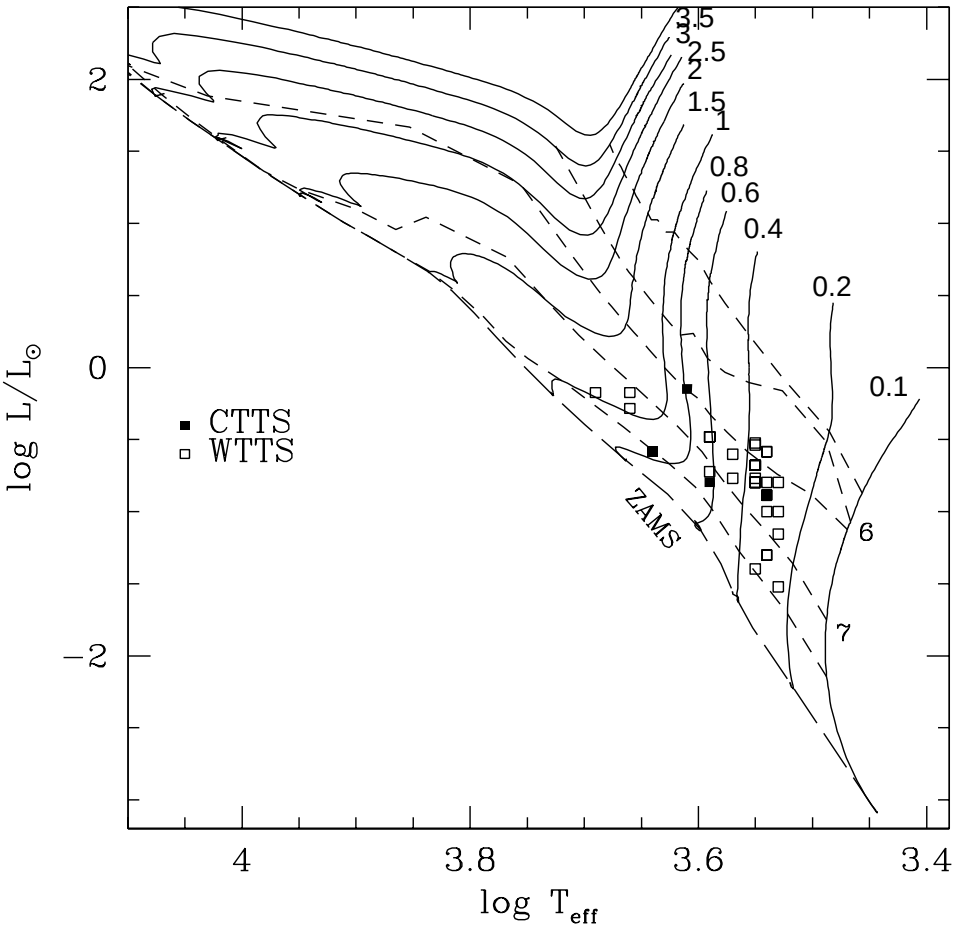

Figure 2.2. H-R diagram of 25 Ori association X-ray detections. We show the location of all 25 Ori X-ray sources on the H-R diagram with evolutionary tracks and isochrones as defined in Figure 2.1. Sources fall primarily between the 6.5 and 7 Myr isochrones with earlier (hotter) sources appearing older due to birth line effects (Hartmann, 2003).

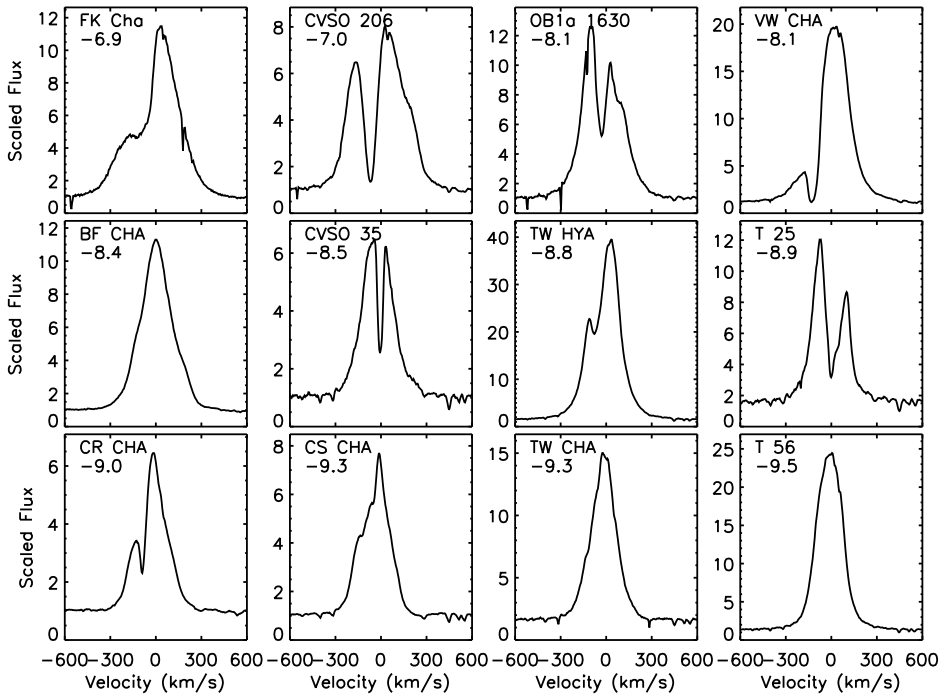

Figure 2.3. Hα line profiles from MIKE. We show the accreting sources in our sample which have MIKE observations, ordered by log $\dot{M}$ (listed below each source name) calculated from the 10% line width relation of Natta et al. (2004). The 7–10 Myr sources, CVSO 206, OB1a 1630, and CVSO 35, have remarkably wide and asymmetric Hα profiles, indicating that accretion is strong and gas remains in the inner circumstellar disk (Chapter 3).

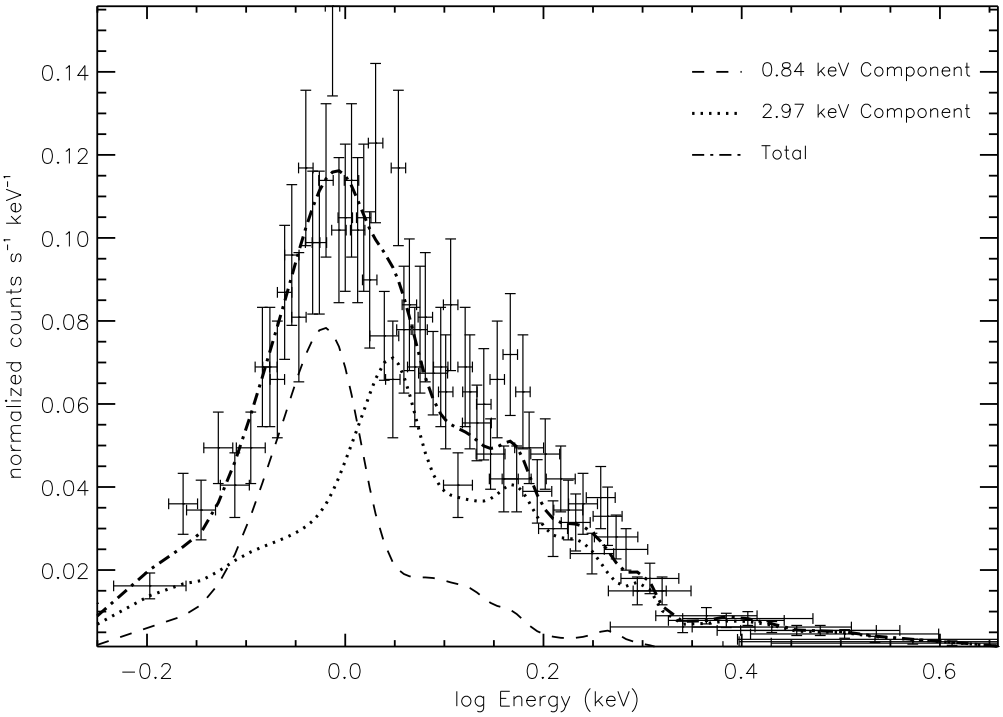

Figure 2.4. *Chandra* ACIS spectrum of the accretor CR Cha. We show the extracted spectrum of CR Cha (the source with the highest counts in our sample) along with our best APEC model fit to the spectrum.

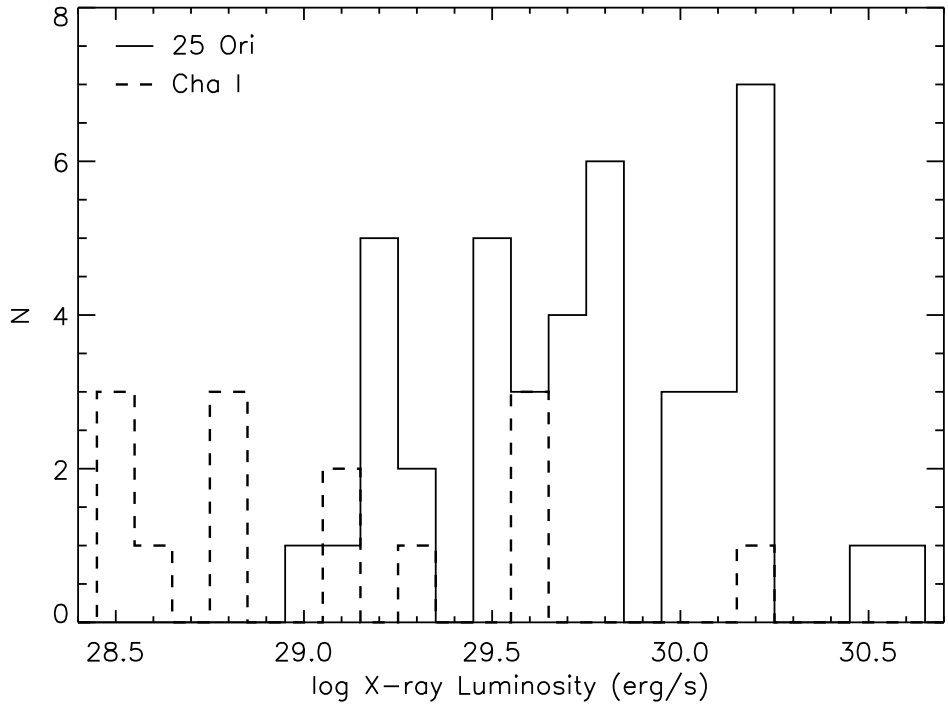

Figure 2.5. Distributions of X-ray luminosities for 25 Ori and Chamaeleon I samples. The distribution of X-ray luminosities, corrected for absorption, in each sample does not reproduce the lognormal shape of the X-ray luminosity function found for COUP sources in Feigelson et al. (2005). This indicates that our samples are likely incomplete in mass. For this reason we supplement our Chamaeleon I observations with previous X-ray observations; however, no additional X-ray observations exist for 25 Ori.

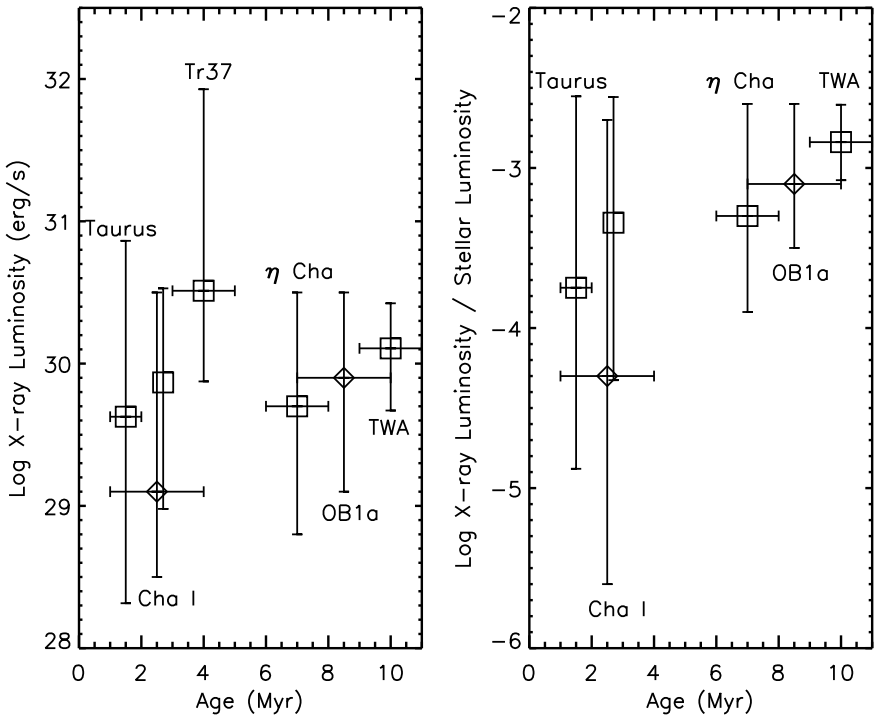

Figure 2.6. X-ray properties of young star forming associations. *Left:* Median X-ray luminosities of young star forming associations versus age. For each association, we plot the median and the full range in X-ray luminosity for sources with spectral types K5 and later. The diamonds represent X-ray luminosities calculated in this work and the boxes represent those taken from the literature: Taurus (Güdel et al., 2007), Cha I (Feigelson et al., 1993), Trumpler 37 (Mercer et al., 2009), η Cha (López-Santiago et al., 2010), TWA (Voges et al., 1999, 2000). We include the sample of Feigelson et al. (1993) for Cha I (offset in age for clarity) because with only two fields observed here, the Cha I sample was limited. Our Cha I observations reproduce the range observed by ROSAT well and actually probe dimmer X-ray sources. *Right:* Normalized X-ray luminosity versus age. Here we divide the observed X-ray luminosities by the stellar luminosities to normalize by spectral type. Both figures show that between 1 and 10 Myr, there is no decline in X-ray luminosity.

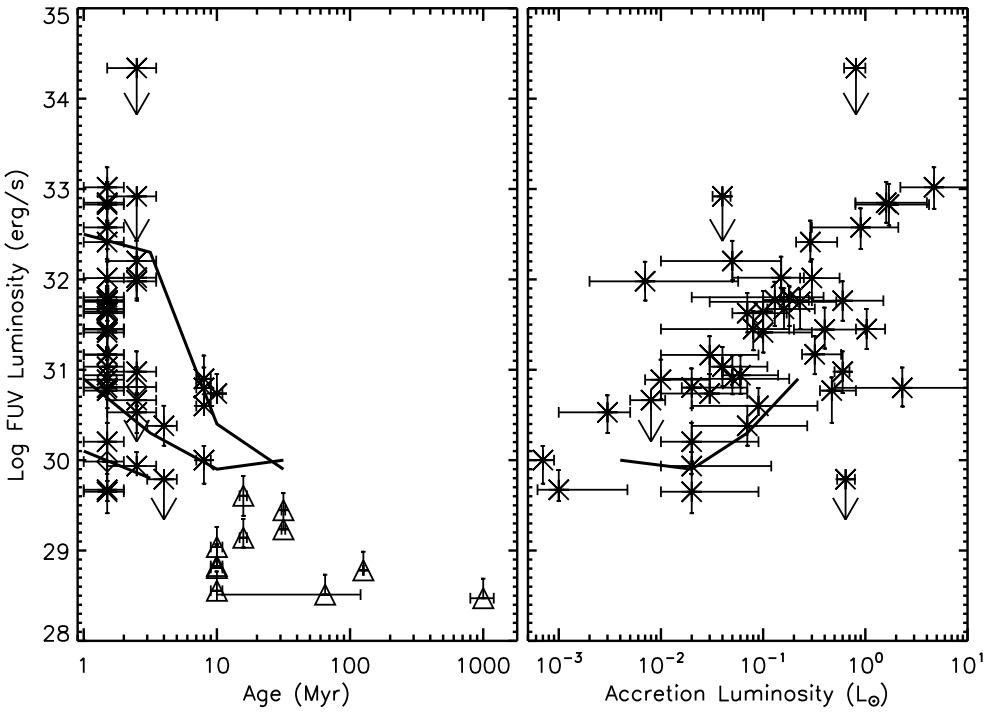

Figure 2.7. FUV luminosities of young star forming associations. X-ray properties of young star forming associations]*Left:* FUV luminosity versus age for young low-mass stars from the T Tauri phase up to 1 Gyr. The FUV luminosity of CTTS, displayed as asterisks when accretion rates are known and diamonds when they are not, is observed to decrease with age until becoming entirely chromospheric in WTTS (triangles). Upper limits were calculated for non-detections, primarily sources with high A_V, and are represented by downward arrows. Solid lines show the predicted FUV luminosity produced in an accretion shock onto the stellar surface (Calvet & Gullbring, 1998) as the source evolves and $\dot{M}$ decreases. The top and bottom lines are calculated for the observed range in $\dot{M}$ at each age and the middle line is calculated from $\dot{M}$ predictions in which a 0.8 $M_\odot$ CTTS with an initial disk mass of 0.1 $M_\odot$ evolves viscously (Hartmann et al., 1998; Calvet et al., 2005). *Right:* FUV luminosity versus L_{acc}. The solid line shows the predictions of FUV luminosity from accretion onto the 0.8 $M_\odot$ CTTS through the viscously evolving disk. Here, we omit the predicted FUV luminosities for the upper and lower limits of observed $\dot{M}$'s, which were shown on the left.

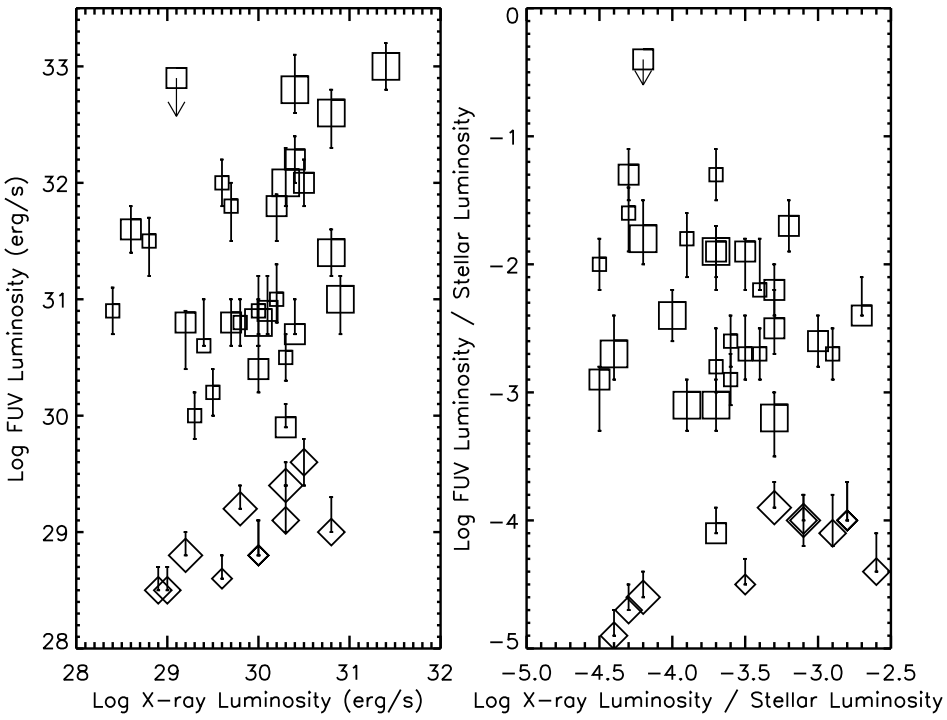

Figure 2.8. X-ray versus FUV luminosities. *Left:* Comparison of total FUV and X-ray luminosities. Boxes represent accreting sources and diamonds represent non-accreting sources. The largest symbols are G stars, medium symbols are K stars and the smallest symbols are M stars. There is no correlation between FUV and X-ray luminosities among this sample; however, the non-accretors have the lowest FUV luminosities. The subset of non-accretors has weakly correlated total X-ray and FUV luminosities. *Right:* Comparison of fractional X-ray and FUV luminosities. Again, no correlation is observed but non-accretors have the lowest fractional FUV luminosities. One CTTS, CR Cha, appears in the region populated by non-accretors (< -3.5). We note that this is the only Chamaeleon I source with $A_V = 0$.

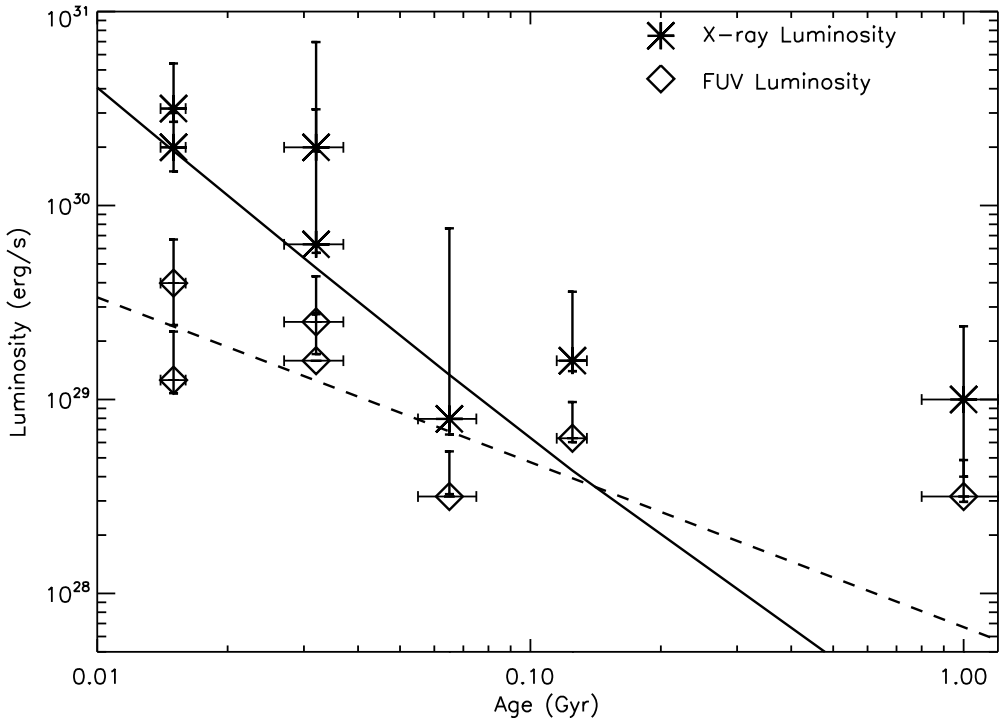

Figure 2.9. The luminosity of young solar analogs compared to power law relations of high energy radiation fields derived in Ribas et al. (2005). The solid line shows the luminosities predicted for the summed 1– 20 Å and the 20-100 Å flux bins as defined by Ribas et al. (2005), approximately the same wavelength region as our 0.2-10 keV observations. The dashed line shows the slope of the predicted fluxes from the 920–1180 Å wavelength bin but scaled vertically in luminosity to fit the FUV luminosities of our longer wavelength observations. The slope of the FUV power law relation provides a good fit to our observed FUV luminosities. The predictions fail to fit the 1 Gyr source in both the X-ray and FUV regimes.

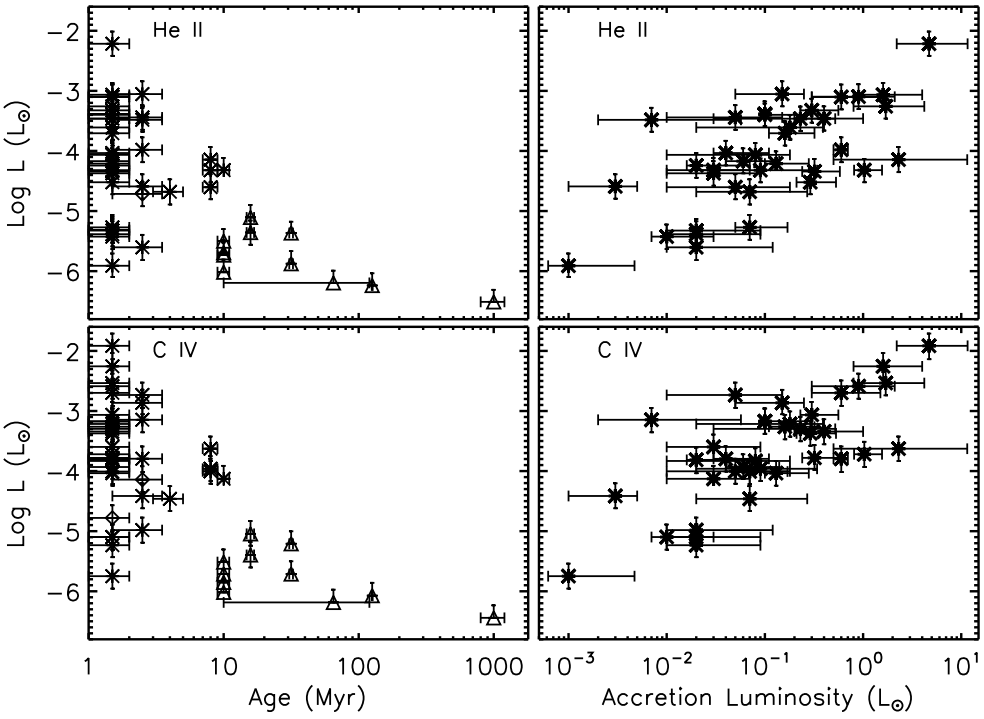

Figure 2.10. He II and C IV versus age and accretion properties. *Top Left:* He II λ1640 Å luminosity versus age. *Bottom Left:* C IV λ1549 Å line luminosity versus age. Symbols are defined as in Figure 2.7. In both cases the luminosity of the line is observed to decrease with age. *Top Right:* He II λ1640 Å luminosity versus L_{acc}. *Bottom Right:* C IV λ1549 Å line luminosity versus L_{acc}. Both He II and C IV are correlated with L_{acc}.

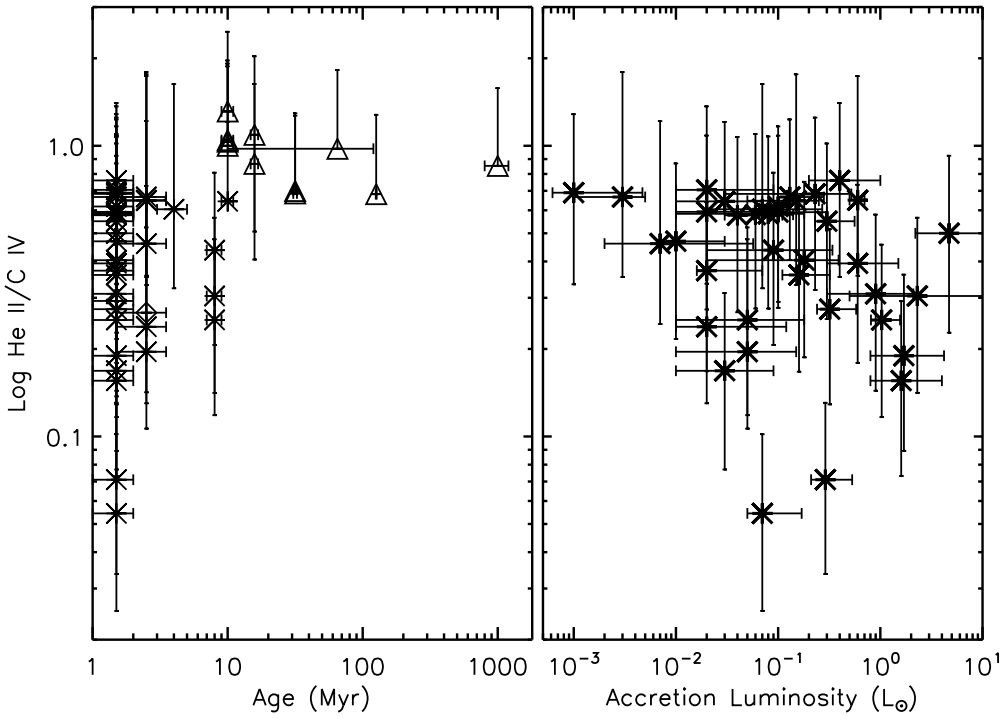

Figure 2.11. Ratio of He II to C IV as a function of age and accretion properties. Symbols are defined as in Figure 2.7. We see that the non-accretors clearly have a higher value of He II/ C IV, approximately 1, while the CTTS have He II/ C IV < 1; however, we see no clear trend with accretion luminosity.

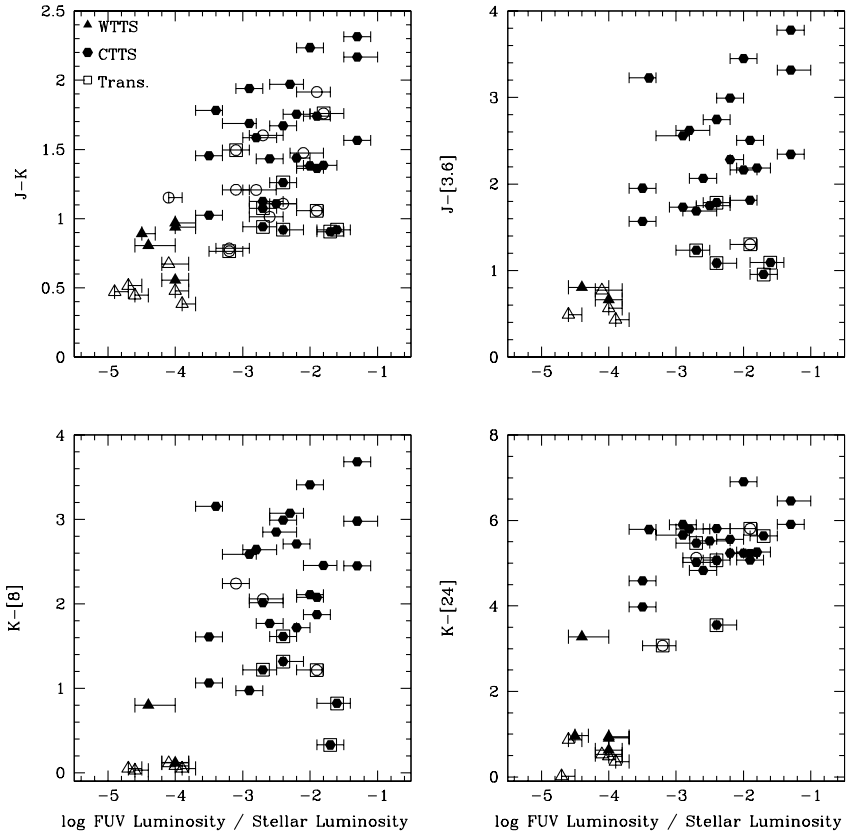

Figure 2.12. FUV radiation and tracers of disk evolution. We compare the FUV luminosities to several indicators of evolution in the disk. [3.6], [8], and [24] represent IRAC and MIPS photometry at 3.6, 8, and 24 μm respectively. Open symbols are sources with spectral types earlier than K5 and closed symbols are spectral types K5 and later. J-[3.6], K-[8], and K-[24] probe regions progressively further in the disk. We see only tentative correlations between high energy emission and dust evolution tracers, but this is likely due to both quantities being dependent on accretion rate. We do see that the full and transitional or pre-transitional disks (boxed symbols) have similar FUV luminosities, indicating that the FUV radiation is not very significant in dust evolution.

Table 2.1: Properties of X-ray and FUV Samples

Source	SpT	L_X ($L_\odot$)	L_{FUV} ($L_\odot$)	L_* ($L_\odot$)	L_{acc} ($L_\odot$)	Reference[a,b]
Taurus						
AA Tau	M0	*1.3×10^{-4}*	0.016	*1.0*	*0.13*	1, 15
BP Tau	K7	*4.1×10^{-4}*	0.016	*1.3*	*0.23*	1, 15
CI Tau	K6	*4.1×10^{-5}*	1.6×10^{-3}	*1.3*	*0.47*	1, 15
DE Tau	M1	–	0.013	*1.3*	*0.16*	1
DL Tau	K7	–	4.1×10^{-3}	*1.0*	*0.32*	1
DM Tau	M1	*1.6×10^{-5}*	8.3×10^{-3}	*0.33*	*0.08*	1, 15
DN Tau	M0	*4.1×10^{-4}*	2.6×10^{-3}	*1.3*	*0.04*	1, 15
DO Tau	M0	–	0.066	*1.3*	*0.29*	1
DP Tau	M0	*6.6×10^{-6}*	2.1×10^{-3}	*0.21*	*0.01*	1, 15
DR Tau	K7	–	8.3×10^{-3}	*1.6*	*1.03*	1
FM Tau	M0	*1.0×10^{-4}*	0.026	*0.52*	*0.30*	1, 15
FP Tau	M3	–	1.3×10^{-4}	*0.41*	*0.001*	1
GK Tau	M0	*2.6×10^{-4}*	2.1×10^{-3}	*1.3*	*0.06*	1, 15
GM Aur	K3	–	0.016	*1.3*	*0.18*	1
HN Tau A*	K5	*1.0×10^{-5}*	0.010	*0.21*	*0.02*	1, 15
HN Tau B*	M4	–	2.6×10^{-4}	*0.033*	–	1
IP Tau	M0	*1.6×10^{-4}*	1.6×10^{-3}	*0.66*	*0.02*	1, 17
LkCa 15	K5	–	4.1×10^{-3}	*1.0*	*0.03*	1
RY Tau	G1	*6.6×10^{-4}*	0.16	*10.4*	*1.6*	1, 15
SU Aur	G1	*1.6×10^{-3}*	6.6×10^{-3}	*8.3*	*0.10*	1, 15
T Tau	G6	*1.6×10^{-3}*	0.10	*8.3*	*0.90*	1, 15
UZ Tau A*	M1	–	1.3×10^{-4}	*0.33*	*0.02*	1
UZ Tau B*	M2	*8.3×10^{-5}*	4.1×10^{-4}	*0.33*	*0.02*	1, 15
Orion						
CO Ori	G0	–	0.16	*20.8*	*1.7*	1
EZ Ori	G3	–	0.10	*6.7*	*0.10*	1
GW Ori	G0	*6.6×10^{-3}*	0.26	*65.7*	*4.7*	1, 16
P 2441	F9	–	6.6×10^{-3}	*10.4*	*0.4*	1
V1044 Ori	G2	–	0.016	*6.7*	*0.6*	1
Chamaeleon I						

Continued on Next Page...

Table 2.1 – Continued

Source	SpT	L_X	L_{FUV}	L_*	L_{acc}	Reference[a,b]
CHXR 8	K2	2.1×10^{-5}	–	–	–	13
CHXR 30A	K8	1.0×10^{-4}	–	*1.3*	0	2, 3
CHXR 30B	M1	8.3×10^{-6}	–	*0.21*	0	2, 3
CR Cha	K2	5.2×10^{-4}	2.1×10^{-4}	*2.6*	0.02	3
CS Cha	K6	*8.3×10^{-4}*	0.026	*1.3*	0.01	2, 3, 18
DI Cha	G2	*5.2×10^{-4}*	0.026	*13.1*	0.15*	3, 17
FK Cha	K6	–	<5.2	*2.6*	1.2	3
FL Cha	K8	3.3×10^{-5}	<0.21	*0.52*	*0.04*	2, 3, 8
FO Cha	M2	2.1×10^{-5}	–	*0.41*	*0.01*	2, 3, 8
HN 7	M5	8.3×10^{-6}	–	*0.066*	0	2, 3
HN 12W	M6	8.3×10^{-6}	–	*0.066*	0	2, 3
ISO 86	–	2.1×10^{-5}	–	–	–	
ISO 91	M3	6.6×10^{-4}	–	*0.26*	–	2, 3
ISO 97	M1	3.3×10^{-5}	–	–	–	2
ISO 196	K7	1.0×10^{-5}	–	–	–	
SY Cha	K6	1.0×10^{-4}	–	*0.52*	0.002	2, 3
SZ Cha	K0	2.6×10^{-4}	1.6×10^{-3}	*2.1*	–	3
T25	M3	–	$<1.3 \times 10^{-3}$	*0.26*	0.01	2, 3
T54	G8	*2.1×10^{-3}*	2.6×10^{-3}	*4.1*	0.58*	3, 18
T56	M1	*5.2×10^{-4}*	8.3×10^{-4}	*0.41*	0.003	2, 3, 17
TW Cha	K8	1.0×10^{-4}	–	*0.52*	0.01	2, 8
VW Cha	K8	*6.6×10^{-4}*	0.041	*3.3*	0.05	2, 3, 18
Chamaeleon II						
BF Cha	K5	*2.6×10^{-4}*	6.6×10^{-4}	*2.1*	0.07	4, 17
BM Cha	K5	–	$< 1.6 \times 10^{-4}$	*1.3*	*0.64*	4
25 Ori						
CVSO 24	M2	8.3×10^{-5}	–	*0.16*	*0.01*	5, 10, 12
CVSO 29	M3	1.0×10^{-4}	–	*0.26*	–	5, 10, 12
CVSO 34	M0	4.1×10^{-4}	–	*0.21*	0	5, 9
CVSO 35	K7	3.3×10^{-4}	2.1×10^{-3}	*0.66*	0.05	5, 10, 12
CVSO 36	M2	3.3×10^{-4}	–	*0.21*	*0.03*	5, 10, 12
CVSO 38	M2	4.1×10^{-4}	–	*0.16*	*0.02*	5, 10, 12
CVSO 39	M2	2.1×10^{-4}	–	*0.33*	*0.01*	5, 12

Continued on Next Page...

Table 2.1 – Continued

Source	SpT	L_X	L_{FUV}	L_*	L_{acc}	Reference[a,b]
CVSO 43	M2	1.3×10^{-4}	–	*0.26*	*0.02*	5, 12
CVSO 200	M3	4.1×10^{-4}	–	0.21	–	11, 12
CVSO 206	K7	1.3×10^{-4}	1.6×10^{-3}	0.26	2.3	10, 11, 12
CVSO 207	K6	4.1×10^{-4}	–	0.66	–	10, 11, 12
CVSO 211	K4	3.3×10^{-4}	–	0.52	–	10, 11, 12
CVSO 214	K2	2.1×10^{-4}	–	0.66	–	10, 11, 12
CVSO 217	M1	2.1×10^{-4}	–	>0.26	–	11, 12
CVSO 218	M4	1.3×10^{-4}	–	0.13	–	10, 11, 12
CVSO 223	M3	2.1×10^{-4}	–	0.21	–	10, 11, 12
CVSO 224	M4	5.2×10^{-5}	2.6×10^{-4}	0.13	7×10^{-4}	6, 10, 11, 12
CVSO 225	M4	2.1×10^{-4}	–	0.26	–	10, 11, 12
CVSO 228	M2	8.3×10^{-5}	–	0.16	–	10, 11, 12
CVSO 230	M1	2.6×10^{-4}	–	0.33	–	10, 11, 12
CVSO 233	M3	1.3×10^{-4}	–	0.052	–	10, 11, 12
CVSO 235	M3	2.1×10^{-4}	–	0.16	–	10, 11, 12
OB1a 532	M3	2.6×10^{-4}	–	0.26	–	11, 12
OB1a 735	M5	3.3×10^{-5}	–	>0.21	–	11, 12
OB1a 834	M2	8.3×10^{-5}	–	0.16	–	11, 12
OB1a 841	M3	2.6×10^{-4}	–	0.16	–	11, 12
OB1a 849	M5	8.3×10^{-5}	–	0.16	–	11, 12
OB1a 948	M3	1.0×10^{-4}	–	0.13	–	11, 12
OB1a 981	K3	5.2×10^{-4}	–	0.83	–	11, 12
OB1a 1088	K6	5.2×10^{-4}	–	>0.52	–	11, 12
OB1a 1253	M4	8.3×10^{-5}	–	0.10	–	11, 12
OB1a 1586	M5	5.2×10^{-5}	–	0.066	–	11, 12
OB1a 1626	K8	4.1×10^{-4}	–	>0.83	–	11, 12
OB1a 1630	M2	6.6×10^{-5}	1.0×10^{-3}	0.16	0.09	11, 12
OB1a 1663	M5	4.1×10^{-5}	–	0.10	–	11, 12
OB1a 1755	M3	1.0×10^{-4}	–	0.21	–	11, 12
RX J0526.7+0143	K0	1.0×10^{-3}	–	–	–	14
J05244498+0159465	K6	8.3×10^{-4}	–	0.66	–	11
J05260639+0137116	M2	6.6×10^{-5}	–	0.041	–	11
J05263125+0141492	M4	5.2×10^{-5}	–	0.033	–	11

Continued on Next Page...

Table 2.1 – Continued

Source	SpT	L_X	L_{FUV}	L_*	L_{acc}	Reference[a,b]
TWA						
TW Hya	K7	*6.6 × 10⁻⁴*	1.3×10^{-3}	*0.32*	0.03	1, 16
HD 98800	K5	*1.6 × 10⁻³*	2.6×10^{-5}	*0.66*	0	1, 16
TWA 7	M1	*1.0 × 10⁻⁴*	1.0×10^{-5}	*0.32*	0	1, 16
TWA 13A	M1	*2.6 × 10⁻⁴*	1.6×10^{-5}	*0.16*	0	1, 16
TWA 13B	M1	*2.6 × 10⁻⁴*	1.6×10^{-5}	*0.16*	0	1, 16
Field						
HD 12039	G4	*1.6 × 10⁻⁴*	4.1×10^{-5}	*0.33*	0	1, 16
HD 202917	G5	*5.2 × 10⁻⁴*	6.6×10^{-5}	*0.66*	0	1, 16
HD 53143	K1	*2.6 × 10⁻⁵*	8.3×10^{-6}	*0.66*	0	7, 16
HD 61005	G8	*4.1 × 10⁻⁵*	1.6×10^{-5}	*0.66*	0	1, 19
HD 92945	K2	*2.1 × 10⁻⁵*	8.3×10^{-6}	*0.41*	0	1, 16
MML 28	K2	*5.2 × 10⁻⁴*	3.3×10^{-5}	*0.41*	0	1, 16
MML 36	K5	*8.3 × 10⁻⁴*	1.0×10^{-4}	*1.0*	0	1, 16

Note: Values in italics were taken from the literature while those in regular font were derived in this work. Sources in bold were observed with STIS rather than ACS/SBC.

[a]Spectral type, stellar, and accretion luminosity references. 1) Chapter 3 and references therein, 2) Luhman (2004), 3) Luhman (2007), 4) Spezzi et al. (2008), 5) Calvet et al. (2005), 6) Espaillat et al. (2008), 7) Kalas et al. (2006), 8) Nguyen et al. (2009), 9) Briceño et al. (2005), 10) Briceño et al. (2007), 11) Briceño et a. (2010), 12) Hernández et al. (2007b), 13) Huenemoerder et al. (1994), 14) Alcala et al. (1996)

[b]X-ray luminosity references. 15) Güdel et al. (2007), 16) Voges et al. (1999), 17) Voges et al. (2000), 18) Feigelson et al. (1993), 19) Wichmann et al. (2003)

*L_{acc}'s for T26 and T54 were calculated from the U band excess, whereas the remaining Chamaeleon sources have L_{acc} calculated using Hα 10% equivalent widths observed here or taken from the literature.

Table 2.2: X-ray Detections: Possible and Confirmed T Tauri Members

2MASS Source	SpT	EW Hα	EW Li 6706 Å	log L_X
05243490+0154207	K4–K5	-0.46	0.10	29.0
05244265+0154116	G9–K0	1.54	0.32	–
05244320+0200355	–	–	–	–
05251394+0143313	–	–	–	–
05265823+0136078	–	–	–	–
05270173+0139157	K6	-0.39	0.17	29.3
10575375-7724495	–	–	–	–

Note: Spectral types were determined using the Ca I absorption lines. With the early spectral type, additional membership confirmation is needed for 2MASS 05244265+0154116 as Li is not a good indicator.

Table 2.3: X-ray Spectral Analysis

Source	Net Counts	N_H (10^{21} cm^{-2})	kT_1 (keV)	kT_2 (keV)	χ^2_{red}	Flux (erg s^{-1} cm^{-2})
CR Cha	1996	0.8	0.84	2.97	0.95	1.4×10^{-12}
CHXR 30A	324	12.2		2.14	1.01	4.6×10^{-13}
SY Cha	283	0.8	0.34	2.94	0.81	2.4×10^{-13}
SZ Cha	692	0.8	0.85	4.53	0.74	3.7×10^{-13}
TW Cha	313	0.8	0.41	1.95	1.08	1.8×10^{-13}
CVSO 38	266	1.1	0.98	6.98	1.42	4.1×10^{-13}
J05244498+0159465	285	1.1	0.32	1.59	2.06	2.5×10^{-13}
RX J0526+0143	369	1.1	0.31	1.48	2.29	2.6×10^{-13}

CHAPTER 3

Far-Ultraviolet H_2 Emission from Circumstellar Disks

3.1 Introduction

Gas comprises 99% of the mass of primordial disks. As time increases, it is accreted onto the star, formed into planets, and lost by photoevaporation, leaving behind a debris disk, in which most of the mass is locked into planets and other solid bodies traced by secondary dust arising from collisions. Although the general outline of this process is agreed upon, many specific questions remain unanswered, mainly because the gas is difficult to observe. As a result, only $\sim$1% of the disk mass, the dust, has been used as a probe of the disk evolution. However, although interconnected, the evolution of gas and dust may take different paths (Pascucci et al., 2009), making observations of the gas itself necessary to understand these processes. Of particular importance are observations of the gas in the inner disk, because it sets the chemical and physical conditions for planet formation. The bulk of the gas in these cold disks is in H_2, which can survive in hot gas up to $\sim$4000 K, given typical disk densities (Herczeg et al., 2002). H_2 lacks a permanent dipole moment and has wide energy spacings, so the pure rotational and rovibrational lines are weak. Nonetheless, extensive surveys of these lines in primordial disks have been carried out (Bary et al. 2008; Bitner et al. 2008, and references therein), and they have been detected in a handful of objects. Searches using less abundant molecules have also succeeded and provided information on the gas in the inner region of gas-rich disks (Carr & Najita, 2008; Salyk et al., 2008; Pascucci et al., 2009; Najita et al., 2008). Gas has also been searched for in disks of more evolved sources which are no longer accreting, within the age range when the transition from primordial to debris is supposed to happen,

$\sim$5 - 20 Myr. In particular, Pascucci et al. (2006) looked for H_2 in the disks of several non-accreting sources and found that the amount of gas still present at 5 - 20 Myr is not large enough to form the gas giant planets at that time. This observation agrees with results indicating that the amount of hot gas in disks of non-accreting sources is decreased when compared to accreting sources (Carmona et al., 2007).

UV observations are very promising for detecting the gas. The strong stellar Lyα radiation bathes the UV thin regions of the circumstellar material and, as long as the H_2 has a temperature of a few thousand degrees, the line excites electrons to upper electronic states, which produces a plethora of emission lines in the UV when they de-excite (Herczeg et al., 2006, H06, and references therein). At the same time, the stellar high energy radiation fields eject electrons from heavy metals, and the resulting free electrons produce additional electrons by ionizing H and He atoms; these secondary electrons then excite H_2 to upper levels, resulting in a characteristic spectrum of lines and continuum in the UV (Spitzer & Tomasko, 1968; Bergin et al., 2004, B04). For electron excitation to work efficiently, temperatures need to be high enough for neutral H to be present. The relatively high temperature requirements mean that the H_2 detected by these means must either to be close to the star or to be excited by shocks. UV H_2 emission has been found to be extended in objects surrounded by substantial natal material, in the regions where the stellar outflow shocks this material, or in fast accretors, where the H_2 may arise in the high density outflow itself (H06). However, without remnant envelopes such as the objects in this study, the only known exception being T Tau, the most likely place to find the required high temperatures is in the inner disk. This makes the UV H_2 emission ideal for probing the H_2 gas in the innermost regions of disks, regions which are difficult to access by other means.

We obtained ACS/SBC prism spectra of a fair number of accreting Classical T Tauri stars (CTTS), non-accreting weak T Tauri stars (WTTS), and more evolved disks (DD), covering the interesting age range, $\sim$1 - 100 Myr. Our goal was to search for UV H_2 emission and study its evolution. The poor spectral resolution of the ACS spectra made the identification of Lyα fluorescent lines impossible. However, we

were able to identify a feature around ~ 1600 Å, first proposed by B04 as due mostly to electron impact excitation of H_2. In this chapter we present and analyze these spectra. We show that the H_2 feature is absent in all non-accreting and evolved stars while present in all accreting stars, and use UV fluxes to give very rough estimates of upper limits for the remaining surface density of H_2 in the latter.

3.2 Observations

We obtained observations of 20 CTTS and 10 non-accreting and evolved targets using the Advanced Camera for Surveys Solar Blind Channel (ACS/SBC) on the Hubble Space Telescope in 2007. The observations were obtained in GO programs 10810 (PI: Bergin), 10840 (PI: Calvet) and 11199 (PI: Hartmann). Each ACS observation consists of a brief image in the F165LP filter and a longer image obtained with the PR130L prism. Images appear unresolved. Offsets between the target location in the filter and prism image, including the wavelength solution, were obtained from Larsen (2006). The target spectrum was then extracted from a 41-pixel (1.3") wide extraction window. Background count rates of 0.05 - 0.1 counts s^{-1} were calculated from offset windows and subtracted from the extracted spectrum. The absolute wavelength solution was then determined by fitting the bright C IV λ1549 Å doublet. Fluxes were calibrated from the sensitivity function obtained from white dwarf standard stars by Bohlin (2007). The spectra range from 1230–1900 Å with a 2-pixel resolution of ~ 300 at 1230 Å and ~ 80 at 1600 Å.

Table 3.1 lists the ACS targets used in this analysis and the properties of these objects. The CTTS sources include 16 objects in the Taurus-Auriga molecular cloud and four sources in the 25 Ori aggregate in the Orion OB1a subassociation. Spectral types for the CTTS in Taurus are from Furlan et al. (2006), and ages from Hartmann (2003). To correct for reddening we used the law towards the star HD 29647 (Whittet et al., 2004) and estimated A_V by de-reddening the median photometry of Herbst et al. (1994) to fit the fluxes of a standard star in the region of the spectrum (V to J bands)

where the emission is mostly photospheric[1]. We obtained accretion luminosities L_{acc} for the Taurus sources using the U band excesses following Gullbring et al. (1998), and the median U from photometry in Herbst et al. (1994). The ages, spectral types, luminosities, A_V's, and L_{acc} for the sources in 25 Ori were taken from Briceño et al. (2007); Hernández et al. (2007b) and Calvet et al. (2005).

The non-accreting sources (WTTS/DD) were selected to have no evidence of accretion and to have excesses in either Spitzer Space Telescope Infrared Spectrograph (IRS) spectra or 24 and 70 μm Multiband Imaging Photometer (MIPS) photometry, indicating the presence of debris disks. The sources in the TW Hydrae Association have been identified as WTTS by spectral observations which showed Hα in emission (Webb et al., 1999) and strong Li 6707 in absorption (Kastner et al., 1997). The WTTS/DD and their properties were discussed in Carpenter et al. (2009, 2008), Hillenbrand et al. (2008), Verrier & Evans (2008), Chen et al. (2005) and Low et al. (2005). Examples of the ACS target spectra are shown in Figure 3.1.

We supplemented the ACS data with previously published medium and high resolution STIS data of CTTS (Calvet et al., 2004; Herczeg et al., 2002, 2004, B04). The source properties, listed in Table 3.1, were taken from Calvet et al. (2004) for the Orion Molecular Cloud sources, and derived as described for the ACS Taurus sources for the STIS Taurus sources. We adopt the spectral type and age from Webb et al. (1999) and A_V from Herczeg et al. (2004) for TW Hya. Accretion luminosities for the STIS sample were taken from Calvet et al. (2004).

3.3 Results

Following B04, we identified a feature in the STIS spectra at 1600 Å which is due mostly to electron impact H_2 emission. Due to the low resolution of the ACS spectra, we used the high resolution spectrum of TW Hya (Herczeg et al., 2004) to identify this feature in the ACS spectra; in Figure 3.2 we compare the feature in the observed

[1]Targets with high mass accretion rate, as DL Tau and DR Tau show significant veiling at J (Edwards et al., 2006), so the estimated extinction may be in error, although it is consistent with values from Taurus.

STIS spectrum of TW Hya and in the STIS spectrum smoothed to the resolution of the ACS spectra. While the H_2 lines are no longer observable in the smoothed spectrum, the feature at 1600 Å is.

In addition to electron impact H_2 emission, the flux at 1600 Å has contributions from accretion shock emission and Lyα fluorescent lines. Attempting to isolate an indicator that is due to electron impact H_2 emission, we measured the flux between 1575 and 1625 Å and subtracted from it the continuum and the contribution from nearby strong lines (He II 1640 Å and C IV 1550 Å). Since it is unclear how strong the emission from additional sources is at 1600 Å, we calculated the continuum in three ways. First, by joining the troughs in the spectrum on either side of the 1600 Å feature; second, by fitting a 5th order polynomial to the entire FUV spectrum; third, by adopting a continuum which assumes that the rise in the spectrum at 1600 Å is due entirely to electron impact H_2 emission. Figure 3.2 shows the location of the subtracted continuum for each method in TW Hya, and Figure 3.3 shows examples of the measurements for three ACS targets. These three methods for measuring the H_2 feature luminosity were used to estimate the errors. Comparing the TW Hya spectra at both resolutions indicates that the feature luminosity decreases by $\sim$2 in the low resolution spectrum because some of the flux is blended into the continuum. This error is small compared to the uncertainty in the continuum location.

Using these procedures, we measured the luminosity of the 1600 Å feature in both the ACS spectra and the STIS spectra smoothed to the resolution of ACS; the feature luminosities are given in Table 3.1. For the WTTS/DD, we find that the H_2 feature is not observable and the values presented in Table 3.1 are upper limits based on the rms fluctuations from 1575 to 1625 Å. We thus find that the H_2 feature shows only in the accreting sources. This is not an age effect; our sample includes CTTS and WTTS of similar age at $\sim$10 Myr (left panel of Figure 3.4) but only the accreting sources show the H_2 feature. Moreover, we find a clear correlation of the strength of the feature with L_{acc} in the CTTS (right panel of Figure 3.4), with a Pearson correlation coefficient of 0.68, indicating that the H_2 emission depends on the accretion properties of the source and not on the age. A similar result was found

in Carmona et al. (2007), where the probability of detecting near-IR H_2 lines was greater in sources with higher accretion rates.

3.4 Discussion

Free electrons are required for the process of electron excitation to be effective (§1). Since, in turn, high energy radiation fields are necessary to produce fast electrons, the absence of H_2 emission in the WTTS/DD could in principle be due to a low level of X-ray or EUV emission in these objects relative to the CTTS. However, Telleschi et al. (2007) found that there is little difference between the X-ray luminosities of CTTS and WTTS in their X-ray survey of pre-main sequence objects in Taurus. Even though there is a soft X-ray excess created in the accretion shock region of CTTS (Günther et al. 2007, and references therein), it does not significantly increase the X-ray production in most young stars (Telleschi et al., 2007). Similarly, Kastner et al. (1997) showed that CTTS and WTTS in the 10 Myr TW Hya Association have similar X-ray luminosities. Moreover, the X-ray luminosity does not decrease significantly over the first 100 Myr of low mass stars (Briceno et al., 1997; Kastner et al., 1997), so the CTTS and WTTS/DD in our sample should have comparable X-ray luminosities.

The EUV radiation field, including emission from approximately 100 to 1000 Å, is also responsible for the ionization of heavy atoms, contributing to the population of free electrons available to excite an H_2 molecule. The EUV is difficult to investigate because the radiation is extremely extincted by interstellar hydrogen. Alexander et al. (2005) find that the EUV flux level does not change in the first ∼10 Myr, from studies of the ratio He II 1640/CIV 1550 Å. If we assume that the FUV level is an indicator of the strength of the EUV emission, we come to similar conclusions. Figure 3.3 shows one CTTS and one DD that have the same FUV luminosity, so one would expect a strong enough EUV radiation field in both sources to create the free electrons needed to excite H_2 if it were present. However, the excess emission at 1600 Å is clearly seen in the CTTS (FP Tau) and absent in the DD (MML 36).

Since the high energy radiation fields in both CTTS and WTTS/DD are compara-

ble in strength, the most likely explanation for the lack of H_2 emission in WTTS/DD is that there is essentially no gas in their inner disks. Given the close relationship between the H_2 feature strength and L_{acc} shown in Figure 3.4, our results suggest that H_2 gas dissipates in timescales consistent with the cessation of accretion; when the gas is dissipated in the inner disk, there is no material left to accrete.

We use the observations to make a rough estimate of the column density of H_2 being collisionally excited. We assume that the H_2 is emitted in an optically thin region of the disk with area A and thickness z. The emitted luminosity per unit volume is $\mathcal{E}_\lambda = h\nu\sigma_\lambda v\chi_e n_{H_2}^2$, where $h\nu$ is the energy of the emitted photon, σ_λ the H_2 cross section, v the impacting electron velocity, n_e the electron number density, χ_e the electron fraction, and n_{H_2} the number density of H_2. The expected flux at 1600 Å due to electron impact excitation is then

$$F_{1600} = \frac{h\nu\sigma_{1600} v\chi_e \Sigma^2 R^2}{16 m_H z d^2}. \tag{3.1}$$

where Σ is the surface density of H_2 excited by electron impacts, m_H the mass of hydrogen, R the radius of the emitting region, and d is the distance. We find that the electron excitation model that provides the best fit to the 1600 Å feature of our sample of CTTS with STIS spectra is characterized by a temperature $T \sim 5000$ K and an electron energy of ∼12 eV. For these values, $\sigma_{1600} = 10^{-20}\mathrm{cm}^2\mathrm{Å}^{-1}$ (Abgrall et al., 1997). According to the thermal models of (Meijerink et al., 2008, M08), gas reaches $T \sim 5000$K within 1 AU of the star, which is consistent with the upper limit to the extension of the H_2 emitting region set by the STIS resolution in the case of TW Hya (Herczeg et al., 2002). We further assume that most electrons are capable of exciting H_2 and adopt $\chi_e = 5 \times 10^{-3}$, as well as R ∼1 AU and z ∼0.1 AU (M08). Using these numbers, and assuming that all the flux at 1600 Å is due to electron impact excitation, we get the estimates of Σ in Table 3.1, which for CTTS are consistent with predicted formation in the uppermost levels of the disk (M08).

A similar estimate can be made for the column density of electron excited H_2 in the WTTS/DD in our sample, which have some dust remaining at larger radii but no

detected IR H_2 lines (Carpenter et al., 2009, 2008; Hillenbrand et al., 2008; Verrier & Evans, 2008; Chen et al., 2005; Low et al., 2005). These estimates are given in Table 3.1. We used the flux of MML 36, which is the WTTS/DD with the highest flux at 1600 Å in our sample, to estimate the mass of H_2 inside $\sim$1 AU; we found that there must be less than 10^{-7} earth masses, 10^{-7}% of the MMSN, lower than the 0.01% of the MMSN estimated by Pascucci et al. (2006). This has important implications for the formation of terrestrial planets, especially if gas is needed to circularize orbits (Agnor & Ward, 2002). Kominami & Ida (2002) theorize that at least 0.01% of the MMSN must be present during the formation of proto-planets, which form around 10 Myr according to simulations by Kenyon & Bromley (2006). Our column density estimates indicate that the amount of H_2 gas present in WTTS/DD with ages of 10-100 Myr is too small to circularize the orbits of the terrestrial planets being formed at that time. Our results support the conclusion by Pascucci et al. (2006) that there must be an additional source responsible for damping eccentricities, one possibility being dynamical friction with remaining planetesimals. Another possibility is that other species of gas exist after the H_2 has been depleted, for example, C and O have been detected around the 10 Myr debris disk β Pic (Fernández et al., 2006; Roberge et al., 2006). C and O do not feel strong radiation pressure due to the low FUV flux in WTTS and therefore may remain after the H_2 has been depleted (Roberge et al., 2006).

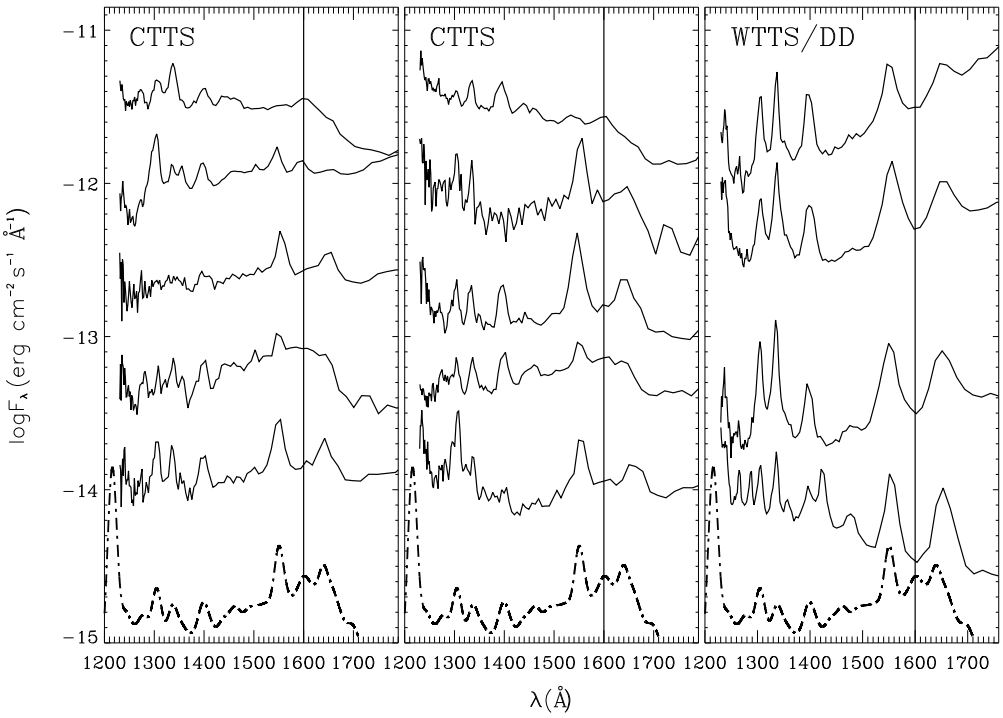

Figure 3.1. Sample of ACS CTTS spectra. Spectra have been corrected for reddening using the values of A_V listed in Table 3.1. Spectra have been scaled vertically for clarity. The bottom spectrum (dash-dotted line) in each panel is the STIS TW Hya spectrum smoothed to the resolution of the ACS spectra for comparison and offset by -1.2. The vertical line at 1600 Å marks the center of the feature used to identify the H_2. Left panel, from top to bottom including the offset in parenthesis: DP Tau (+2.7), DR Tau (+1.5), FM Tau (+0.5), FP Tau (+2.2) and GK Tau (+0.3). Middle panel; from top to bottom: HN Tau A (+1.9), HN Tau B (+3.0), IP Tau (+1.5), UZ Tau A (+1.2) and UZ Tau B (+0.45). The right panel shows ACS spectra of WTTS/DD; from top to bottom: HD 12039 (+3.4), HD 202917 (+2.5), HD 61005 (+2.0), HD 92945 (+1.7) and HD 98800 (+0.8).

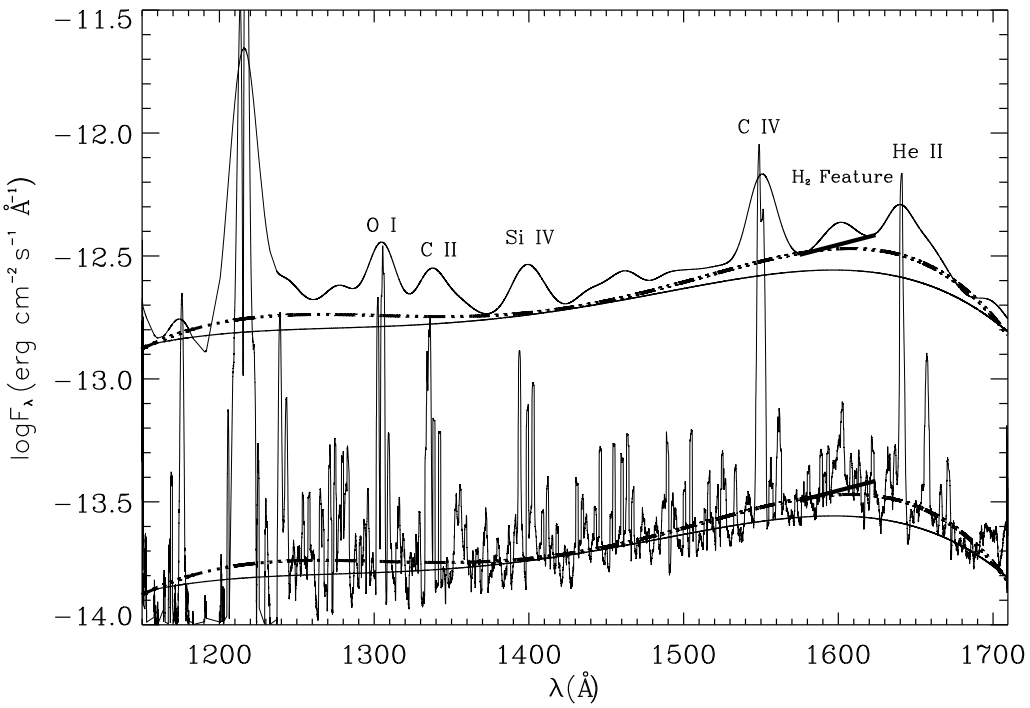

Figure 3.2. Observed and convolved spectra for TW Hya. The bottom spectrum is the high resolution STIS FUV spectrum. The top spectrum is the TW Hya spectrum convolved to the ACS spectral resolution and offset by +1.0. The solid and dashed lines on the smoothed spectrum show the three subtracted continua. These three continua are also shown plotted on the high resolution spectrum and indicate that the lowest continuum may provide the best measure of the luminosity. The strong emission lines are labeled along with the H_2 feature.

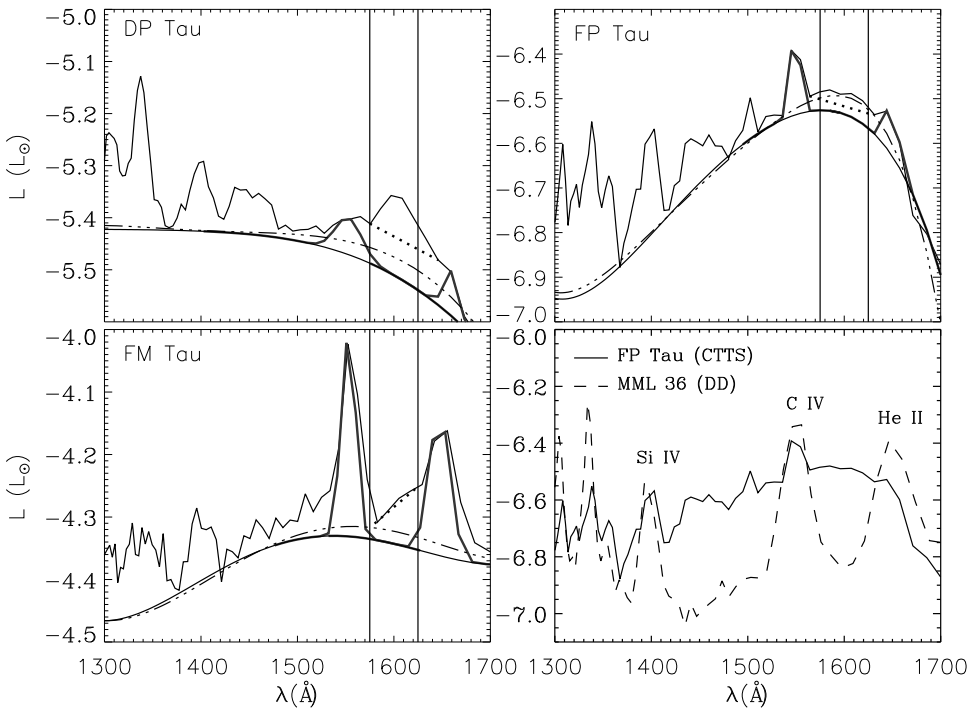

Figure 3.3. H_2 measurements for ACS sources. The first three panels show ACS sources and the location of the subtracted continua, shown as the solid, dashed and dot-dashed lines. Also plotted are the He II and C IV emission lines as the thick solid line. The final panel compares accreting and non-accreting sources with the same luminosity. An excess in FP Tau is observed at 1600 Å, which is due to electron impact H_2 emission, and also between the S IV and C IV lines, which is likely due to blended electron impact and Lyα fluorescent lines.

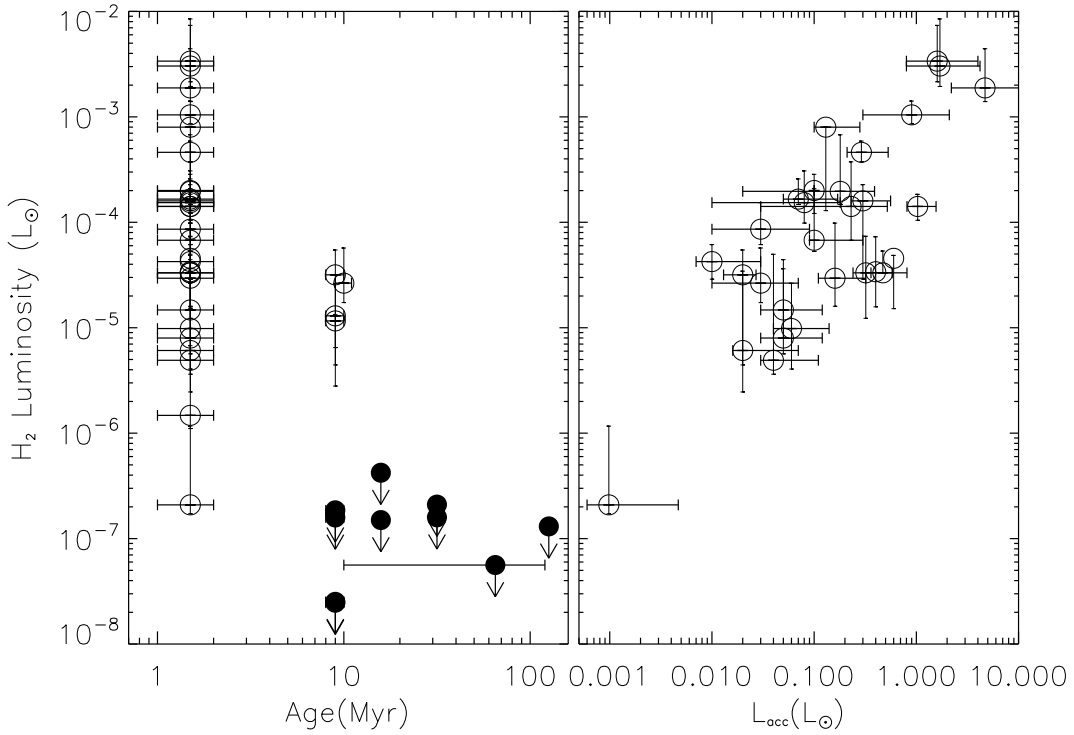

Figure 3.4. Luminosity of H_2 vs age and accretion luminosity. Left: Luminosity of the H_2 vs. age. Filled circles represent WTTS and open circles represent CTTS. For the WTTS we show only an upper limit on the luminosity of the H_2. Right: H_2 luminosity vs. L_{acc}. The H_2 luminosity is observed to increase with L_{acc}. Errors on L_{acc} are calculated using the scatter in the correlation with L_U presented in Gullbring et al. (1998).

Table 3.1: CTTS and WTTS/ Debris Disks Observed with ACS/SBC

Object	SpT	L ($L_\odot$)	A_V (mag)	Age (Myr)	L_{acc} ($L_\odot$	H_2 Feature $10^{-5}L_\odot$)	Σ (10^{-6} g cm^{-2})
ACS CTTS							
AA Tau	M0	1.1	1.4	1	$0.13\pm^{.15}_{.03}$	$79.9\pm^{0}_{67}$	> 49.3
CI Tau	K6	1.3	2.1	1	$0.47\pm^{.34}_{.11}$	$3.3\pm^{2.0}_{0}$	> 9.9
DE Tau	M1	1.2	1.1	1	$0.16\pm^{.16}_{.05}$	$2.9\pm^{6.9}_{1.4}$	> 36.3
DL Tau	K7	1.0	1.6	1	$0.32\pm^{.26}_{.08}$	$3.3\pm^{4.1}_{2.1}$	> 22.5
DN Tau	M0	1.2	0.8	1	$0.04\pm^{.07}_{.01}$	$0.49\pm^{4.5}_{.13}$	> 18.4
DO Tau	M0	1.4	2.4	1	$0.29\pm^{.24}_{.08}$	$46.1\pm^{13}_{8.6}$	> 84.6
DP Tau	M0	0.2	0.5	1	$0.01\pm^{.02}_{.003}$	$4.2\pm^{1.9}_{1.4}$	> 17.6
DR Tau	K7	1.7	1.0	1	$1.03\pm^{.53}_{.22}$	$14.1\pm^{4.3}_{3.7}$	> 43.2
FM Tau	M0	0.5	1.9	1	$0.30\pm^{.26}_{.07}$	$16.0\pm^{6.8}_{13}$	> 61.7
FP Tau	M3	0.4	0.1	1	$0.001\pm^{.004}_{.0004}$	$0.021\pm^{.10}_{.004}$	> 4.9
GK Tau	M0	1.4	1.1	1	$0.06\pm^{.08}_{.02}$	$0.98\pm^{1.7}_{.58}$	> 18.1
HN Tau A*	K5	0.2	1.2	1	$0.07\pm^{.10}_{.02}$	$16.6\pm^{9.2}_{1.8}$	> 38.8
HN Tau B*	M4	0.03	0.9	1	–	$0.15\pm^{.53}_{.04}$	> 5.8
IP Tau	M0	0.7	0.9	1	$0.02\pm^{.05}_{.004}$	$0.61\pm^{2.8}_{0.4}$	> 15.0
UZ Tau A*	M1	0.3	0.5	1	$0.02\pm^{.07}_{.02}$	$0.80\pm^{2.8}_{0}$	> 14.3
UZ Tau B*	M2	0.3	1.0	1	$0.02\pm^{.07}_{.02}$	$1.5\pm^{2.9}_{.91}$	> 8.5
CVSO 206	K6	0.2	0.2	9	–	$1.2\pm^{.17}_{.51}$	> 13.9
CVSO 35	K7	0.7	0.7	9	$0.02\pm^{.01}_{.01}$	$3.2\pm^{2.3}_{2.7}$	> 16.6
CVSO 224†	M3	0.1	0.5	9	–	–	–
OB1a 1630	M2	1.0	0.0	9	–	$1.3\pm^{1.3}_{1.0}$	> 13.3
STIS CTTS							
BP Tau	K7	1.3	1.0	1	$0.23\pm^{.29}_{.20}$	$14.1\pm^{23}_{7.4}$	>41.6
DM Tau	M1	0.3	0.6	1	$0.08\pm^{.10}_{.07}$	$15.4\pm^{15}_{5.5}$	> 39.5
GM Aur	K3	1.2	1.1	1	$0.18\pm^{.21}_{.16}$	$19.7\pm^{48}_{4.9}$	> 48.7
LkCa 15	K5	1.0	1.0	1	$0.03\pm^{.06}_{.02}$	$8.6\pm^{6.8}_{2.5}$	> 26.4
RY Tau	G1	9.6	2.2	1	$1.6\pm^{2.4}_{.80}$	$338.0\pm^{400}_{120}$	> 148.4
SU Aur	G1	7.8	0.9	1	$0.10\pm^{.20}_{.01}$	$6.8\pm^{14}_{1.5}$	> 30.0
T Tau	G6	7.8	1.8	1	$0.90\pm^{1.2}_{.60}$	$104.5\pm^{37}_{18}$	> 103.9
CO Ori	G0	22.3	2.0	1	$1.7\pm^{2.5}_{.90}$	$303.5\pm^{550}_{110}$	> 149.0

Continued on Next Page...

Table 3.1 – Continued

Object	SpT	L	A_V	Age	L_{acc}	H_2 Feature	Σ
EZ Ori	G3	5.9	0.6	1	$0.10\pm^{0}_{0}$	$20.0\pm^{8.5}_{7.9}$	> 41.1
GW Ori	G0	61.8	1.3	1	$4.7\pm^{6.9}_{2.5}$	$188.2\pm^{250}_{49}$	> 178.8
P2441	F9	11.5	0.4	1	$0.4\pm^{.60}_{.20}$	$3.4\pm^{3.9}_{1.8}$	> 29.0
V1044 Ori	G2	6.7	0.4	1	$0.6\pm^{.90}_{.30}$	$4.6\pm^{30}_{3.0}$	> 37.6
TW Hya	K7	0.3	0	10	$0.03\pm^{.04}_{.02}$	$2.6\pm^{3.1}_{.92}$	> 43.9
ACS WTTS							
HD 12039	G4	–	0	31.6	0	$<.021$	< 2.2
HD 202917	G5	0.7	0	31.6	0	$<.016$	< 2.8
HD 61005	G8	0.6	0	125.9	0	$<.013$	< 1.3
HD 92945	K2	–	0	20 - 150	0	$<.006$	< 0.93
HD 98800	K5	0.6	0	10.0	0	$<.019$	< 0.84
MML 28	K2	–	0.1	15.8	0	$<.015$	< 2.4
MML 36	K5	–	0.3	15.8	0	$<.042$	< 3.3
TWA 7	M1	0.31	0	10.0	0	$<.003$	< 1.0
TWA 13A	M1	0.18	0	10.0	0	$<.016$	< 1.5
TWA 13B	M1	0.17	0	10.0	0	$<.002$	< 1.5

* Stellar properties for binaries are from White & Ghez (2001). UZ Tau A and B are themselves binaries; UZ Tau A is a spectroscopic binary and UZ Tau B is a binary system (White & Ghez, 2001) but is unresolved by ACS/SBC.

† CVSO 224 is a CTTS surrounded by a transitional disk (Espaillat et al., 2008) and has a very low $\dot{M}$. The ACS/SBC spectrum of this target is noisy and while we cannot confidently quantify the H_2 emission, we do see the rise in the spectrum at 1600 Å which indicates its presence.

CHAPTER 4

Short Gas Dissipation Timescales: Diskless Stars in Taurus and Chamaeleon I

4.1 Introduction

An early stage of pre main-sequence evolution is characterized by the accretion of gas from the inner disk by magnetospheric accretion. The inner disk is truncated by the stellar magnetic field and infalling gas is channeled onto the star by the field lines creating a shock upon impact with the photosphere (Calvet & Gullbring, 1998). As the source evolves the mass accretion rate decreases, until eventually, accretion ends when the inner disk gas is depleted (Chapter 3; hereafter I09). Accreting young stars with gas rich disks are called classical T Tauri stars (CTTS) and non-accreting T Tauri stars with gas poor disks, weak T Tauri stars (WTTS). Little is known about how the gas is ultimately depleted from the disk, marking the transition from CTTS to WTTS. The amount of gas remaining in the disk may affect the eccentricity and migration of planetary orbits (Kominami & Ida, 2002; Matsuyama et al., 2003) and therefore the gas dissipation timescale is key for models of planet formation and evolution.

Circumstellar disk evolution is primarily traced by dust in the disk, emitting at infrared (IR) wavelengths (Hernández et al., 2008). Attempts at modeling the IR excess have resulted in a possible sequence of disk evolutionary stages. Beginning with a full disk of small dust particles distributed throughout the vertical layers, the dust coagulates and settles towards the midplane (Weidenschilling, 1997; Dullemond & Dominik, 2004). There, a planet may form, and if massive enough, open a gap in the disk (Zhu et al., 2011), observed as a deficit in IR fluxes. A disk gap may

also form when the mass loss rate due to photoevaporation of disk material by high radiation from the central star exceeds the mass accretion rate (Clarke et al., 2001). After the gap is formed the inner disk is drained onto the star by viscous evolution and/or is removed from the system through continued photoevaporation, creating an inner disk hole.

Circumstellar gas evolution has proved harder to probe than the dust, due to the difficulty of detecting spectroscopic gas signatures. Recently, observations of molecular gas in the disks of low mass T Tauri stars have increased, including IR detections of H_2O, OH, HCN and C_2H_2 with the *Spitzer* Infrared Spectrograph (IRS) (Carr & Najita 2011, and references therein), *Herschel* (e.g. Mathews et al. 2010) and *Hubble Space Telescope* (HST) FUV observations of H_2 (France et al., 2011; Herczeg et al., 2002; Calvet et al., 2004; Yang et al., 2012, see also Chapter 5). In a study of 43 young stars, I09 used low resolution FUV spectra from the Advanced Camera for Surveys Solar Blind Channel (ACS/SBC) PR130L prism to study gas in disks surrounding accreting and non-accreting sources between 1 Myr and 1 Gyr. I09 located a continuum feature in the low resolution spectra near 1600 Å produced when H_2 is excited by high energy electrons (Bergin et al., 2004) and found it present in accreting sources but absent in non-accreting sources. Since the X-ray emission necessary for producing the high energy electrons is strong during pre-main sequence evolution (Chapter 2), the lack of H_2 emission in the non-accretors indicates that gas is cleared from the inner disk by the time accretion ends. However, I09 only observed non-accreting sources at ages >10 Myr and observations of young WTTS were necessary to confirm that the gas is completely drained, even when accretion stops early on.

We present FUV observations of 1–3 Myr WTTS in the Taurus and Chamaeleon I star forming regions and look for evidence of circumstellar H_2. In Section 4.3 we present results on the presence or lack of H_2 and in Section 4.4 we discuss mechanisms which may be responsible for disk evolution in these sources, as well as the evolution of high energy radiation from the star.

4.2 Sample, Observations and Data Reduction

4.2.1 FUV Observations

We obtained observations centered on 11 young stars using ACS/SBC on *HST* in GO program 12211 (PI: Calvet). Two of the fields contained wide binaries where the spectrum of each component was extracted separately; however, one of the single stars was not detected in the FUV, therefore the total sample consists of 12 sources. Each ACS observation consists of a brief image in the F165LP filter and a longer image obtained with the PR130L prism. Offsets between the target location in the filter and prism image, including the wavelength solution, were obtained from Larsen (2006). The target spectrum was then extracted from a 41-pixel (1.″3) wide extraction window. Background count rates were calculated from offset windows and subtracted from the extracted spectrum. The absolute wavelength solution was then determined by fitting the bright C IV λ1549 Å doublet. Fluxes were calibrated from the sensitivity function obtained from white dwarf standard stars by Bohlin (2007). The spectra cover 1230–1800 Å with a 2-pixel resolution of $\sim$300 at 1230 Å and $\sim$80 at 1600 Å.

4.2.2 Notes on Sample and Individual Sources

The FUV detections include 7 low mass T Tauri stars in Taurus and 5 in Chamaeleon I (Figure 4.1 and Table 4.1). WTTS were chosen based on a lack of evidence for remaining inner disk dust as traced by $K - L < 0.4$ for Taurus sources (Kenyon & Hartmann 1995), or by a Spitzer IRS slope < -2.2 between 2 and 24μm or 3.6 and 24μm for sources in Chamaeleon I (Luhman et al. 2008), and no ongoing accretion, defined as Hα equivalent width (EW) $<$ 10 Å for the spectral types of this sample (Kenyon & Hartmann 1995; Luhman 2004). Very low accretion may not register on the Hα line profile in low resolution spectra (Chapter 5); therefore, small quantities of gas could remain in the inner disk.

We detect both components of LkCa 3, a binary with separation of 69 AU (Kraus et al., 2011). We use a spectral type of M1 and assume equal contribution to the unresolved luminosity from each (Kenyon & Hartmann, 1995). For V827 Tau, the lines are too broad, indicating a binary aligned along the dispersion direction. Kraus

et al. (2011) found that V827 Tau is a close binary with mass ratio of ∼0.6 and separation of ∼90 mas (13.5 AU). With the close separation we do not separate the two components. CHXR 68 is a triple system with A and B components separated by 4.″4 and the A component itself a binary with a separation of 0.″1 and mass ratio of 0.6 (Nguyen et al., 2012). We extract A and B individually and identify the two components of the A binary with a separation of 60 mas, but again due to the close separation, the prism spectrum of CHXR 68A is a combination of the two sources. J1-4827 was not detected in the FUV.

4.3 Results

We used a continuum feature at 1600 Å, which is formed primarily by the photodissociation of H_2, as a gauge of the strength of H_2 emission (Bergin et al., 2004). We first de-reddened the spectra using published A_V or A_J magnitudes (Kenyon & Hartmann, 1995; Luhman, 2004) and the Whittet et al. (2004) extinction law. The FUV continuum[1] has contributions from several sources in CTTS, including the chromosphere and accretion shock, in addition to the continuum produced by H_2 dissociation (Chapter 2,5). To approximate the FUV continuum at the PR130L resolution, we used the median FUV spectrum of the WTTS and debris disks (DD) in I09. I09 showed that no H_2 emission was present in the spectra of these sources and there is no ongoing accretion, leaving only the chromospheric contribution. Figure 4.2 compares the median of the I09 WTTS/DD sample to the median of the Taurus and Chamaeleon I WTTS samples. After subtracting the I09 WTTS/DD spectrum, scaled to the target spectra between 1400 and 1500 Å, the flux between 1575 and 1625 Å was integrated and represents the flux of the H_2 feature.

Figure 4.3 shows the luminosities of the H_2 feature in our sample combined with results from I09. We also include new observations of accretors in Chamaeleon I (Chapter 2). Many of the 1–3 Myr WTTS have H_2 feature luminosities within 3σ of the luminosities of the I09 older population which were shown to be cleared of gas in

[1]Due to the low resolution of the ACS/SBC prism, the observed continuum includes unresolved line emission blended with the intrinsic continuum from the source.

the inner disk. The H_2 feature luminosities of the WTTS sample are lower than all but two of the Taurus accretors. For V827 Tau, the luminosity is high ($> 10^{-6}$ $L_\odot$) because of contributions from wide C IV and He II emission lines produced by the binary observed along the dispersion axis. The CTTS HN Tau B has an H_2 luminosity comparable to our WTTS sample; it is a low mass companions with spectral type M4 and unknown accretion properties (Kraus et al., 2011). Given the large error on the low resolution spectra and the similarity in H_2 feature luminosities with the I09 sample, these results are consistent with the 1–3 Myr sample of WTTS being cleared of inner disk gas.

4.4 Discussion

4.4.1 Disk Depletion on Short Timescales

As shown in Figure 4.3, circumstellar gas is depleted in short timescales for some sources, while others retain a gas disk, even at 10 Myr. The diskless sources at 1–3 Myr are interesting because they have lost their disks in timescales much shorter than the typical disk lifetime, 5–10 Myr (Hernández et al., 2008; Fedele et al., 2010). The reason no disks remain for these sources may be due to the initial conditions, e.g. the initial disk mass or angular momentum of the parent cloud (Shu et al., 1987), or may stem from the physical processes which are responsible for dispersing disk material. Close binaries (< 40 AU) may be incapable of retaining a disk; however only three of our sources are close binaries, V826 Tau, V827 Tau and CHXR 68A (Kraus et al., 2012; Nguyen et al., 2012). Other possible mechanisms for disk dispersal include viscous evolution and accretion of gas, planet formation and photoevaporation.

In addition to gas, the dust is gone, based on photospheric IR fluxes observed in IRS spectra indicating a lack of inner disk dust (Luhman et al., 2008; Wahhaj et al., 2010). Andrews & Williams (2005) observed five of the Taurus sources in the sub-mm, tracing the outer disk, and constrained the disk mass to <0.0004 $M_\odot$ (< 2 M_{Jup}). They also compared sub-mm and IR data for their sample and found that most sources lacked excesses in both, indicating that inner and outer disks are

dispersed within 10^5 years of each other. Therefore, both the gas and dust in both the inner and outer disks of our sample were likely depleted quickly. While planets alter the disk structure by forming a gap at their orbital radius, it is unlikely that they will completely disperse both the inner and outer disks (Zhu et al., 2011).

Blue-shifted forbidden line emission at velocities around 10 km s^{-1} is interpreted as evidence that gas is undergoing photoevaporation (Pascucci et al., 2011). Theories of photoevaporation differ regarding the type of high energy emission responsible for the mass loss and the rates at which the material is dispersed, yet all models eventually produce a gap in the disk. Initial models of photoevaporation by EUV emission predicted low mass loss rates of $\sim 10^{-10}$ $M_\odot\,yr^{-1}$ (Font et al., 2004; Alexander et al., 2006). Alexander et al. (2006) showed that once the initial gap is formed, both the inner and outer disks disappear quickly, in $\sim 0.1 - 0.2$ Myr, consistent with the observations of Andrews & Williams (2005). After the gap is formed, the inner and outer disk are influenced by continued accretion and photoevaporation, respectively, at rates of 10^{-10} $M_\odot\,yr^{-1}$. At these low rates, the disk mass at the time of gap opening must be less than 2×10^{-5} $M_\odot$ in order for the disk to be depleted in 10^5 years. Given the early age of the sources in our sample, there is little time for the disk to be depleted down to the low masses needed for EUV photoevaporation to disperse the disk.

A larger disk mass is possible if the mass loss rate is higher than that predicted by EUV photoevaporation, and recent models of photoevaporation which include X-ray and FUV emission achieve mass loss rates up to 10^{-8} $M_\odot\,yr^{-1}$ (Gorti et al., 2009; Owen et al., 2012b). In Owen et al. (2012b), the mass loss rate scales with the X-ray luminosity; for the X-ray luminosities of our WTTS sample (see §4.2), the predicted mass loss rate would be $\sim 10^{-8}$ $M_\odot\,yr^{-1}$. Therefore both the inner and outer disk would contain $< 10^{-3}$ $M_\odot\,yr^{-1}$ to be completely removed in $< 10^5$ years, close to the range of predicted disk masses. However, objects with very low accretion rates yet with full disks cannot be undergoing photoevaporation at such high rates, whereas the low mass loss rates predicted by the EUV photoevaporation models are more consistent with observations (see Chapter 5).

Instead, WTTS may form from cloud cores with low initial angular momentum, J. Assuming stars both with and without disks at 1-3 Myr formed from cloud cores with the same mass, the cloud angular momentum determines the mass distribution in the disk. The radius at which the cloud material accretes onto the disk is given by r_c, which depends on the core gas temperature (T), angular velocity (Ω), and mass of the central star (M). Assuming $T = 10$ K and $M = 1\ M_\odot$,

$$r_c \sim 9 \text{ AU} \times \Omega_{-15}^2 \tag{4.1}$$

where Ω_{-15} is in units of 10^{-15} rad s^{-1} (Hartmann, 2009). Assuming uniform rotation, the specific angular momentum is

$$J/M \sim 9.5 \times 10^{19} \text{ cm s}^{-2} \text{ R}_{0.1}^2\ \Omega_{-15} \tag{4.2}$$

where $R_{0.1}$ is the initial radius of the cloud in units of 0.1 pc. If matter falls from a cloud with $R_{0.1}$=0.1 pc at $r_c \leq 1$ AU (which would accrete onto the star in only 30,000–40,000 years), then J/M=19.5 cm^2 s^{-1}. This is a rough approximation of the angular momentum, as the actual collapse of cloud cores is significantly more complicated than assumed here and physical properties of the cloud (for example, the magnetic field strength) may be important (Allen et al., 2003). Up to 20% of cloud cores have low enough angular momenta to form a disk which would accrete quickly, according to the models of Dib et al. (2010) which show that angular momenta inferred from observations are overestimated by assuming a 2D geometry. The observed disk fractions in the youngest clusters are 90–95% (Hernández et al., 2008). Given the distribution of angular momenta predicted by Dib et al. (2010), it is possible that the 5–10% of diskless stars formed from slowly rotating clouds.

4.4.2 Evolution of Chromospheric Emission

Accurate estimates of the high energy emission in young stars are important because one or a combination of these fields may drive photoevaporation. The active chromospheres in young stars produce a UV excess with respect to the photosphere

(Houdebine et al., 1996); however, the total excess is difficult to estimate due to the small number of UV observations of WTTS. Here, we analyze the FUV emission of 23 non-accreting young stars (combining our sample with the WTTS/DD sample in I09) to characterize the evolution of chromospheric emission. WTTS have no emission contributions from accretion or H_2, so the FUV continuum and hot lines are intrinsic to the young star and provide a gauge of the chromospheric emission.

We also include published X-ray observations to probe the evolution of coronal emission (Voges et al., 1999; Feigelson et al., 1993; Güdel et al., 2007). ROSAT and XMM-Newton X-ray count rates were converted to X-ray luminosities in the 0.2-10 keV range using the HEASARC tool WebPimms for comparison to the X-ray luminosities of the I09 WTTS/DD sample. In Figure 4.4, we show the evolution of high energy stellar radiation fields between 1 and 100 Myr [2]. Large X-ray samples of WTTS indicate that the emission saturates around 10 Myr (Preibisch et al., 2005). The X-ray saturation level of our sample, $\log L_X/L_{bol} = -2.9 \pm 0.2$, is within the errors of that found previously, $\log L_X/L_{bol} = -3.3 \pm 0.4$.

The evolution of FUV emission is not as well studied as the X-ray evolution. Ribas et al. (2005) observed that high energy emission, including FUV, decreases for solar type stars $>$ 100 Myr. Findeisen et al. (2011) determined the chromospheric indicator R'_{FUV} in a sample with GALEX data and observed a decrease in chromospheric activity between $10^{7.5}$ and 10^9 years. Evidence suggests that the same physical mechanism is heating both the chromosphere and the corona; Maggio et al. (1987) and more recently Mamajek & Hillenbrand (2008) found that the coronal X-ray luminosity was correlated with indicators of the chromospheric emission (e.g. the Ca II H and K lines) and in Chapter 2, we showed that X-ray and FUV luminosities are correlated for $>$ 10 Myr non-accretors. Given this evidence that the heating of the chromosphere and corona are linked and should therefore saturate on similar timescales, we estimate the FUV saturation for sources $\leq$ 10 Myr (shown in Figure

[2]In Chapter 2, one source appeared to diverge from the fit to the X-ray decline with age. This source, HD 53143, has an uncertain age, between 45 Myr to 6 Gyr (Nakajima et al., 2010; Holmberg et al., 2009). We find that the young age is more consistent with the observed decline in X-ray emission and therefore assume an age of 45 Myr.

4.4.) Total FUV luminosities were integrated between 1230 and 1800 Å (Table 4.1). We find that the FUV luminosity saturates at a level of $\log L_{FUV}/L_{bol} = -4.1 \pm 0.1$. We also see evidence for the beginning of the expected decline in FUV emission for the oldest sources in our sample.

4.4.3 Summary

We presented results from an FUV study of the gas (or lack of gas) in the disks around 1-3 Myr WTTS. Our conclusions are summarized here.

- A new FUV sample of young (1–3 Myr) WTTS in the Taurus and Chamaeleon I star forming regions confirms previous results that H_2 gas in the inner circumstellar disk is completely dissipated by the time accretion onto the star ends. This is true even for the youngest non-accretors.

- Photoevaporation alone cannot explain diskless stars at 1–3 Myr, unless the initial disk mass is very small. However, up to 20% of T Tauri stars may form from clouds with low angular momenta, producing disks with small radii which accrete quickly onto the star.

- If the heating of the corona and chromosphere are related, as observational evidence indicates, we expect the X-ray and FUV emission to saturate at the same age. The saturation of the FUV emission for our sample occurs at $\log L_{FUV}/L_{bol} = -4.1 \pm 0.1$.

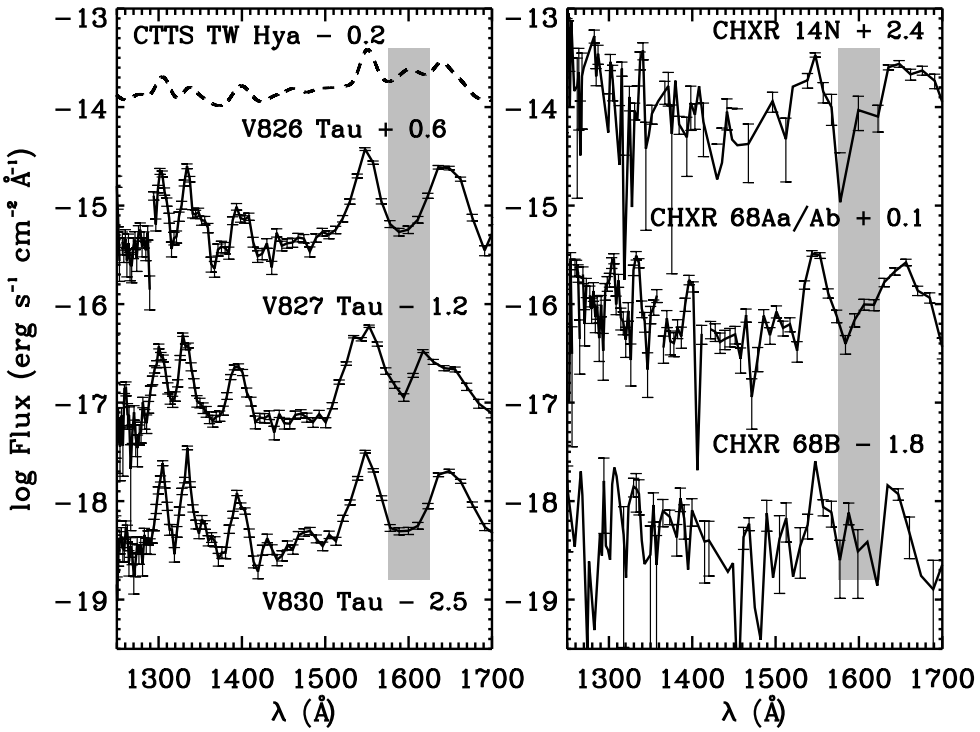

Figure 4.1. ACS/SBC observations. The spectra are offset by the value listed. A Space Telescope Imaging Spectrograph spectrum of the CTTS TW Hya is shown for comparison (Herczeg et al. 2002; dashed line), convolved to the PR130L resolution. The grey shaded area represents the spectral region where we would expect to see H_2 emission, if gas were present in the disk (I09); in TW Hya H_2 emission is observed. For the Chamaeleon I sources, it is unclear if emission near 1600 Å is produced by H_2 or noise in the spectrum as the error bars are large in this region; the signal to noise in the continuum is <3, as opposed to >5 for the Taurus sample.

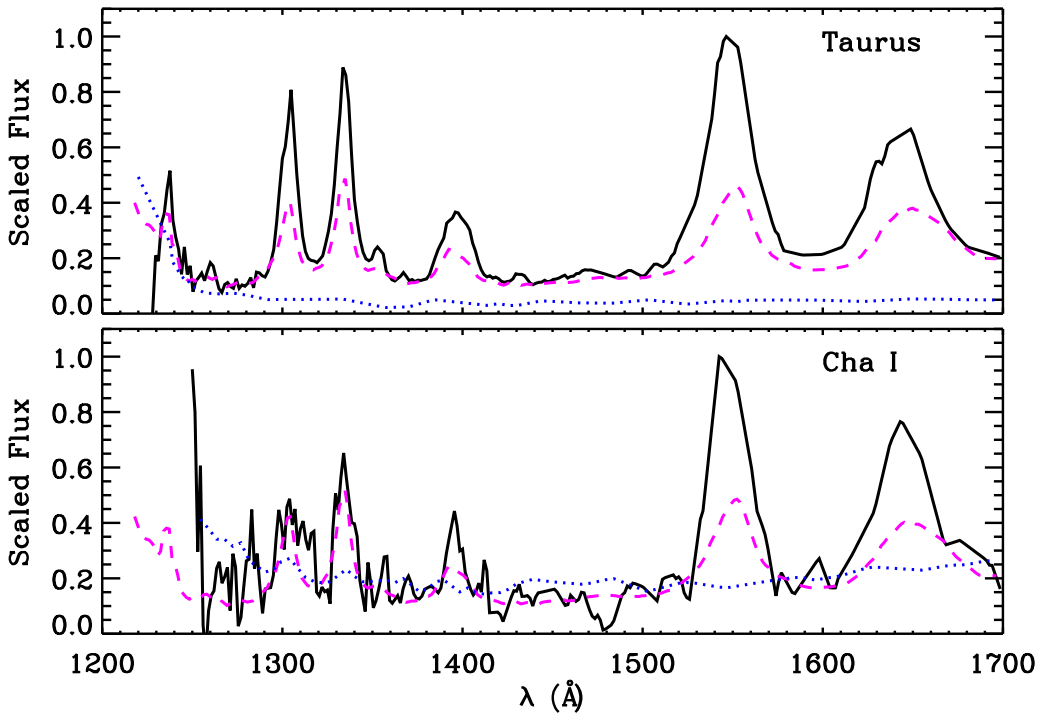

Figure 4.2. Taurus and Chamaeleon I ACS spectra. We compare the median of the Taurus (top panel) and Chamaeleon I (bottom panel) WTTS observations (black line) to the median of the WTTS/DD sample observed in I09 (dashed purple line). We also show the level of the background (dotted blue line). For Chamaeleon I, the background emission is comparable to the source flux at 1600 Å.

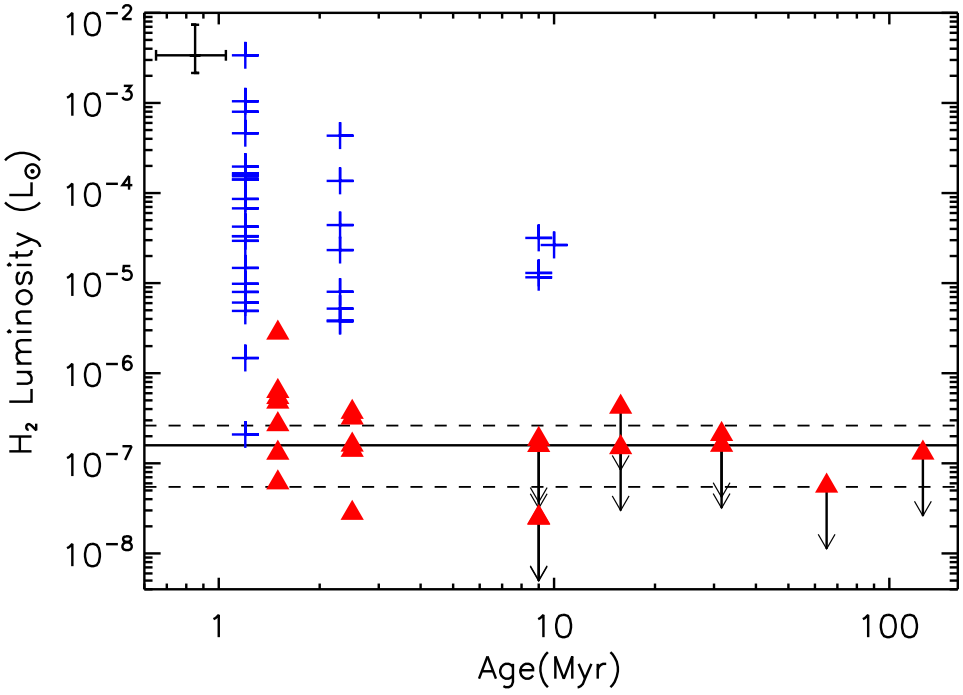

Figure 4.3. H_2 versus age. The luminosity of the H_2 feature for accreting sources is shown as blue crosses and for the non-accretors, red triangles. New WTTS in Taurus and Chamaeleon I are offset from the CTTS in each region by 0.2 Myr for clarity. The solid line represents the median H_2 luminosity for the I09 non-accreting sample and the dashed lines represent 3σ from that median. Typical errors are shown in the upper left corner.

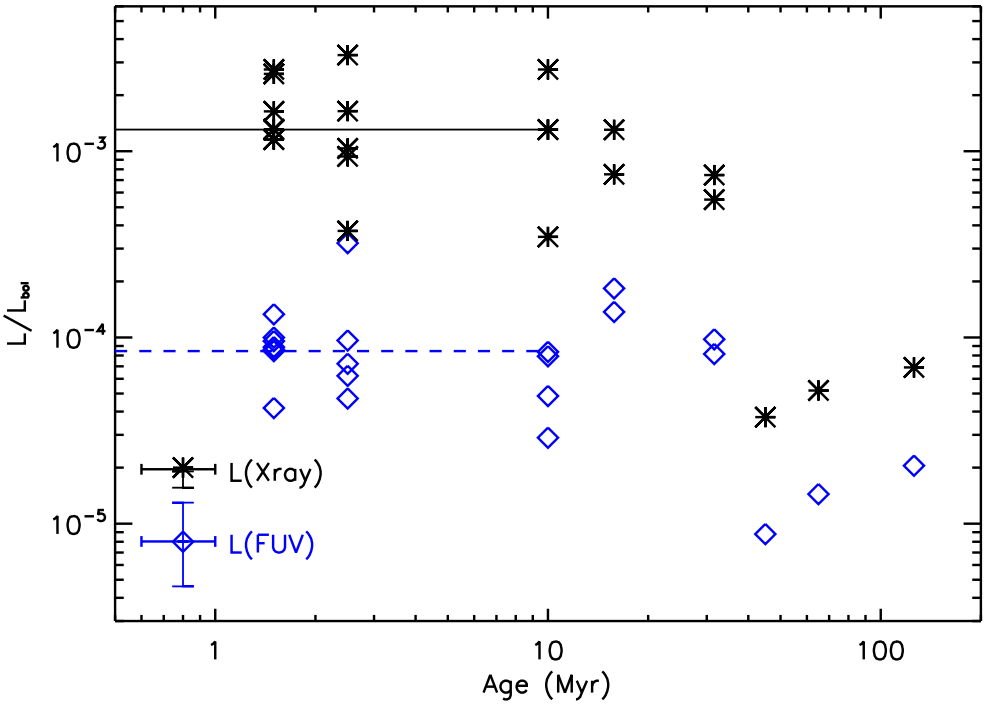

Figure 4.4. X-ray and FUV luminosities normalized by the bolometric luminosity versus age. The median of the X-ray (black asterisks) and FUV (blue diamonds) luminosities for sources at $\leq$10 Myr are indicated with black solid and dashed blue lines, respectively. Typical errors are shown in the lower left corner.

Table 4.1: Young WTTS Observed with ACS/SBC

Object	SpT	Luminosity ($L_\odot$)	A_V	L_{FUV} ($\times 10^{-5}$ $L_\odot$)	Region
J1-4872	K7	0.5	0.0	–	Taurus
LkCa 3E	M1	0.9	0.4	8.0	Taurus
LkCa 3W	M1	0.9	0.4	8.6	Taurus
LkCa14	M0	0.4	0.0	3.4	Taurus
V826 Tau	K7	0.8	0.3	6.8	Taurus
V827 Tau A/B	K7	0.8	0.3	8.0	Taurus
V830 Tau	K7	0.6	0.3	8.0	Taurus
V1075 Tau	K7	0.5	0.0	2.1	Taurus
CHXR 14N	K8	0.4	0.5	2.5	Cha I
CHXR 55	K5	0.7	1.1	22.5	Cha I
CHXR 68 Aa/Ab	K8	0.7	0.4	3.3	Cha I
CHXR 68 B	M2	0.2	0.5	1,9	Cha I
UV Cha	M2	0.4	0.4	2.9	Cha I

Note: Spectral type, luminosity and A_V were taken from Kenyon & Hartmann (1995) and Luhman (2004) for Taurus and Chamaeleon I, respectively.

CHAPTER 5

NUV Excess in Slowly Accreting T Tauri Stars: Limits Imposed by Chromospheric Emission

5.1 Introduction

It is now accepted that classical T Tauri stars (CTTS[1]) are accreting mass from their disks via magnetospheric accretion. In this process, the stellar magnetic field truncates the circumstellar disk and channels gas near the truncation radius onto the stellar surface, where an accretion shock forms. Gas heated by the shock emits energetic photons which, after re-processing in the accretion streams, irradiate the inner disk with ultraviolet (UV) and X-ray photons (Calvet & Gullbring, 1998; Ardila & Johns-Krull, 2009; Günther et al., 2007). This energetic emission plays a key role in driving disk chemistry and may be the most efficient mechanism for dispersing the disk gas (Najita et al., 2010; Pinte et al., 2010; Bethell & Bergin, 2009; Gorti et al., 2009). The rate at which material is accreted is an important input in models of circumstellar disks, affecting the surface density and inner disk heating (D'Alessio et al., 2006), so accurate accretion rates are essential for describing the evolution of both gas and dust. Accretion rates decrease with age (Calvet et al., 2005), so objects with very low accretion rates are particularly interesting for studying the final stages in the evolution of disks.

The spectrum produced by the accretion shock on the stellar surface peaks in the UV, so UV flux excesses over the stellar fluxes are the most direct measure of the accretion luminosity (L_{acc}) from which the mass accretion rate, $\dot{M}$, can be derived

[1]In this chapter we use the terms classical and weak-line T Tauri stars (CTTS and WTTS) to indicate accreting and non-accreting T Tauri stars, respectively, following White & Basri (2003).

(§5.4.2). However, CTTS have active chromospheres which produce UV emission in excess of the main sequence standards (Houdebine et al., 1996; Franchini et al., 1998). The chromospheric contribution to the measured excess is expected to be small when compared to the excess due to accretion in CTTS with typical values of the mass accretion rate, $\dot{M} \sim 10^{-8}\,\mathrm{M}_{\odot}\,\mathrm{yr}^{-1}$ (Gullbring et al., 1998). However, as the disk evolves, the mass accretion rate and accretion luminosity decrease, and so do the accretion-powered UV fluxes. In contrast, indicators of chromospheric activity, e.g. the X-ray luminosity, stay approximately constant in the age range 1 - 10 Myr during which disks evolve significantly (Chapter 2). Therefore, the chromospheric contribution is expected to become more important in determining the total UV flux as the disk evolves and at some point will become the dominant contributor. From this point on, the UV excess is no longer measuring accretion.

In most determinations of accretion luminosity in CTTS to date, the excess fluxes in the UV have been measured using main sequence standards as templates for the intrinsic stellar emission. A better template for the stellar emission of an accreting T Tauri star is a non-accreting T Tauri star (or WTTS), which is expected to have a comparable level of chromospheric activity as a CTTS. However, UV observations of WTTS with enough sensitivity do not exist (Valenti et al., 2003), so it has not been possible to determine typical levels of chromospheric emission, which in turn are important to set up realistic limits to the accretion luminosities that can be determined from UV observations. In this chapter we address these issues by comparing the UV fluxes of a non-accreting WTTS, RECX-1, with those of a very low accretor, RECX-11, and find that the NUV fluxes are dominated by chromospheric emission; this allows us to place limits on the lowest accretion luminosity detectable in the UV.

Even for chromospheric-dominated UV fluxes, alternative indicators may be used to identify whether a young star is accreting. A commonly used accretion indicator is the Hα line profile. Hα is observed in emission in all T Tauri stars but a large velocity width or line asymmetry indicates accretion, whereas a narrow symmetric line profile is characteristic of a non-accreting star (Muzerolle et al., 2001; Lima et al., 2010; White & Basri, 2003). In addition, redshifted absorption components superimposed

on the emission line profiles are direct indication of infalling material and can be explained in terms of magnetospheric accretion (Muzerolle et al., 1998a, 2001). The He I line at 10830 Å can also be used to diagnose accretion properties in T Tauri stars. In CTTS this line shows deep blueshifted and redshifted absorption components in its profile, which have been interpreted as formed in outflows and accretion streams (Edwards et al., 2006; Fischer et al., 2008). Other indicators of accretion used in the literature are the forbidden lines of [OI] 6300 and 6363 Å, which are present only in accreting stars (Hartigan et al., 1995), and the Ca II triplet lines, whose luminosities correlate with accretion luminosity (Calvet et al., 2004). In this chapter we analyze these accretion indicators in high resolution spectra of RECX-11 and RECX-1. We find conclusive evidence for accretion in RECX-11 and not in RECX-1 in our high resolution observations of Hα and He I λ10830, but not in other lines. Our analysis allows us to assess which accretion indicators are appropriate for detecting accretion at very low levels.

The indicators discussed above are directly tracing material in the accretion shock or flows, but another indirect method of determining whether a source is accreting or not involves gas in the inner circumstellar disk. While in the past circumstellar gas was difficult to observe, new observations have made gas detections possible (Bary et al., 2008; Bitner et al., 2008; Carr & Najita, 2008; Pascucci et al., 2009). Of particular interest are observations of hot gas very close to the star, near the magnetospheric truncation radius. FUV observations have shown that CO and H_2 at temperatures near 2500 K are present in the disk (France et al., 2011, 2010; Herczeg et al., 2004, 2002). In Chapter 3 we analyzed a sample of FUV spectra of T Tauri stars and found that H_2 was present in the inner 1 AU of all accreting sources but not in non-accreting sources. FUV gas detections therefore indicate more than the presence of gas, but actually show whether a source is still accreting or not. These results were based on ACS low resolution observations; the COS observations presented in this chapter allow us to confirm this finding using spectrally resolved H_2 lines.

This chapter is organized as follows. In §5.2 we present the UV, optical and IR data discussed in this chapter. In §5.3 we discuss which commonly used accretion

indicators are valid at low levels of accretion and which are unreliable. In §5.4 we estimate limits for the minimum $\dot{M}$ that can be determined from the UV. Finally, in §5.5 we discuss the limitations of current accretion rate determinations in view of our results, as well as the implications for disk evolution models.

5.2 Observations

5.2.1 The Targets

Our targets are the young stars RECX-1 and RECX-11 in the η Chamaeleontis group, the nearest open cluster at only 97 pc with an age of 5-9 Myr (Mamajek et al., 1999, 2000; Luhman & Steeghs, 2004). With $A_V \sim 0$, this region has little extinction (Luhman & Steeghs, 2004), making it ideal for UV observations as corrections for reddening may introduce large uncertainties. The sources have similar spectral types, and were classified as K4 by Mamajek et al. (1999) and K5-K6 by Luhman & Steeghs (2004). Sources in this region have also been well characterized in the infrared with broad band $J-L$ photometry (Lyo et al., 2004), *Spitzer* IRAC and MIPS photometry and Infrared Spectrograph (IRS) spectroscopy (Sicilia-Aguilar et al., 2009). The properties of each source are summarized in Table 5.1.

5.2.2 HST Observations

Observations of RECX-1 and RECX-11 were obtained between 2009 December and 2010 January with COS and STIS on HST in GO Program 11616 (PI: Herczeg). STIS NUV observations used the MAMA detector and the G230L grating providing spectral coverage from 1570 to 3180 Å with R$\sim$500-1000. Optical observations were completed during the same orbit as the NUV using the G430L grating which covers 2900-5700 Å with R$\sim$530–1040, resulting in almost simultaneous NUV to optical coverage with STIS.

The low-resolution STIS spectra were calibrated with custom written IDL routines following the procedures described in the STIS data handbook. The wavelengths were calibrated from the location of identified emission lines within the spectrum, and fluxes were calibrated from spectra of WD 1337+705 in the NUV and HIP 45880

in the optical. The flux calibration also includes a wavelength-dependent aperture correction.

COS observations of RECX-11 were presented in France et al. (2011), and we discuss them here together with observations for RECX-1. The COS FUV observations were taken with the G160M and G130M gratings and were completed within 3–4 hours of the STIS observations. The combination of the two gratings provides FUV coverage from 1150 – 1775 Å with R∼16,000 – 18,000. The log of the observations is given in Table 5.2.

The COS spectra were processed by the standard CALCOS calibration pipeline. The individual spectral segments, after obtaining different wavelength settings to minimize instrumental fixed pattern effects and to provide full wavelength sampling, were combined using the IDL coaddition procedure described by Danforth et al. (2010). This procedure coaligns the individual exposures and performs an exposure-weighted interpolation onto a common wavelength grid.

In our COS NUV acquisition image, we resolved RECX-1 into a binary with a separation of $0\farcs141$ and a position angle of 21° (taking into account the fact that MIRRORB creates spurious images), indicating some relative motion between the April 2004 H-band images of Brandeker et al. (2006) and our January 2010 observations. Brandeker et al. (2006) found that the semi-major axis of the orbit was $0\farcs42$. The two stars are also marginally resolved in our STIS spectra, which were obtained with a slit position angle of -49.6°. Separate spectral extractions for the components were obtained by fitting two Gaussians to the cross-dispersed profile at each wavelength position, subtracting off the emission from one component, and subsequently extracting the counts in the other component. From the blue spectrum, we estimate spectral types of K4 for the S component and K6 for the N component, consistent with the unresolved spectral type of K5–K6 (Luhman & Steeghs, 2004). The near-UV spectra of the two stars are similar, except for a ~ 1.5 times stronger Mg II λ2800 flux from the S component. For our analysis, we use the combined spectra of the N and S components to increase the signal to noise. With both components having spectral types close to RECX-11 and very similar STIS spectra, little error is introduced by

using the combined spectra.

5.2.3 Ground Based Observations

Both sources were observed using MIKE (Magellan Inamori Kyocera Echelle) on the Magellan-Clay telescope at Las Campanas Observatory in Chile (Bernstein et al., 2003) on 11 March 2010, with a coverage of 4800–9000 Å and resolution, R∼35,000. The data were reduced using the Image Reduction and Analysis Facility (IRAF) tasks CCDPROC, APFLATTEN, and DOECSLIT (Tody, 1993).

We also obtained 4 low dispersion spectra of RECX-11, covering the Hα line, between 27 November and 22 December 2009, using the Small and Medium Aperture Research Telescope System SMARTS 1.5m telescope at CTIO. We used the RC spectrograph, which is a long-slit spectrograph with a Loral CCD detector; the slit subtends 5 arcmin on the sky and has a 1.5 arcsec slit width. All observations were made by SMARTS service observers and each night consisted of 3 observations with 5 minute integration time. The three observations are median-filtered to minimize contamination by cosmic rays. The data was reduced with the SMARTS spectroscopic data reduction pipeline[2]. We subtracted the bias and trimmed the overscan and flattened the image using dome flats. The spectra were extracted by fitting a Gaussian plus a linear background at each column. Uncertainties were based on counting statistics, including uncertainties in the fit background level. The wavelength calibration was based on an arc lamp spectrum obtained before each set of images.

Finally, we obtained $R = 100,000$ spectra of the He I λ10830 line from RECX-11 with Phoenix on Gemini South on 12 December 2009 and from both RECX-1 and RECX-11 using CRIRES on VLT-UT1 on 22 May 2011. The observations were obtained in an ABBA nod pattern. The star η Cha, a B8 pre-main sequence star with no detectable photospheric features at 10830 Å, was observed to provide the telluric correction. These spectra were reduced with custom-written routines in IDL. The wavelength solution is accurate to $\sim$ 1 km s^{-1} and was calculated from a linear fit to telluric absorption lines obtained from spectra generated by ATRAN (Lord 1992)

[2]http://www.astro.sunysb.edu/fwalter/SMARTS/smarts_15ms ched.html#RCpipeline

and available online.

5.3 Accretion Analysis

Figure 5.1 shows the STIS NUV spectra of RECX-1 and RECX-11; they are remarkably similar, making it difficult to assess if either is accreting based on a UV excess. Also shown in Figure 5.1 is a STIS spectrum of the inactive K5V star HD 154363 (Martínez-Arnáiz et al., 2010, properties in Table 5.1) taken from the HST/STIS Next Generation Spectral Library (Heap & Lindler, 2007), for comparison. Both η Cha sources have excess NUV emission compared to the main sequence standard (§5.4.1). Despite the similarity of NUV fluxes, analysis of emission line profiles shows that one source, RECX-11, is still accreting material from the disk while the other, RECX-1, is not. In this section we review this evidence. We find that the emission line profiles of RECX-11 show redshifted absorption components indicative of accreting material, and consistent with magnetospheric accretion. As mentioned before, accretion shock emission is then expected from the accreting star, but it must be hidden by intrinsic chromospheric emission present in both the accreting and the non-accreting stars; this points to a very low accretion luminosity and mass accretion rate. In §4 we estimate upper limits for these quantities.

5.3.1 Diagnostics of Low Accretion

–Lines Produced by Accretion and Related Processes

Our spectroscopic observations, from the FUV to the IR, include a number of emission lines that trace phenomena such as accretion and outflows in T Tauri stars. Line widths of several hundred $\mathrm{km\,s^{-1}}$ are used to identify accretors, but the most conspicuous indicators are redshifted and blueshifted absorption components on the emission line profiles.

Accessible in the optical, the Hα emission line is one of the most commonly used accretion tracers. Figure 5.2 shows MIKE Hα line profiles for RECX-11 and RECX-1. The Hα equivalent widths (EW) of RECX-11 and RECX-1 are 4 Å and 1.3 Å, respectively, which would make RECX-1 a WTTS and RECX-11 a borderline

CTTS/WTTS according to the standard criterion for a K5–K6 star (White & Basri, 2003). The Hα profile of RECX-1 in Figure 5.2a agrees with the WTTS classification because it is symmetric and narrow. With a line width at 10% of the peak intensity of only $\sim$130 km s^{-1}, the line shows no indication of the high velocities that are characteristic of magnetospheric accretion. In contrast, the Hα profile of RECX-11 is typical of accreting sources, with a line width at 10% of $\sim$300 km s^{-1} (White & Basri, 2003). The blue emission wing is wide, extending to velocities of several hundred km s^{-1}, implying that material is accreting at nearly free-fall velocities. Inverse P Cygni absorption due to infalling material along the accretion streams is also seen (Lima et al., 2010; Muzerolle et al., 2003; Walter, 1999). The line profile is consistent with model predictions for a high inclination source (Muzerolle et al., 2001; Kurosawa et al., 2006), in agreement with the inclination of $i \sim 68°$, estimated from the values of the projected rotation velocity $v\sin i$ (Jayawardhana et al., 2006) and the rotational period (Lawson et al., 2001). Moreover, Lawson et al. (2004) compared their observed Hα profile of RECX-11 with magnetospheric accretion models and obtained a good fit assuming an inclination of $i \sim 70°$.

In Figure 5.2b, we show our MIKE profile and the four SMARTS low resolution Hα profiles of RECX-11 obtained within a few days before and after the HST observations. The Hα profile is highly variable, as already noted by Lawson et al. (2004) and Jayawardhana et al. (2006). The wide blue emission wing is present in all spectra, but variability is conspicuous in the red wing, sometimes showing narrow transient red-shifted absorption components. This variability points to a complex geometry of the accretion streams very close to the star since red-shifted absorption occurs when material in the accretion columns absorbs hot radiation produced in the accretion shock on the stellar surface (Bouvier et al., 2007; Muzerolle et al., 2001). The complex structure revealed by the line profiles of Hα, which in the case of RECX-11 is conclusive in identifying accretion, would have been missed when only considering the equivalent width of the line.

In Figure 5.3 we show two He I λ10830 profiles for RECX-11 obtained 18 months apart with Phoenix and CRIRES along with a CRIRES spectrum of RECX-1 for

comparison. We also show the RECX-11 line profiles after subtraction of the RECX-1 line profile (with the Phoenix observation at the resolution of CRIRES) which removes any contribution by photospheric absorption lines. The He I λ10830 emission profiles show absorption components similar to those found by Edwards et al. (2006) and Fischer et al. (2008) in a large sample of CTTS, which were interpreted as arising in the wind and in the accretion columns. The earlier Phoenix profile shows a broad red-shifted absorption component extending to ~ 250 km s^{-1} with several deep, narrow red and blue-shifted absorption lines at lower velocities, between -50 and 100 km s^{-1}. The second, CRIRES, profile also shows a complex absorption spectrum with a broad component extending from 200–400 km s^{-1}. It also shows a red-shifted emission wing which was not observed in the Phoenix observation. The broad high velocity absorption feature in the CRIRES spectrum occurs at velocities typical of material infalling along accretion streams. According to magnetospheric accretion models, material falling from $5R_*$ in the disk onto a star with the mass and radius of RECX-11 will reach velocities of ~ 470 km s^{-1}, capable of producing the absorption features at the observed velocities (Calvet & Gullbring, 1998).

Fischer et al. (2008) found that sources with low accretion rates, observed to have low veiling at 1 μm ($R_Y < 0.5$), were more likely to have redshifted absorption in He I than sources with high accretion rates. Fischer et al. (2008) also found that in order to explain the He I λ10830 profiles, absorption over a large range of velocities was necessary. They proposed that in low $\dot{M}$ sources accretion occurs in low density, narrow accretion "streamlets" with small filling factors, covering a large velocity range, although none of their sources had low enough accretion rates to test this scenario. The narrow red-shifted absorption features in the Phoenix spectrum of our very low accretor, RECX-11 (§5.4), may be observational evidence for these multiple, narrow accretion streams. Some of these narrow features, like the one at ~ 100 km s^{-1}, may be related to the feature at comparable velocity in seen in the MIKE Hα profile (Figure 5.2), although no definite conclusion can be stated since the lines were observed at different times. Simultaneous extensive coverage of Hα and He I λ10830 is necessary to understand the complexity of the accretion flows in

RECX-11.

In addition to Hα and He I λ10830, the C IV doublet in the FUV spectrum can be used to separate accretors from non-accretors. The C IV λ1549 line emission has been shown to correlate with the mass accretion rate, indicating that its origin is, at least in part, in the accretion shock and flows (Johns-Krull et al., 2000; Calvet et al., 2004). In Figure 5.4 we compare the C IV line profiles of the accretor, RECX-11, to the non-accretor, RECX-1. The C IV line profile is much wider and stronger in the accreting source than in the WTTS, in which the emission is expected to be chromospheric. The strength and width of C IV in RECX-11 is consistent with the accreting nature of RECX-11 (Ardila et al. in preparation).

In the NUV range, the only significant difference between the spectra of RECX-11 and RECX-1 is in the CII] λ2325 Å line, which is much stronger in RECX-11 (Figure 5.1). This line has been observed in other accreting sources (Gómez de Castro & Ferro-Fontán, 2005; Calvet et al., 2004), and its likely origin is the accretion shock.

–**The** H_2 Lines

The FUV spectrum of RECX-11 contains a wealth of lines due to molecular species, including H_2 (France et al., 2011). Lines from H_2 in the UV are mainly due to two mechanisms. Lyα emission excites H_2, producing a fluorescent spectrum in the UV as the electrons cascade back to the ground electronic state (Herczeg et al., 2002, 2004; Yang et al., 2011). In addition, fast electrons can collisionally excite H_2, resulting in UV lines and continua (Bergin et al., 2004, Chapter 3).

Using emission from collisionally excited H_2 measured in low resolution FUV spectra of a large sample of both accreting and non-accreting young stars, Chapter 3 showed that by the time accretion ends, the inner disks are depleted of gas. Our targets confirm this trend at high resolution. In Figure 5.5 we show the COS FUV spectrum of RECX-11 compared to RECX-1; the wavelengths at which H_2 pumped by Lyα may emit are labeled. H_2 emission lines at 1434.1 and 1445.3 Å may also be pumped by the C III λ1174 Å multiplet (Herczeg et al., 2002). Figure 5.5 shows that the COS FUV spectrum of RECX-11 is rich in lines of molecular gas, similar

to previously observed sources with confirmed accretion (Bergin et al., 2004; Herczeg et al., 2002, 2004; France et al., 2010). In contrast, molecular lines are not apparent in the FUV spectra of the WTTS RECX-1. If present, the flux of the H_2 lines in RECX-1 is <5% of the H_2 flux in RECX-11.

Assuming that the molecular lines are formed in the atmosphere of the disk (Herczeg et al., 2004), we constructed synthetic models for an optically thin line formed between radii R_1 and R_2 in a Keplerian disk. We assumed that the emissivity depended on radius as R^γ and that the intrinsic line profile was a Gaussian with width corresponding to a temperature of 2500 K. The intensity at each radius was convolved with the rotational profile corresponding to the Keplerian velocity of the annulus, and the flux was then calculated by integrating the intensity over the range of radii. Finally, the resultant profile was convolved with the G130M line spread function.

Figure 5.6 compares the predicted profile to a flux-weighted average of H_2 lines, selected from the spectral region (<1330 Å) in which all the lines were observed with the same grating, G130M. The continuum of the predicted profile has been scaled to the observed continuum. The shaded region in Figure 5.6 corresponds to predicted profiles for models with inner radius between $R_1 = 1 - 20\ R_*$ (0.01–0.1 AU), outer radius $R_2 = 50 - 500\ R_*$ (0.3–3.2 AU), and emissivity power law exponent $\gamma = -1.5$. $\chi^2_{red} = 3.1 - 3.6$ for the range of models shown in Figure 5.6. We find that the inner radius is well constrained, within the uncertainties of the observations; small inner radii with high Keplerian velocities are needed to account for the width of the observed wings. The outer radius R_2, on the other hand, is not well constrained, since little emission comes from those regions. The power law of the emissivity is constrained by the width of the line near the peak, and we require it to fall rapidly with radius. This rapid fall-off is likely due to the combination of a number of factors. For instance, the excitation will decrease as the flux of Lyα decreases with distance; similarly, the number of electrons in excited states that can absorb Lyα transitions decreases with radius, as the temperature of the upper disk layers drops (Meijerink et al., 2008). Our modeling indicates that the region of formation of the H_2 lines can be as close to the star as 0.01-0.1 AU, as was also found for the accreting brown

dwarf 2M1207 (France et al., 2010). This indicates that gas likely extends closer to the stellar surface than the inner dust disk, see section 5.2.

5.3.2 Unreliable accretion diagnostics at low $\dot{M}$

Additional tracers of accretion present in our dataset, like [O I] at 6300 and 6363 Å and the Ca II infrared triplet, do not provide conclusive indication of accretion in RECX-11. [O I] emission, which is expected to originate in an outflow, is observed only in sources undergoing accretion (Hartigan et al., 1995). We show in Figure 5.7a the line profiles of [O I] λ6300 of RECX-11 and RECX-1. [O I] λ6300 appears in RECX-11 in excess over the WTTS spectrum of RECX-1, but the detection is $< 3\sigma$, and therefore not reliable. Similarly, the Ca II λ8542 is often used as an indicator of accretion, and even used to measure mass accretion rates (Muzerolle et al., 1998a). However, the profile of this line in RECX-11, shown in Figure 5.7b, is indistinguishable from the same line in RECX-1, indicating that the flux comes mostly from the chromosphere.

The Mg II λ2800 line luminosity also correlates with accretion luminosity in accreting stars (Calvet et al., 2004) and is seen in our STIS spectra (Figure 5.1). The line is observed to have the same strength in the weakly accreting star, the WTTS and the dwarf star, indicating that it is mainly due to chromospheric activity. Moreover, its strength does not increase with the NUV emission level of the chromosphere. This agrees with the results of Cardini & Cassatella (2007), who show that at ages <0.3 Gyr, the Mg II λ2800 fluxes are not observed to change due to saturation effects, and so the line strength does not reflect the level of chromospheric activity.

5.4 Measuring Small Accretion Rates

5.4.1 The Chromosphere

While dwarf or giant stars have been used to estimate the intrinsic stellar emission in CTTS when measuring the UV excess, WTTS are the best templates for accretion analysis because they have similar surface densities and are expected to have comparable levels of chromospheric emission. The presence of a UV excess in non-accreting

pre-main sequence stars and active stars (when compared to inactive dwarf stars) due to enhanced chromospheric activity is well established (Houdebine et al., 1996; Franchini et al., 1998). In fact, recent studies with GALEX have relied on this excess to identify young stars in nearby star forming regions (Rodriguez et al., 2011; Shkolnik et al., 2011; Findeisen & Hillenbrand, 2010). This UV excess due to chromospheric emission affects measurements of the excess emission from which accretion luminosities are derived. Several studies have already taken these effects into account. For instance,Valenti et al. (2003) used the average spectrum of several WTTS to estimate the UV excess in low resolution International Ultraviolet Explorer (IUE) spectra of accreting stars. Similarly, Herczeg & Hillenbrand (2008) used WTTS templates to measure flux excesses and estimate accretion rates in very low mass objects. However, many determinations of accretion luminosities and accretion rates based on UV fluxes have used dwarf standards as templates (Gullbring et al., 2000; Calvet et al., 2004). The omission of the chromospheric fluxes makes these determinations, and calibrations of line luminosities derived from them, uncertain at the low end.

In this work we have presented UV fluxes of RECX-1, which to date, is the only WTTS spectrum with the signal and resolution needed for use as a chromospheric template. We compare the spectrum of the inactive K5 main sequence star (HD 154363) with that of RECX-1, shown in Figure 5.1. The flux between 2000–5000 Å from RECX-1 is 0.05 $L_{\odot}$ brighter than that from HD 154363. If this luminosity difference were due to accretion, we would have estimate that RECX-1 is accreting at $\log \dot{M} > -8.5$ $\mathrm{M_{\odot}\,yr^{-1}}$, which is typical of a CTTS. This is a lower limit because we have not accounted for any excess emission outside of the range of observations. This clearly demonstrates the effect of an active chromosphere on the UV spectrum and shows that inactive main sequence standards should not be used to measure small NUV excesses. It can be argued that the chromospheric level of RECX-1 is not typical of WTTS because it is a binary. However, with a binary separation $>$ 15 AU (Köhler & Petr-Gotzens, 2002; Brandeker et al., 2006) it is unlikely that the stars are interacting. In any event, a survey of NUV spectra of WTTS of different spectral types and luminosities is needed to determine the characteristic range of

chromospheric NUV emission in these stars.

5.4.2 Estimate of the mass accretion rate from NUV emission

With evidence that RECX-11 is accreting, we use shock models to estimate upper limits to the accretion luminosity and mass accretion rate of RECX-11. A full description of the accretion shock models can be found in Calvet & Gullbring (1998); here we review the main characteristics. An accretion shock forms at the stellar surface when material from the disk falls onto the star along magnetic field lines (§5.1). The shock formed at the base of the accretion column slows the material to match the stationary photosphere, converting the kinetic energy into thermal energy, and causing the temperature to increase sharply. The shock emits soft X-rays into the pre-shock and post-shock regions and the photosphere below the shock. The heated gas emits the observed excess continuum emission which is strongest in the UV (Calvet & Gullbring, 1998). The accretion shock model is used to fit the NUV excess emission and account for shock emission outside of the range of observations. The model yields the accretion luminosity, from which the mass accretion rate can be derived with knowledge of the stellar mass and radius, through $L_{acc} = GM\dot{M}/R$. The accretion shock model assumes that all the excess flux in the UV comes from accretion, neglecting any contribution from the outflow. Since the luminosity of the wind is <10% of the accretion luminosity for typical mass loss rates (Cranmer, 2009) this assumption is justified.

We model the spectrum of RECX-11 as the sum of the WTTS RECX-1, used as a proxy for the intrinsic stellar emission, and the accretion shock emission; our fit to the observations is shown in Figure 5.8 and has a $\chi^2_{red} \sim 11.5$. Since the NUV fluxes of RECX-11 are essentially chromospheric, our aim is to determine the amount of shock emission that may be hidden in the spectrum of RECX-11. We find that $\dot{M} \sim 3 \times 10^{-10}$ $M_\odot$ yr^{-1} is the highest value of the mass accretion rate that RECX-11 could have and still not show an excess over the chromospheric emission or veiling in the optical absorption lines.

The upper limit on $\dot{M}$ is consistent with estimates of accretion from the emission

lines shown in Figures 5.2 and 5.4. From the width of the Hα line at 10% of the maximum and the relation between 10% width and $\dot{M}$ of Natta et al. (2004), we find $\dot{M} = 2.3 \times 10^{-10}$ $M_\odot\,yr^{-1}$. Also, from the flux in the C IV λ1549Å line, we find $\dot{M} = 1.6 \times 10^{-10}$ $M_\odot\,yr^{-1}$ from the relation between C IV flux and $\dot{M}$ in Valenti et al. (2003). Lawson et al. (2004) fit their Hα line profile of RECX-11 with a magnetospheric accretion model, finding good agreement for a model with a mass accretion rate of $\dot{M} = 4 \times 10^{-11} M_\odot\,yr^{-1}$, also consistent with our upper limit.

5.5 Discussion

5.5.1 L_{acc} vs L_U

While it is ideal to measure L_{acc} from the peak of the excess emission, in the UV, it is often not possible to obtain these observations. To overcome this difficulty, Gullbring et al. (1998) calibrated the excess luminosity in the U broad band, L_U, in terms of the accretion luminosity, L_{acc}, for a sample of stars for which they had medium resolution spectra from 3200 to 5400 Å. Accretion luminosities were measured for each star in this sample by extracting the excess flux through veiling measurements and using a slab model to account for energy outside the observed bands. The excess luminosity in U was measured by subtracting the flux in the U band of a main sequence standard with the same V magnitude from the observed U band fluxes. This correlation was later reproduced using the accretion shock model described in §5.4.2 (Calvet & Gullbring, 1998). The L_{acc} vs L_U relation is commonly utilized in studies of large populations because it provides a convenient method for finding L_{acc} (Rigliaco et al., 2011; Grosso et al., 2007; Robberto et al., 2004; White & Ghez, 2001; Rebull et al., 2000; Hartmann et al., 1998). However, as discussed above, the calibration was developed using dwarf stars as templates against which the U band excess was measured, and as we have shown, T Tauri stars have active chromospheres which contribute to the U excess.

The UV excess observed in the WTTS RECX-1 significantly decreases the estimated excess from the accretion shock emission in the NUV. Assuming that the

chromospheric emission in RECX-1 is typical for $\sim$ K5 stars, then the intrinsic chromospheric NUV flux would be 0.05 $L_{\odot}$ (§5.4.1.) If this NUV excess were interpreted as an "accretion luminosity", using the Gullbring et al. (1998) relation between L_{acc} and U band excess, the excess luminosity in the U band just due to chromospheric emission would be 0.01 $L_{\odot}$. This suggests that for the $\sim$ K5 spectral range, U band excesses and derived accretion luminosities below these limits should be taken with caution. An extensive survey of the intrinsic chromospheric emission in WTTS covering a wide spectral range is necessary to quantify the expected chromospheric emission in CTTS. A re-calibration of the L_U vs. L_{acc} relation using characteristic chromospheric contributions may extend its range of application to low values of L_{acc} and $\dot{M}$.

5.5.2 RECX-11 and Disk Evolution

RECX-11 is in the η Chamaeleontis group, with an estimated age of 5-9 Myr. This age range is interesting because disk frequency studies indicate that $\sim$ 80% of the original disks have already dissipated by $\sim$ 5 Myr (Hernández et al., 2008). The disk around RECX-11 is then one of the few survivors and a study of its properties can give insight into the mechanisms of disk survival and dissipation.

In the age range of RECX-11, viscous disk evolution would predict a value for the $\dot{M}$ between 10^{-10} $M_{\odot}\,yr^{-1}$ and 10^{-8} $M_{\odot}\,yr^{-1}$, extrapolating for the dispersion observed in other populations (Calvet et al., 2005). The $\dot{M}$ for RECX-11 is below this range, so additional disk dispersal mechanisms like photoevaporation may be at play. According to one type of photoevaporation model, EUV photons would ionize the disk surface; a wind is established outside a radius r_g where the gas escape velocity becomes higher than the sound speed. The predicted mass loss rates for EUV photoevaporation is $\sim 10^{-10}$ $M_{\odot}\,yr^{-1}$ (Alexander & Armitage, 2007). After the mass accretion rate becomes comparable to the mass loss rate, mass does not reach the inner disk, which drains onto the star in timescales comparable to the local viscous time, $\sim 10^5$ years (Clarke et al., 2001). An inner disk hole is thus created, and EUV irradiation of its edge is expected to quickly erode the rest of the disk (Alexander

et al., 2006). For the mass of RECX-11 (Table 5.1), the value of r_g (Clarke et al., 2001) would be $\sim$ 7 AU. With further refinements of the theory, the value of the critical radius can be decreased to $\sim 0.1 - 0.2\ r_g$ (Font et al., 2004; Adams et al., 2004). This implies that if EUV photoevaporation were active with mass loss rates greater than the low accretion rate of RECX-11, a hole of at least 0.7 AU should have developed in the RECX-11 disk.

A second type of photoevaporation model includes the effects of stellar X-ray and FUV emission and predicts higher mass loss rates than the EUV models (Ercolano et al., 2008; Gorti et al., 2009). According to the predictions of the X-ray driven photoevaporation models, the wind mass loss rate scales with the X-ray luminosity. The X-ray luminosity of RECX-11 has been recently measured by XMM Newton to be 3×10^{30} erg s^{-1} (López-Santiago et al., 2010), very similar to the value 1.6×10^{30} erg s^{-1} estimated from ROSAT observations (Mamajek et al., 2000). The disk of RECX-11 must have been subject to this influx of high energy radiation for most of its lifetime, since the X-ray luminosity stays approximately constant in the 1 - 10 Myr age range (Chapter 2). With the observed value of the X-ray luminosity, the mass loss rate predicted by X-ray driven photoevaporation is $\sim 10^{-8}$M$_\odot$ yr^{-1}, and the low value of the accretion rate would imply that the disk was quickly clearing its inner regions, with timescales $\leq 10^5$ yrs (Owen et al., 2012b). So, for the X-ray photoevaporation models, the innermost disk regions should be cleared or in the process of being cleared.

To find evidence of the effects of photoevaporation on the disk of RECX-11, we have constructed the SED shown in Figure 5.9. We plot fluxes at the B, V, R, I_C bands (Lyo et al., 2004; Lawson et al., 2001) and J, H, and K bands from the 2MASS survey (Skrutskie et al., 2006) along with *Spitzer*/IRAC [3.6], [4.5], [5.8], and [8] and MIPS [24] and [70] bands from Sicilia-Aguilar et al. (2009). We also include the *Spitzer* IRS spectrum, observed in the SL1 and LL modes; the spectrum was downloaded from the Spitzer archive and reduced with version S18.7 of the Spitzer Science Center pipeline using the SMART data reduction package (Higdon et al., 2004) following the description in McClure et al. (2010). The SED of a K5 star, scaled at J, is shown for comparison; this SED was constructed with colors taken

from Kenyon & Hartmann (1995). The median SED of Taurus (D'Alessio et al., 1999), also scaled at J, is also shown.

The SED shown in Figure 5.9 of RECX-11 shows excess above the photosphere at all wavelengths > 1.5 μm. Beyond the near infrared, the fluxes are lower than the median SED of Taurus, a proxy for optically thick disks in which dust is present all the way into the dust sublimation radius. The slope of the SED between 13 and 31 μm of $n_{13-31} = -0.8$ is steeper than the median value of -0.4 for Taurus, indicating a significant degree of dust settling in the RECX-11 disk (Furlan et al., 2006, 2009; McClure et al., 2010). In addition, the profiles of the 10 μm and 20 μm silicate features in the IRS spectrum are wider than those found in the ISM (Sicilia-Aguilar et al., 2009) and contain substructure consistent with significant dust evolution, either in the form of grain growth or crystallization (Watson et al., 2009).

Despite the high degree of evolution of dust in the disk, the SED of RECX-11 does not show indications of an inner cleared region. In fact, the location of RECX11 in the K-[8] vs. K-[24] diagram corresponds to that of full disks according to the study of circumstellar disks at various stages of evolution by Ercolano et al. (2011). Moreover, the SED of RECX-11 shows a substantial near-IR excess, comparable to the median SED of Taurus, despite the low fluxes at longer wavelengths. The largest contributor to the near-IR excess in T Tauri star disks is the optically thick "wall" at the dust destruction radius, the sharp transition between the dust and gas disk (D'Alessio et al., 2006; Dullemond & Monnier, 2010). For the parameters of RECX-11, the dust destruction radius is of the order of ~ 0.06 AU, taking the simple expression for the equilibrium temperature, with $T = 1400$ K as the dust sublimation temperature, and $T_{eff} = 4350$K for a K5 star (Dullemond & Monnier, 2010).

The evidence then seems to rule out inner clearing in the disk of RECX-11. First, it is accreting, so mass has to reach the magnetospheric radius, 3-5 stellar radii, $\sim$ 0.03 AU. Substantial H_2 emission is observed, coming from gas regions as close in as 0.01-0.1 AU to the central star, typical of all accretors. Moreover, dust extends inwards to ~ 0.06 AU. These inner radii, where disk material is present, are not consistent with those predicted for photoevaporation models, according to which the

innermost < 0.1 AU of the disk should be clear. It could be argued that the disk of RECX-11 has been caught in the short phase when the inner disk is still accreting its remaining mass onto the star. However, the recent analysis of the disk of another star in the η Cha group, ET Cha (ECHA J0843.3-7915 = RECX-15) casts some doubt on this suggestion (Woitke et al., 2011). The disk of ET Cha is also accreting (Lawson et al., 2004); it is very evolved with very low dust and gas masses, but still has a very substantial near-IR excess consistent with emission from the dust destruction radius (Woitke et al., 2011). For a 5-9 Myr population of less than 20 stars (Mamajek et al., 2000) the probability of finding 2 stars in a phase lasting only $\sim 10^5$ years is low. Overall, the evidence provided by low accretors in evolved populations suggests that current models of disk dissipation by photoevaporation with high mass loss rates may need to be re-visited. Our upper limit on $\dot{M}$ does not, however, rule out photoevaporation at the low mass loss rates predicted by the EUV photoevaporation models.

5.6 Summary and Conclusions

We used multi-wavelength observations of the CTTS RECX-11 and the WTTS RECX-1 to investigate their accretion properties. We found:

- Multi-wavelength observations provide the clearest picture of the accretion properties of a low $\dot{M}$ T Tauri star. Observations of molecular gas in the FUV may be the most sensitive accretion probe, since these lines are only present in accreting sources (Chapter 3), and their line profiles are consistent with an origin in the disk, very close to the star. In the optical and near infrared, the most sensitive indications of accretion come from high resolution observations of the Hα and He I λ10830 emission lines. These show variable and multiple redshifted absorption components which reveal the complex structure of the magnetosphere in a low $\dot{M}$ source. For very low values of $\dot{M}$, lines normally used as accretion indicators such as the Ca II IR triplet lines, arise mostly in the stellar chromosphere and are not sensitive to accretion.

- The contribution from the stellar chromosphere to the NUV flux can be substantial and may result in estimates of the accretion luminosity from U excesses that are significantly higher than the actual value of L_{acc}. For RECX-1, a K5 star that is not accreting, as determined from its narrow Hα line profile and from the lack of H_2 lines in the FUV, its chromospheric NUV excess over the photosphere of a standard dwarf star would result in incorrect estimates of $L_{acc} \sim 0.05\ L_{\odot}$ and $\dot{M} \sim 3 \times 10^{-9}\ M_{\odot}\,yr^{-1}$. For the middle K spectral range, estimates of accretion less than these limits based on methods calibrated with standard dwarf stars should be taken with caution.

- When accounting for the active chromospheres of T Tauri stars by using a WTTS as a template against which to measure the NUV excess, we determine a very low $\dot{M}$ for RECX-11, $\leq 3 \times 10^{-10}\ M_{\odot}\,yr^{-1}$.

- Given the low mass accretion rate, the high X-ray luminosity, and the advanced age of RECX-11, photoevaporation is expected to be driving the final evolution of its disk; if this was the case, the innermost disk regions, ≤ 0.1 AU should be clear. However, we find evidence for gas and dust in the innermost disk of RECX-11, as indicated by ongoing accretion, the detection of H_2 lines formed in the innermost disk, and emission from optically thick dust at the dust destruction radius at levels consistent with other CTTS. This, together with similar evidence provided by other slowly accreting, old disks, suggests that models for photoevaporation-driven disk dissipation resulting in high values of the mass loss rate should be revisited.

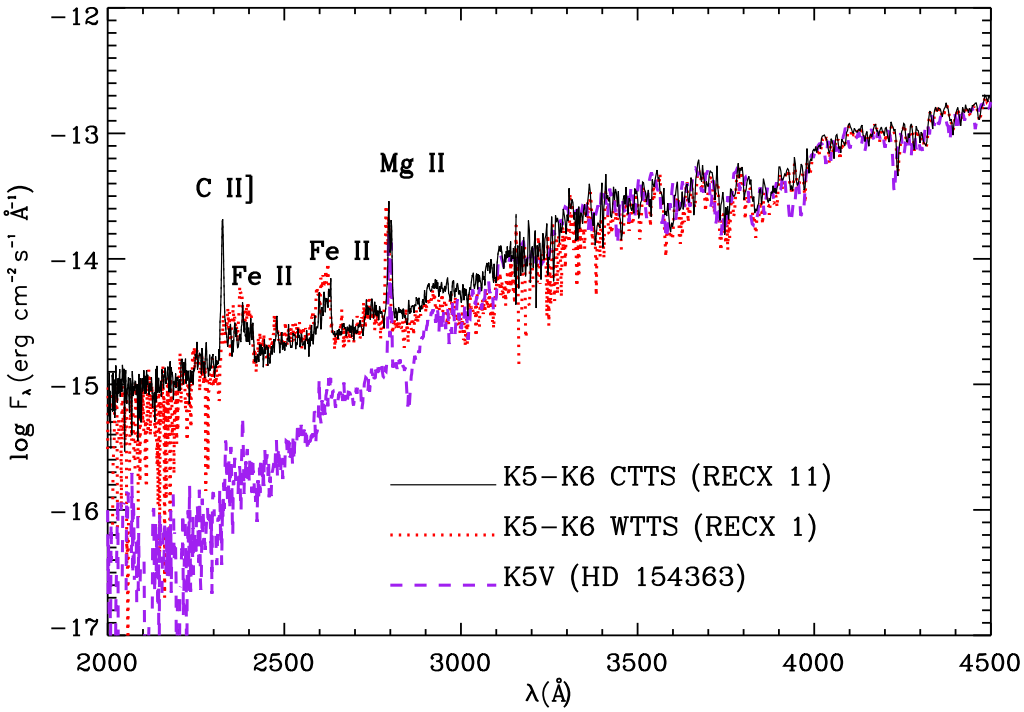

Figure 5.1. STIS spectra of the WTTS RECX-1, the CTTS RECX-11 and the dwarf standard star, HD 154363. All have K5–K6 spectral types but RECX-1 is no longer accreting while RECX-11 has ongoing accretion (Lawson et al., 2004; Sicilia-Aguilar et al., 2009; Jayawardhana et al., 2006). The spectra of the RECX-1 and RECX-11 are remarkably similar, except for the stronger C II] λ2325 line in the CTTS. The Mg II λ2800 doublet strength is comparable in the three sources (§ 5.4).

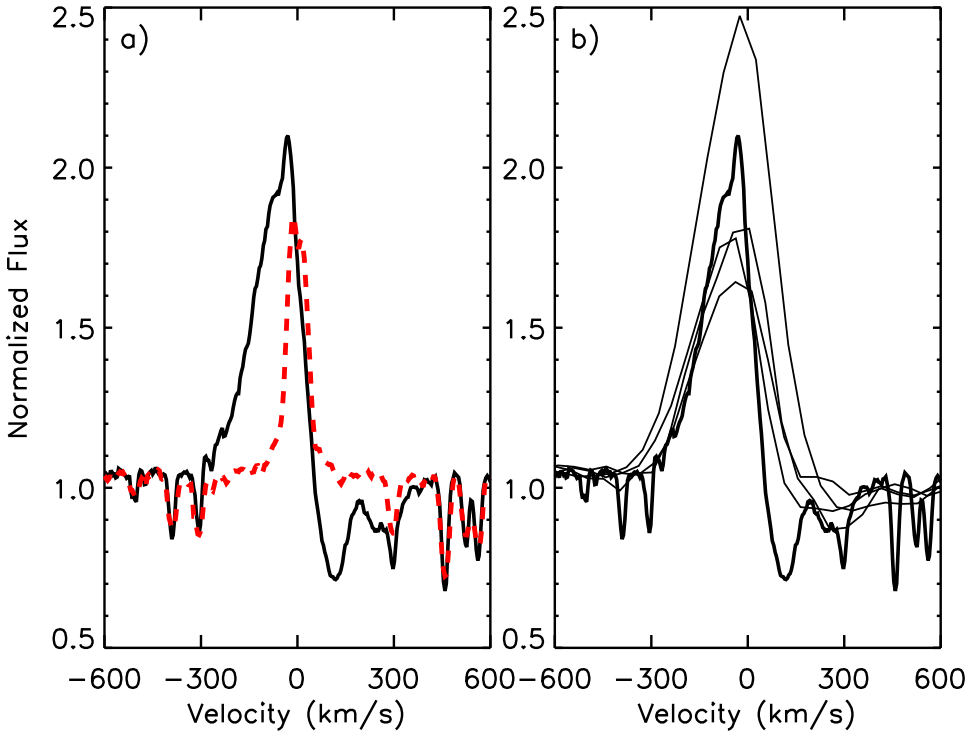

Figure 5.2. Hα line profiles. (a) MIKE spectra of RECX-11 (solid line) and RECX-1 (red dashed line). (b) SMARTS spectra of RECX-11 obtained within a few days of the HST observations. The MIKE spectrum is also shown for comparison as the thick solid line. The wide blue wing and red-shifted absorption in the Hα profile of RECX-11, characteristic of accretion, are observed in the MIKE and SMARTS data. Transient narrow red-shifted components are observed in the red wing of the lines and show the largest variability.

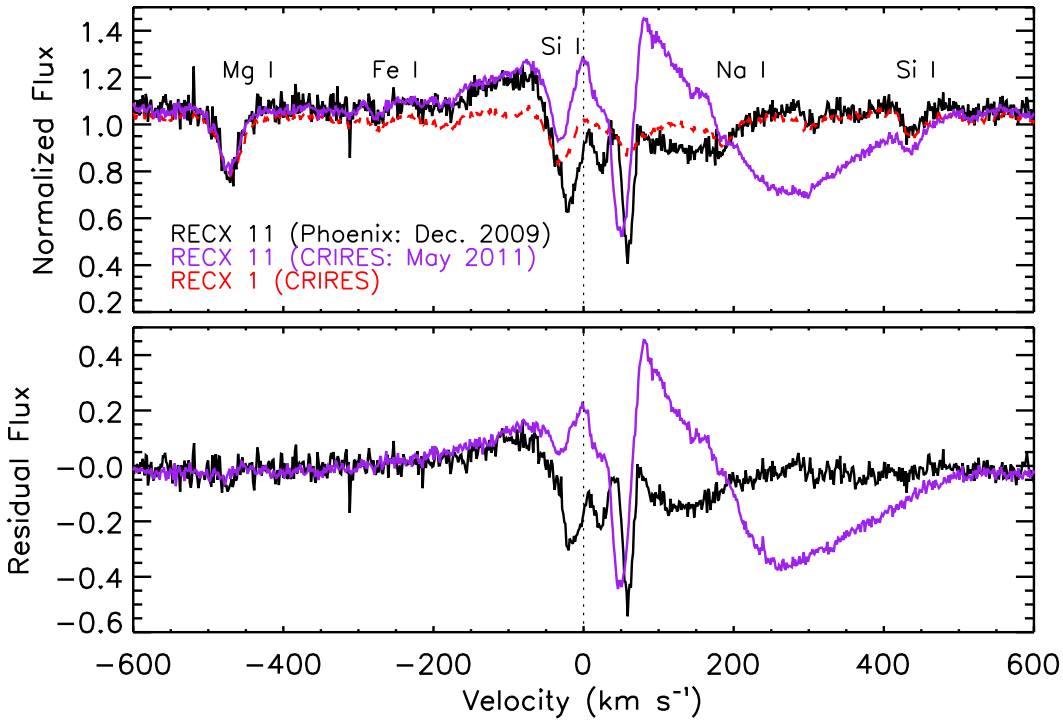

Figure 5.3. He I λ10830 profiles obtained with Phoenix and CRIRES. *Top Panel:* He I observations of RECX-11 are shown from two epochs largely separated in time by 18 months. RECX-1 is shown for comparison and photospheric lines identified by the Infrared Telescope Facility (IRTF) spectral library are designated (Rayner et al., 2009). RECX-11 shows significant variability between the two observations, including a variable redshifted emission component and a broad, high velocity redshifted absorption component characteristic of magnetospheric infall. *Bottom Panel:* He I λ10830 line profiles of RECX-11 after subtraction of the RECX-1 line profile. The Phoenix observation was degraded to the resolution of the CRIRES observations prior to subtraction of the RECX-1 profile. The photospheric lines are cleanly subtracted but the complex nature of the profile remains.

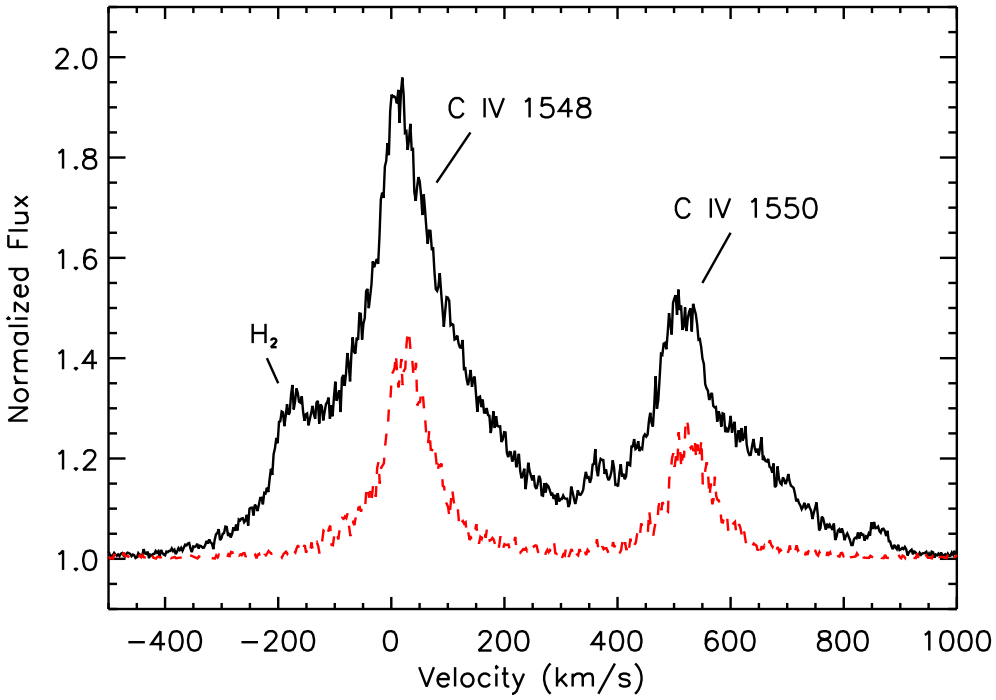

Figure 5.4. COS C IV λ1549 and λ1551 line profiles for RECX-11 (solid line) and RECX-1 (red dashed line). In agreement with other accretion indicators, the CTTS RECX-11 has broader lines than the WTTS RECX-1; the emission is expected to arise in the accretion shock and flows.

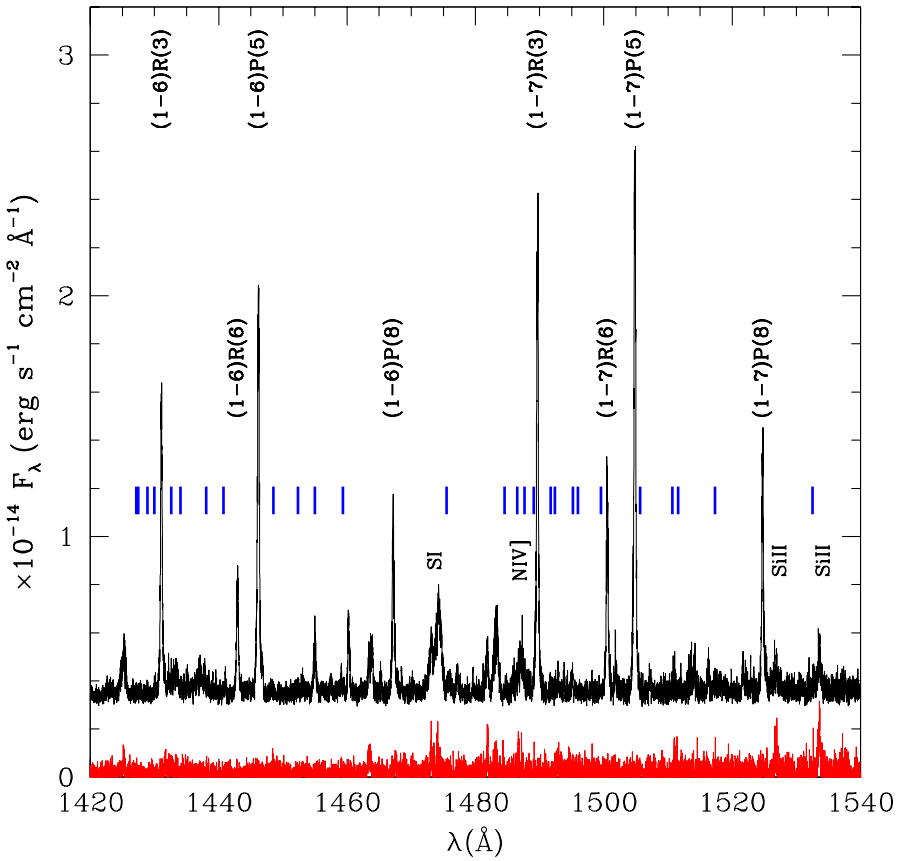

Figure 5.5. COS FUV spectra of the WTTS RECX-1 and the CTTS RECX-11. The RECX-11 spectrum (upper black line) is offset vertically for clarity. Strong lines of Lyα fluoresced H_2 and atomic lines are labeled. The blue dashes show the wavelengths at which additional H_2 emission lines from Lyα pumping may be seen. RECX-1 (lower red line) shows a lack of molecular gas lines which are apparent in RECX-11; essentially no gas exists in the inner disk region of RECX-1.

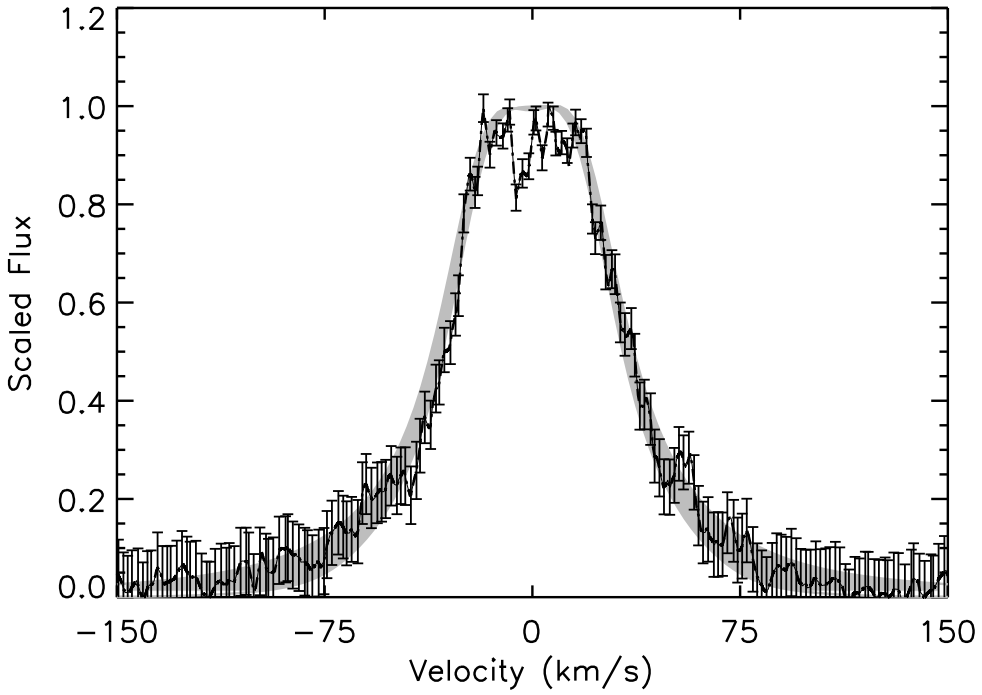

Figure 5.6. Spectrally resolved H_2 line profile. The dot-dashed line shows the flux weighted average of four H_2 lines observed with the COS G130M grating. These lines result from the (1–2) R(6) and (1–2) P(5) Lyα pumping transitions and are found in a narrow wavelength region observed with a single grating. The shaded region shows the predicted line emission originating in a Keplerian disk with inclination of 68°, inner radius $R_1 = 1 - 20\ R_*$ and outer radius, $R_2 = 450 - 500\ R_*$. The predicted line fluxes are convolved with the COS line spread function to account for instrumental effects (Kriss, 2011).

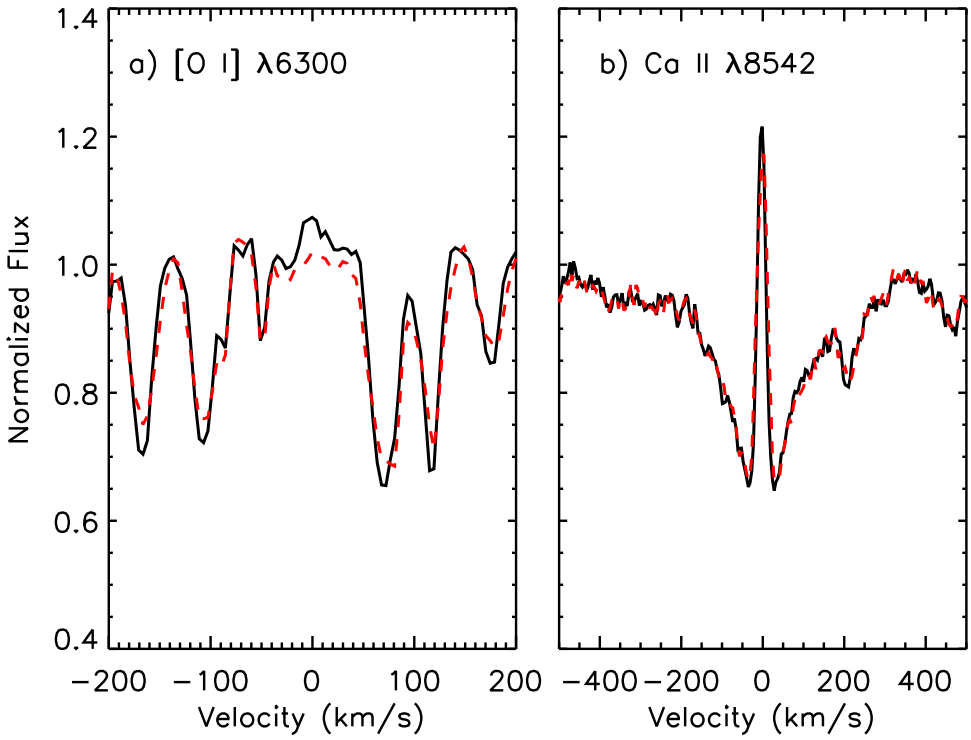

Figure 5.7. Accretion indicators. In each panel the black solid line shows the line profile of the CTTS, RECX-11, and the red dashed line shows the WTTS, RECX-1. a) [O I]. The [O I] λ6300 Å line probes wind emission in T Tauri stars. Weak [O I] emission appears to be present in RECX-11 in excess over the WTTS but the detection is $< 3\sigma$. If [O I] were present it would be additional support for accretion in RECX-11. b) Ca II. The Ca II λ8542 Å shows an emission core on the photospheric absorption line. At low $\dot{M}$, this line is dominated by chromospheric emission and cannot be used to measure accretion rates, as shown by the identical profiles of RECX-1 and RECX-11.

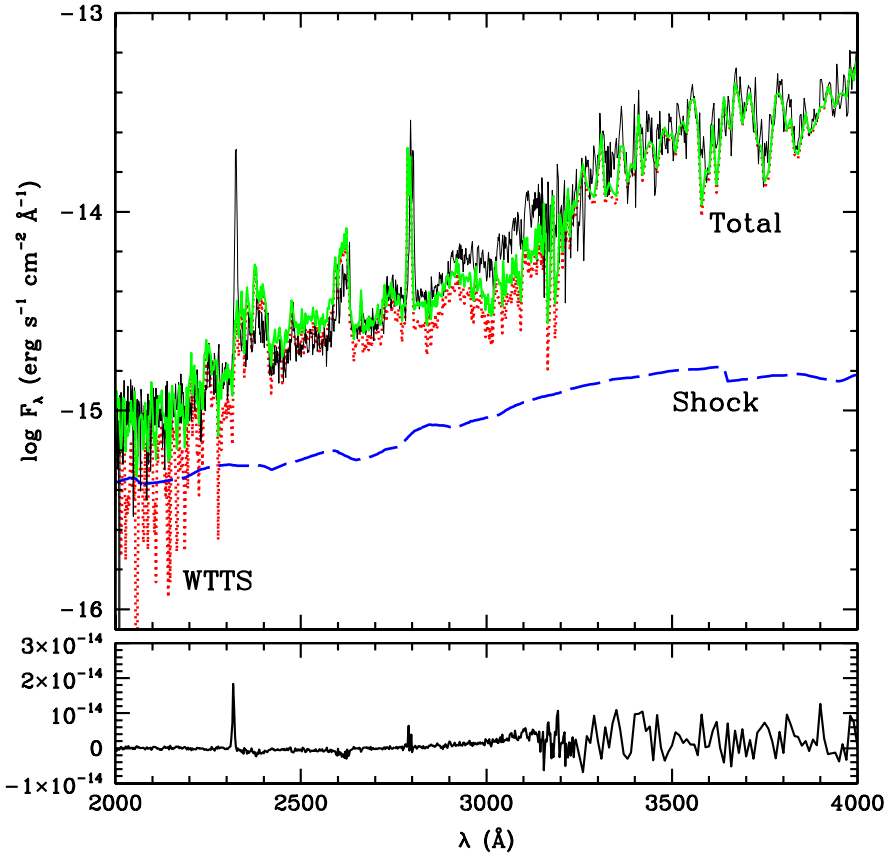

Figure 5.8. STIS spectrum of RECX-11 compared to predictions of the accretion shock model. *Top Panel:* We show the STIS spectrum of RECX-11 (thin solid line) along with the template NUV and optical emission, the WTTS RECX-1 (red dotted line), and the emission predicted from the accretion shock model (blue long dashed line), with $\dot{M} \leq 3 \times 10^{-10}$ M$_\odot$ yr^{-1}. The thick solid green spectrum is the accretion shock model added to the WTTS spectrum. *Bottom Panel:* The model (green) was subtracted from the observations (black) and the residuals are shown.

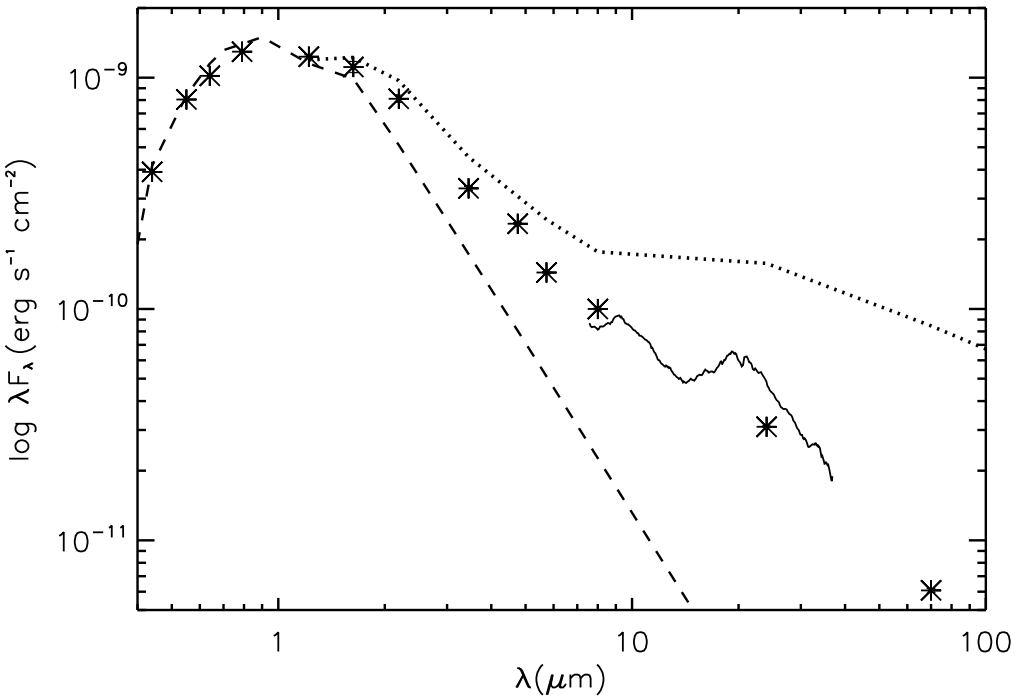

Figure 5.9. IR spectrum of RECX-11. The IRS spectrum (solid line) and *Spitzer* photometry (asterisks) show that the IR fluxes are lower than the median IR fluxes of Taurus (dotted line), yet still in excess over the photosphere (dashed line) even in the near-IR. A near-IR excess is due to dust in the inner circumstellar disk, extending all the way to the dust sublimation radius.

Table 5.1: Properties of RECX-1, RECX-11 and HD 154363

Object	Class	Spectral Type	Luminosity ($L_\odot$)	Mass ($M_\odot$)	Radius ($R_\odot$)	Distance (pc)	Age (Myr)
RECX-1	WTTS	K5–K6	1.0	0.9	1.8	97	5–9
RECX-11	CTTS	K5–K6	0.6	1.0	1.4	97	5–9
HD 154363	Dwarf	K5	0.2	0.6	0.8	11	<1400

Note: Masses for the η Cha sources were calculated from the position in the HR diagram, assuming the evolutionary tracks of Siess et al. (2000) with solar metallicity. Stellar parameters for HD154363 are from Holmberg et al. (2009) and Takeda et al. (2007).

Table 5.2: Log of Observations for RECX -1 and RECX-11

Object	RA (J2000)	DEC (J2000)	Telescope/ Instrument	Date of Obs
RECX-1	08 36 56.12	-78 56 45.3	HST/ COS G130M/G160M	2010-01-22
			HST/ STIS G230L/G430L	2010-01-22
			Magellan/ MIKE	2010-03-10
			VLT-UT1/ CRIRES	2011-05-22
RECX-11	08 47 01.28	-78 59 34.1	HST/ COS G130M/G160M	2009-12-12
			HST/ STIS G230L/G430L	2009-12-12
			Magellan/ MIKE	2010-03-10
			CTIO/ SMARTS RC Spectrograph	2009-11-26
			CTIO/ SMARTS RC Spectrograph	2009-11-27
			CTIO/ SMARTS RC Spectrograph	2009-12-15
			CTIO/ SMARTS RC Spectrograph	2009-12-19
			Gemini South/ Phoenix	2009-12-12
			VLT-UT1/ CRIRES	2011-05-22

CHAPTER 6

A Multiple- Column Model for Accretion in Low Mass T Tauri Stars

6.1 Introduction

Classical T Tauri stars (CTTS) are pre-main sequence stars which are accreting gas from their circumstellar disks, as discussed in previous chapters. The currently accepted paradigm for accretion is magnetospheric accretion, where the circumstellar disk is truncated at a few stellar radii by the stellar magnetosphere (Hartmann et al., 1994). At the truncation radius, gas is channeled along the magnetic field lines at nearly free fall velocities, until it impacts the stationary photosphere, producing an accretion shock. Accreting sources are identified by broad emission lines (like Hα and Ca II), tracing material moving near free fall velocities in the accretion streams (Edwards et al., 1994), or by an ultraviolet (UV) and U band excess over the stellar photosphere, produced by hot gas in the accretion shock (Calvet & Gullbring, 1998).

The accretion properties of young stars are best characterized by studying a large sample, including non-accreting T Tauri stars (or weak T Tauri stars, WTTS) to distinguish effects of accretion from those of enhanced magnetic activity or surface gravity. Although WTTS are no longer accreting, they retain strong magnetic fields which produce an active chromosphere. The ramped up activity in the chromosphere is seen as a UV excess over a dwarf star photosphere (Houdebine et al., 1996) and emission in lines of hydrogen and calcium, the same diagnostics of magnetospheric accretion; however, the chromospheric contribution is much weaker. Due to the similarity in tracers, it is essential to use a WTTS template when estimating the accretion rate onto the star ($\dot{M}$), especially for low $\dot{M}$ objects where the accretion

emission is comparable to that from the active chromosphere. Until now, high signal UV spectra of WTTS were not available, so dwarf spectra took their place as stellar templates, resulting in overestimated UV excesses (Chapter 5). Accurate $\dot{M}$s are vital for the understanding of disk physics; the accretion rate provides information about the surface density of the inner circumstellar disk (D'Alessio et al., 1999). For the lowest accretors, the accretion properties reveal characteristics about the final stages of the inner disk, shortly before it is dissipated.

Initial attempts to fit the shock excess assumed a single accretion spot on the stellar surface characterized by either a single temperature and density in slab models (Gullbring et al., 1998; Herczeg et al., 2004), or a single energy flux in the accretion column for accretion shock models (Calvet & Gullbring, 1998, see Section 6.3.3). These models indicated that the shocks or hot regions cover a small fraction of the stellar surface, of order $\sim$ tenths to a few percent. Recent models of the magnetosphere, calculated to reproduce spectro-polarimetric observations, revealed that the magnetic field geometry of accreting stars is extremely complex, including high order and tilted fields (Donati et al., 2008; Gregory & Donati, 2011). The accretion footprints on the stellar surface which result from field lines of varying strengths and geometries are themselves complex, ranging in size and density of the shocked material, with filling factors spanning over 10% of the stellar surface. These large filling factors have yet to be reproduced when fitting the accretion excess without significantly over-estimating the UV fluxes.

In addition to theorized large filling factors, long wavelength veiling observations are not explained by current accretion shock models. Veiling occurs when the excess emission produced in the shock fills in, or "veils", photospheric absorption lines, causing them to appear shallow when compared to a WTTS template (Hartigan et al., 1991). Veiling around 1 μm was reported in Edwards et al. (2006) and more recently in Fischer et al. (2011) and McClure et al. (2012), who showed that the amount of veiling becomes nearly constant from 0.8 to 1.4 μm. Given an accretion shock spectrum which peaks in the UV and decreases toward long wavelengths, veiling should be negligible in the near-IR. White & Hillenbrand (2004) proposed that long wavelength

veiling originates in a cool accretion component, cooler than that which describes the UV excess, while Fischer et al. (2011) found that, in some cases, the necessary filling factors of the cool component are too large for the veiling to be accretion related and instead suggested that it comes from hot gas in the inner circumstellar disk. McClure et al. (2012) successfully reproduced the observed long wavelength veiling and found feasible filling factors for the cool accretion column; the difference between the Fischer et al. (2011) and (McClure et al. 2012) results stemming from the temperatures assumed for blackbodies representing disk and accretion components. While near IR veiling measurements provide convincing evidence for a cool accretion component, they are limited by the lack of spectral information near the peak of the shock emission and result in little constraint to the high energy accretion properties.

In this Chapter, we use the accretion shock models described in Calvet & Gullbring (1998) to fit UV and optical observations of a large sample of CTTS. The sample is a part of the large *Hubble Space Telescope* (*HST*) program, The Disks, Accretion and Outflows of T Tau stars (DAO) which compiled a large dataset for each source covering a long range in wavelength with observations as close to simultaneous as possible. Observations included *HST* far UV (FUV), near UV (NUV) and optical spectra obtained with the Cosmic Origins Spectrograph (COS) and the Space Telescope Imaging Spectrograph (STIS). We focus on the NUV and optical observations which are ideal for measuring accretion excesses, whereas the FUV spectrum is complicated by molecular emission, both in lines and the continuum (Bergin et al., 2004; France et al., 2011). Attempts were made to contemporaneously (within a few nights of *HST*) obtain additional optical spectra in order to observe Hα, which was not included in the STIS spectra; these attempts were successful for over half of the sample.

Here, we improve upon treatments of the accretion shock as a single spot on the stellar surface by including multiple accretion components, a scenario more physically accurate given the geometry of the magnetosphere. With the added components, we attempt to explain long wavelength veiling by including cooler accretion columns, as suggested by White & Hillenbrand (2004) and Calvet & Gullbring (1998), from which

the emission peaks toward redder wavelengths. In Section 6.2 we discuss the data used in this chapter, both new observations and some previously published. Section 6.3 describes the process we use for calculating accretion rates and our results are presented in Section 6.4. Finally, in Section 6.5.1 we explore the range of accretion rates possible, assuming that some accretion luminosity is undetectable above the star and in Section 6.5.2 we show how our new results affect correlations between accretion indicators and $\dot{M}$, which are commonly used when UV observations are not feasible.

6.2 Observations

6.2.1 *HST* Observations

Observations were obtained with STIS on *HST* for 21 low mass CTTS and 4 WTTS between 2009 and 2012 in the large *HST* program GO 11616 (PI: G. Herczeg). The total DAO sample is larger, but for this chapter we select those sources which are low mass (spectral types K to M). STIS NUV observations used the MAMA detector and the G230L grating providing spectral coverage from 1570 to 3180 Å with R$\sim$500-1000. Optical observations were completed during the same orbit as the NUV using the G430L grating which covers 2900-5700 Å with R$\sim$530–1040, resulting in almost simultaneous NUV to optical coverage with STIS. The bright source, CV Cha, was observed with the echelle grating in the NUV (E230M). We also include two CTTS observed earlier with the STIS G230L NUV grating, BP Tau (GO program 9081; PI. Calvet) and LkCa 15 (GO program 9374; PI. Bergin).

The low-resolution STIS spectra were calibrated with custom written IDL routines following the procedures described in the STIS data handbook. The wavelengths were calibrated from the location of identified emission lines within the spectrum, and fluxes were calibrated from spectra of WD 1337+705 in the NUV and HIP 45880 in the optical. The flux calibration also includes a wavelength-dependent aperture correction. Two of the STIS spectra were previously discussed in Chapter 5

6.2.2 Ground Based Observations

We also obtained low dispersion spectra of much of the sample, covering the Hα line, using the Small and Medium Aperture Research Telescope System (SMARTS) 1.5m telescope at the Cerro Tololo Inter-American Observatory (CTIO). Sources were observed with SMARTS for a few days before and after the *HST* observations when possible, providing nearly simultaneous observations of Hα. The reduction of SMARTS spectra was described in Chapter 2.

Due to the low resolution of the SMARTS data, we supplemented the observations with existing, non-simultaneous high resolution spectra obtained with MIKE (Magellan Inamori Kyocera Echelle) on the Magellan-Clay telescope at Las Campanas Observatory in Chile, with a coverage of 4800–9000 Å and resolution, R$\sim$35,000. The data were reduced using the Image Reduction and Analysis Facility (IRAF) tasks CCDPROC, APFLATTEN, and DOECSLIT (Tody, 1993). MIKE spectra were used to calculate the V band veiling, which would not be accurate at the low resolution of the SMARTS data (Section 6.3.2). A log of all HST and ground based observations is given in Table 6.1.

6.3 Calculating Accretion Rates

6.3.1 Stellar Template: The Active Chromosphere

It is well known that enhanced chromospheric activity is characteristic of stars which have not yet reached the main sequence. A higher level of activity is inferred from lines like Hα and the Ca II infrared triplet which are in emission and also variable in young stars (Gálvez et al., 2009). Young stars also emit excess UV emission, compared to dwarf stars (Houdebine et al., 1996). Since Hα, Ca II emission lines and the UV excess are also the typical tracers of accretion, emission from the active chromosphere should be taken into account when the accretion luminosity is estimated from the UV excess over the photosphere. While chromospheric emission is not a large contaminant for strong accretors, it is extremely significant when $\dot{M}$ is low. In Chapter 5 we demonstrated how the emission from an active chromosphere can mask all evidence

of accretion for the lowest accretors. In these cases, additional tracers of accretion or material near the magnetospheric truncation radius (like FUV H_2 emission lines) are necessary to confirm that a source is accreting.

Previous estimates of $\dot{M}$ have mainly relied on dwarf photospheres as templates against which to measure the U band or UV excess (Romaniello et al., 2004). A better estimate of the excess could be found using a WTTS template but, until now, WTTS with good signal in the UV were not available. As part of the DAO sample, WTTS were included to act as templates, covering the range of spectral types of the accreting sample (Table 6.2). Figure 6.1 shows the WTTS templates compared to main sequence dwarf stars with the same spectral type; dwarf spectra were scaled to the WTTS at 5500 Å. STIS observations of main sequence stars were found in the *HST* Next Generation Spectral Library (Heap & Lindler, 2007). We compared the luminosity in the WTTS to that of the dwarf between 2000 and 3000 Å and found that the WTTS had NUV luminosities $\sim$3$\times$ higher than the dwarf stars. In the following analysis, we use the WTTS with the closest spectral type match to each CTTS as the stellar template.

6.3.2 Veiling By Shock Emission

The excess emission produced in the shock can contribute significantly to the total luminosity of the CTTS, making it difficult to determine the luminosity of the star itself. However, veiled absorption lines provide a diagnostic of the relative contributions from the star and shock (Gullbring et al., 1998). Veiling occurs when excess emission is added to the spectrum of the star, filling in the photospheric absorption lines (Hartigan et al., 1991), so by comparing the depth of absorption lines in the CTTS to a WTTS, we have an estimate of the veiling continuum. When available, we used the veiling at V, published in Edwards et al. (2006), which provides a compilation from the literature. For a small sample of the sources with unpublished veiling (CS Cha, CV Cha, DM Tau, LkCa 15, RECX11, RECX 15 and TWA 3a) we calculated r_V from high resolution optical spectra obtained with MIKE. Following the method of Hartigan et al. (1989), we compared the depths of photospheric absorption

lines of each CTTS to a WTTS with the same spectral type. A WTTS is a much better veiling template than a dwarf star because the surface gravity and chromospheric activity of the young stars alter the photospheric absorption lines (McClure et al. 2012). We show three examples of different degrees of veiling observed in our MIKE spectra in Figure 6.2.

Based on the veiling measurements near V band, we scale our WTTS templates to each CTTS using,

$$F_{\lambda,WTTS} = F_{\lambda,CTTS}/(1 + r_\lambda), \tag{6.1}$$

where $F_{\lambda,WTTS}$ and $F_{\lambda,CTTS}$ are the continuum fluxes of the WTTS and CTTS at a given wavelength, respectively. $r_\lambda = F_{veil}/F_{cont}$, is the measured veiling at that wavelength, where F_{veil} is the excess continuum emission added to the photospheric spectrum and F_{cont} is the continuum flux. It is important to note that none of our V band veilings are simultaneous to the STIS UV and optical spectra. This presents an error in our estimated $\dot{M}$ because CTTS are known to be variable and as $\dot{M}$ (and the excess continuum emission) change, the amount of veiling will reflect this (Alencar et al., 2012). However, the low resolution of the simultaneous SMARTS optical spectra prohibited accurate r_V estimates, so we are left with non-simultaneous veiling estimates. This will be more important for the high $\dot{M}$ objects than for the low $\dot{M}$ sources, where errors are expected to be small because large accretion outbursts are unlikely.

6.3.3 Accretion Shock Model

A full description of the model used to characterize the accretion shock can be found in Calvet & Gullbring (1998) but here we review the main points. The current picture of material accretion in the inner disk of CTTS is magnetospheric accretion. The material falls onto the star along the magnetic field lines, which creates columns of accreting material that impact the stellar photosphere. When the material traveling at the free fall velocity, v_s, hits the stationary photosphere a shock is created. The

velocity of the material is given by

$$v_s = \left(\frac{2GM_*}{R_*}\right)^{1/2} \left(1 - \frac{R_*}{R_i}\right)^{1/2}, \tag{6.2}$$

where M_* and R_* are the stellar mass and radius, respectively, and R_i (assumed to be 5 R_*) is the radius at which the magnetosphere truncates the disk (Calvet & Gullbring, 1998).

The model of the accretion column is simplified by assuming that it has a plane parallel geometry and is perpendicular to the stellar photosphere. The shock formed at the base of the accretion column effectively reduces the velocity of the infalling material in order for it to join the star at the photosphere, converting the kinetic energy into thermal energy, and causing the temperature to increase sharply. In the strong shock approximation, which is used because the material is traveling at high velocities, the temperature immediately after the shock is described by

$$T_s = 8.6 \times 10^5\, K \left(\frac{M_*}{0.5 M_\odot}\right) \left(\frac{R_*}{2R_\odot}\right)^{-1} \tag{6.3}$$

(Calvet & Gullbring, 1998). At these high temperatures, the shocked material emits soft X-rays into the pre-shock, post-shock and the photosphere below the shock. This radiation heats the material in these regions causing it to emit the observed excess continuum emission.

In this treatment, the emission from the accretion column is characterized by two parameters, $\mathcal{F}$ and f, which are the total energy flux in the accretion column ($\mathcal{F} = 1/2\rho v_s^3$) and the filling factor (or fraction of the surface of the star which is covered by the accretion columns), respectively. Changes in the filling factor, f, cause the shock spectrum to increase or decrease independent of wavelength, in essence scaling the luminosity of the emission. $\mathcal{F}$ acts to change the peak wavelength of the accretion shock emission, producing blackbody- like behavior. Figure 6.3 shows how the shock spectrum changes for different values of $\mathcal{F}$, assuming typical values for M_* and R_*. As $\mathcal{F}$ increases, more energy is deposited on the stellar surface, increasing

the temperature of the photosphere below the shock. This region behaves as the photosphere of a star with an earlier spectral type than that of the undisturbed photosphere. High $\mathcal{F}$ columns have temperatures up to 9000 K, whereas low $\mathcal{F}$ columns are cooler, around 5000–6000 K, producing the wavelength shift between columns with different $\mathcal{F}$s. For the lowest value of $\mathcal{F}$, the emission peaks around 6000–7000 Å whereas for the model with the highest $\mathcal{F}$, the emission peaks between 2000 and 3000 Å.

We use this property of the accretion column emission to explain excesses at both short and long wavelengths when attempting to fit the DAO observations. In the following analysis we refer to accretion columns with energy fluxes of $\mathcal{F} = 10^{10} - 3 \times 10^{10}$ erg s^{-1} cm^{-3} as "low $\mathcal{F}$" columns and those characterized by $\mathcal{F} = 3 \times 10^{11} - 10^{12}$ erg s^{-1} cm^{-3} as "high $\mathcal{F}$" columns. This range allows for blackbody-like spectra with temperatures ranging between 5000 and 10,000 K (Calvet & Gullbring, 1998), or, from slightly hotter than star to the high temperatures needed to fit the UV excess. Note that as $\mathcal{F}$ decreases, larger values of f are needed to produce the same amount of flux as a high $\mathcal{F}$ accretion column. $\dot{M}$ can be calculated for each accretion column, with $\mathcal{F}$ and f known, using

$$\dot{M} = \frac{8\pi R_*^2}{v_s^2} \mathcal{F} f. \tag{6.4}$$

(Gullbring et al., 2000). The total $\dot{M}$ is a sum of the contributions from each column and from $\dot{M}$ we may determine L_{acc} using,

$$L_{acc} = \frac{G M_* \dot{M}}{R_*} (1 - \frac{R_*}{R_i}). \tag{6.5}$$

6.4 Results

In this analysis we include, for the first time, multiple accretion columns with a range in energy flux; specifically, we add low $\mathcal{F}$ accretion columns to fit the red optical excess and the veiling at 1 μm. 1 μm veilings are known for only a subset of our sample (10 sources) and of that subset, the veiling is >0.1 for only 7 sources

(Edwards et al., 2006). For the remaining sources, we fit the NUV and optical excess without constraining the 1 μm veiling.

The spectra were de-reddened using the A_V values in Table 6.3 and the reddening law of Whittet et al. (2004). UV emission is extremely sensitive to reddening assumptions, with $A_\lambda > 2 \times A_V$ near 2500 Å and corrections are complicated by uncertain UV reddening laws. Calvet et al. (2004) compared UV reddening laws and found that the extinction law towards a B star behind the Taurus Molecular Cloud (Whittet et al., 2004) was appropriate for sources in Taurus and similar environemnts, where the grain sizes in the cloud are not significantly different from those in the interstellar medium. We used values of A_V from Furlan et al. (2009) or Furlan et al. (2006) for the sources in Taurus and Chamaeleon I, which were computed by comparing observed $V-I$, $I-J$, or $J-H$ colors to expected photospheric colors in Kenyon & Hartmann (1995). For the remaining sources (TWA 3a, RECX 11 and RECX15) we assume A_V=0 (Webb et al., 1999; Luhman & Steeghs, 2004).

We calculated the stellar luminosity from the flux in the J band of the photosphere using the bolometric correction of Kenyon & Hartmann (1995). The photospheric J band flux was obtained by scaling de-reddened Two Micron All Sky Survey (Skrutskie et al., 2006, 2MASS) J magnitudes by the veiling at 1 μm. We then used the Siess et al. (2000) evolutionary tracks to determine the masses of the sources in the sample. These stellar properties are listed in Table 6.3.

To find the best fit of the accretion shock models to the STIS and SMARTS spectra for each source, we calculated the emission from accretion columns spanning $\mathcal{F} = 10^{10} - 10^{12}$ erg s^{-1} cm^{-3}, using the M_* and R_* from Table 6.3. We allowed the filling factor, f, to vary independently for each accretion column and then summed the flux from each column with that of the WTTS, scaled to the CTTS by the veiling at V. The spectrum of the final model is given by;

$$F_\lambda(model) = \Sigma_i(F_\lambda(column, \mathcal{F}_i) \times f(\mathcal{F}_i)) + F_\lambda(WTTS), \tag{6.6}$$

where $F_\lambda(model)$ is the flux in the model, $F_\lambda(WTTS)$ is the scaled flux of the WTTS,

$F_\lambda(column, \mathcal{F}_i)$ is the flux from an accretion column with energy flux $\mathcal{F}_i$ and $f(\mathcal{F}_i)$ is the filling factor of a column with energy flux $\mathcal{F}_i$, where $\mathcal{F}_i$=$10^{10},\ 3\times10^{10},\ 10^{11},\ 3\times10^{11},\ 10^{12}$ erg s^{-1} cm^{-3}.

When determining the best fit model, we isolated continuum regions because the accretion shock models do not attempt to reproduce line emission produced in the shock and calculated the χ^2_{red}, as

$$\chi^2_{red} = \frac{1}{N}\Sigma_{i=0}^{N}\frac{(F_\lambda(model) - F_\lambda(CTTS))^2}{E_\lambda(CTTS)^2} \tag{6.7}$$

where N is the number of continuum wavelengths which contribute to the fit, $F_\lambda(CTTS)$ represents the de-reddened CTTS spectrum and $E_\lambda(CTTS)$ is the error in the observed fluxes. The best fit models were chosen on the basis of having the lowest χ^2_{red} fit in addition to re-producing veiling estimates at 1 μm from Edwards et al. (2006). The filling factor of each contributing column in the best fit model is given in Table 6.4; columns with $f = 0$ do not contribute to the model fluxes. Finally, we calculated $\dot{M}$ using Equations 6.2, 6.4 and,

$$\dot{M} = \frac{8\pi R_*^2}{v_s^2} \times \Sigma_i(\mathcal{F}_i \times f(\mathcal{F}_i)) \tag{6.8}$$

Basically, $\dot{M}$ is calculated for each contributing column and then the $\dot{M}$s are summed. Estimated $\dot{M}$s are listed in Table 6.5. An important result is that, by including the low $\mathcal{F}$ columns to fit the red veiling, we find significantly higher filling factors than would be needed to fit the UV excess alone (Tables 6.4 and 6.5). Given that models of the magnetosphere predict large f, multi-component accretion columns are a better representation of the physical geometry of the system.

The best fit of the accretion shock models to the de-reddened NUV and optical spectra are shown in Figures 6.4 – 6.7. Overall, we found good fits between the models and the observed spectra, with a few exceptions. For the later spectral types, especially the M stars, the models did not reproduce a rise in the observed spectra between 2000 and 3000 Å (Figure 6.7). This spectral region is populated with Fe

emission lines, which are unresolved at the STIS resolution. The Fe lines may be produced in accretion related flows (Herczeg et al., 2006); however, they are also observed in the WTTS templates, so they appear to have a chromospheric component. They become more apparent at later spectral types, as the photospheric emission in the UV decreases. For DK Tau, we were unable to reproduce the 1 μm veiling, likely because of variability. In Edwards et al. (2006), the veiling at V is equal to the veiling at 1 μm, requiring an abnormally red accretion spectrum, which is not supported by the observations. The two veiling measurements were not simultaneous, so it is possible that $\dot{M}$ was higher when the IR observations were obtained. Finally, we do not attempt to fit the FUV spectrum because the continuum at <1700 Å has contributions from H_2 in the disk, which are not included in the accretion shock model.

Figures 6.4 – 6.7 also include non-simultaneous photometry from the literature, de-reddened using A_V from Table 6.3. When available, we used the range of optical photometry from Herbst et al. (1994) and this range is shown as the green error bars. The photometry for the remaining CTTS came from the following sources; CV Cha (Lawson et al., 1996), GM Aur, IP Tau, LkCa 15 and V836 Tau (Kenyon & Hartmann, 1995), RECX 11 and RECX 15 (Sicilia-Aguilar et al., 2009) and TWA 3a (Gregorio-Hetem et al., 1992). The models shown do not attempt to fit the photometry because it is not simultaneous, but we use the photometry to look for evidence of high amplitude variability. Most of the photometry agrees with the STIS and SMARTS spectra and is therefore well fit by the models. For a small sample of sources, the STIS spectra are slightly lower than expected from the photometry, RW Aur, FM Tau, IP Tau, V836 Tau, RECX 15 and TWA 3A. Except for RW Aur and FM Tau, the photometry for these sources is single epoch, therefore, the spectra may be representative of typical variability, were there multi-epoch observations. The NUV and optical spectra of HN Tau are significantly higher than the range of photometry from Herbst et al. (1994), but this source has been shown to display large increases in brightness over several years (Grankin et al., 2007).

In Figure 6.8 we compare the $\dot{M}$s calculated here with those from two previous

studies of young stars in Taurus. The first, Valenti et al. (1993), fit optical spectra with coverage from 3400 to 5000 Å of Taurus CTTS using a hydrogen slab model and a WTTS template. The slab was characterized by the temperature, number density, thickness and coverage on the stellar surface. The second study, by Gullbring et al. (1998), used similar assumptions to those of Valenti et al. (1993) and therefore, their accretion rates are in good agreement. Gullbring et al. (1998) notes that the major differences between the two come from choices of A_V and the evolutionary tracks used to determine M_*.

Compared to the Valenti et al. (1993) and Gullbring et al. (1998), our $\dot{M}$s tend to be higher. Significant differences in our method include: 1) we used accretion shock models as opposed to slab models, 2) we had estimates of the chromospheric contribution to the NUV excess and 3) we used estimates of the excess at 1 μm to constrain emission from a cooler accretion component. These last two tend to cancel each other out; the reduction in the shock excess due to the active chromosphere is countered by an increase in the shock excess at long wavelengths as indicated by the 1 μm veilings. Both accretion and slab models have been shown to fit the UV and blue excesses (Gullbring et al., 2000; Calvet et al., 2004; Herczeg et al., 2004; Herczeg & Hillenbrand, 2008) so the difference is not likely in the models. The reason for the discrepancy is different from source to source. In some cases our assumed A_Vs are higher, increasing our $\dot{M}$s; in general our A_Vs are slightly higher than those assumed in Gullbring et al. (1998). For the sources with the highest veiling, the red excess is greater than the NUV decrement to the excess from the chromosphere, so the two do not completely cancel, again resulting in higher $\dot{M}$.

6.5 Discussion

6.5.1 Hidden Accretion Emission

Table 6.4 shows that a low $\mathcal{F}$ column is not always needed to fit the excess emission in certain CTTS. For these objects, the lack of a red excess negates the need for a low $\mathcal{F}$ column; however, it does not rule one out. In Chapter 5, we showed that emis-

sion produced in the accretion shock may be hidden by the intrinsic stellar emission (specifically the active stellar chromosphere). Here, we estimate how much hidden flux may be present for sources with no detectable red excess and the implications for determinations of $\dot{M}$. In Figure 6.9 we show two model fits to the spectrum of V836 Tau. In the left panel, the best fit model is produced with only a high $\mathcal{F}$ column, no additional accretion columns are needed because no red excess is observed (Table 6.4). In the right panel, we assume that the low $\mathcal{F}$ columns exist, but the emission from the column is not detectable above the stellar component. For V836 Tau we find that the contribution to the accretion emission that may be hidden below the stellar emission is approximately equal to that in the high $\mathcal{F}$ column, doubling the estimated accretion rate. This new model results in limited veiling at 1 μm, with $r_{1\ \mu m}$=0.1, within the errors of veiling estimates.

We perform this analysis for all sources which had $f = 0$ for the low $\mathcal{F}$ columns in the initial fit, with the constraints that the NUV and optical fluxes are not overestimated by the new models, and that the veiling at 1 μm remains less than 0.1. Using this method, we calculate upper limits on $\dot{M}$ and the filling factor, listed in Table 6.5, where the differences in the two filling factors comes from increasing $f(1 \times 10^{10})$ from its value in Table 6.4. These additional low $\mathcal{F}$ accretion columns impact our understanding of magnetospheric accretion because they increase the expected $\dot{M}$ along with the filling factors. For the example shown in Figure 6.9, the accretion rate is slightly more than doubled when we assume some shock emission is hidden, but the filling factor may be up to 100 times higher. This increases the filling factor from $<$0.1% to a few percent, better in line with the models of the accretion footprints produced by complex magnetic field geometries (Romanova et al., 2012).

6.5.2 Correlations with Accretion Indicators

Measuring the UV excess is by far the best method for determining $\dot{M}$ but UV observations are difficult to obtain. For this reason it is common to use an indicator of accretion easily accessible in the optical or near-IR which has been calibrated with $\dot{M}$s calculated for the few sources with UV observations. Both the EW(Hα) and

the width of Hα at 10% of the maximum flux are often used as accretion proxies (White & Basri, 2003; Natta et al., 2004). The width of Hα at 10% is favorable because the wings trace the fast moving material in the accretion flows (Muzerolle et al., 2001). Also, the EW(Hα) saturates for the highest accretors, or sources with the largest veiling (Muzerolle et al., 1998a). Correlations between Hα 10% width have been widely used; however there is considerable scatter because Hα and the UV excess have not been measured simultaneously. The dataset presented here, with UV and optical observations separated by less than one to a few days, would be ideal for this analysis; however, the resolution of the SMARTS optical spectra is too low to accurately measure the 10% width of Hα, so we focus on the EW(Hα).

In Figure 6.10, $\dot{M}$ and EW(Hα) are plotted for the sample of our sources which had nearly simultaneous SMARTS optical and UV observations. There is no clear relation between EW(Hα) and $\dot{M}$. Two sources, DM Tau and RECX 15, have relatively low $\dot{M}$ but significant EW(Hα), showing that it is not a good tracer of $\dot{M}$. However, we can measure the flux of the Hα line in the SMARTS data and $L_{H\alpha}$ is then calculated with distances from Table 6.3. In Figure 6.11 we see a correlation between Hα luminosity and $\dot{M}$ (or L_{acc}) with a Pearson correlation coefficient of 0.9. The following equations describe the trend between $L_{H\alpha}$ and $\dot{M}$ or L_{acc}.

$$\log(\dot{M}) = 1.0(\pm0.2)\log(L_{H\alpha}) - 5.6(\pm0.6) \tag{6.9}$$

$$\log(L_{acc}) = 0.9(\pm0.2)\log(L_{H\alpha}) + 1.3(\pm0.6) \tag{6.10}$$

Hβ is less often used to trace accretion than Hα but has been shown to correlate with $\dot{M}$ (Muzerolle et al., 2001). We compare the luminosities in Hβ ($L_{H\beta}$) measured from the simultaneous STIS optical spectra to both $\dot{M}$ and L_{acc} in Figure 6.12. We find strong correlations between the line luminosity and the accretion rates and luminosities, both with correlation coefficients $\sim$0.9. The lines shown in Figure 6.12 which describe the trends are given by the following equations;

$$\log(\dot{\mathrm{M}}) = 1.5(\pm0.2)\log(\mathrm{L}_{\mathrm{H}\beta}) - 3.4(\pm0.6) \tag{6.11}$$

$$\log(\mathrm{L}_{\mathrm{acc}}) = 1.5(\pm0.2)\log(\mathrm{L}_{\mathrm{H}\beta}) + 3.9(\pm0.7) \tag{6.12}$$

Another commonly used tracer of accretion is the Ca II infrared triplet line emission (Rigliaco et al., 2011). Our SMARTS spectra did not cover the infrared triplet lines of Ca II, but in our STIS optical data, we observe the Ca II H and K lines. The H line at λ3969 Å is blended with the λ3970 Å Hϵ line at the resolution of STIS, so we only consider the contamination-free K line. Similar to the Hα and Hβ line luminosities, the Ca II K line at λ3934 Å appears to have an origin in accretion related processes, as there is a clear trend between the Ca II K luminosity ($\mathrm{L}_{\mathrm{CaII\ K}}$) and $\dot{M}$ or L_{acc} (with correlation coefficients of 0.8 in each case). We show the trends in Figure 6.13 and give the relations in the following;

$$\log(\dot{\mathrm{M}}) = 0.9(\pm0.2)\log(\mathrm{L}_{\mathrm{CaII\ K}}) - 5.2(\pm0.6) \tag{6.13}$$

$$\log(\mathrm{L}_{\mathrm{acc}}) = 0.9(\pm0.2)\log(\mathrm{L}_{\mathrm{CaII\ K}}) + 2.2(\pm0.6) \tag{6.14}$$

Included in our NUV spectra are two emission lines which have been shown to correlate with accretion properties. Calvet et al. (2004) analyzed NUV spectra for a sample of intermediate mass T Tauri stars and found that luminosities of C II] λ2325 Å and Mg II λ2800 Å increased with L_{acc}. We expected a similar trend due to simultaneous observations of the lines and accretion excess and Figure 6.14 shows a tight correlation. Mg II is also a tracer of chromospheric activity, and is detected in each of the WTTS templates, but the contribution to the luminosity is likely saturated at the age of our sample (Cardini & Cassatella, 2007). C II] is not observed in WTTS; however, is easily identified even in low $\dot{M}$ objects and correlates with L_{acc}. C II], therefore, appears to be a very sensitive tracer of accretion, observable even when the NUV continuum excess is not. Relations between line fluxes and L_{acc}

are given by;

$$\log(L_{acc}) = 1.0(\pm0.2)\log(L_{C\ II]}) + 2.6(\pm0.6) \tag{6.15}$$

$$\log(L_{acc}) = 1.1(\pm0.1)\log(L_{Mg\ II}) + 2.0(\pm0.4) \tag{6.16}$$

6.6 Summary and Conclusions

We used a large sample of T Tauri stars with complete spectral coverage in the FUV, NUV and optical to analyze the accretion properties of young stars. The main results are summarized here.

- The NUV fluxes of WTTS are $\sim$3$\times$ stronger than dwarf stars of the same spectral type, due to enhanced chromospheric activity in young stars. This excess can introduce uncertainties in the estimate of the NUV excess produced by accretion if the correct templates are not used. By using WTTS templates with good signal to noise in the UV, which first became available in the DAO sample, we were able to distinguish chromospheric excesses from accretion excess when calculating accretion rates.

- Accretion shock models which explain the NUV excess cannot describe both large filling factors predicted by models of the magnetic field distribution and non-zero long wavelength veiling, observed in 1 μm data. Here, we used multi-column accretion shock models. The shock emission is assumed to be a combination of high energy flux ($\mathcal{F}$) columns which peak in the UV and low $\mathcal{F}$ accretion columns which peak at redder, optical wavelengths. By including a variety of accretion columns, red veiling may be explained and due to the larger filling factors of low $\mathcal{F}$ accretion columns, expected large filling factors are also understood.

- Low $\mathcal{F}$ accretion columns which can explain 1 μm veiling in high accretors, may be present even when no red excess is observed. The intrinsic stellar emission,

especially the active chromosphere, may hide this accretion component at low $\dot{M}$. We measured the maximum emission of a cool column that can be hidden by the stellar emission and determined the filling factor of the cool column. We found large surface coverage, even in sources without veiling at 1 μm. In some cases the red excess was equal to the excess flux in the NUV, doubling $\dot{M}$.

- We used, for the first time, simultaneous measurements of emission line luminosities and accretion luminosities ti search for indicators of accretion. We found clear trends between the luminosities of Hα, Hβ, Ca II K, Mg II and CII]. No correlation is found between EW(Hα) and $\dot{M}$, even with simultaneous observations. C II] may be a sensitive tracer of accretion at low $\dot{M}$, as it is observed in all the CTTS in our sample, even those with no NUV accretion excess.

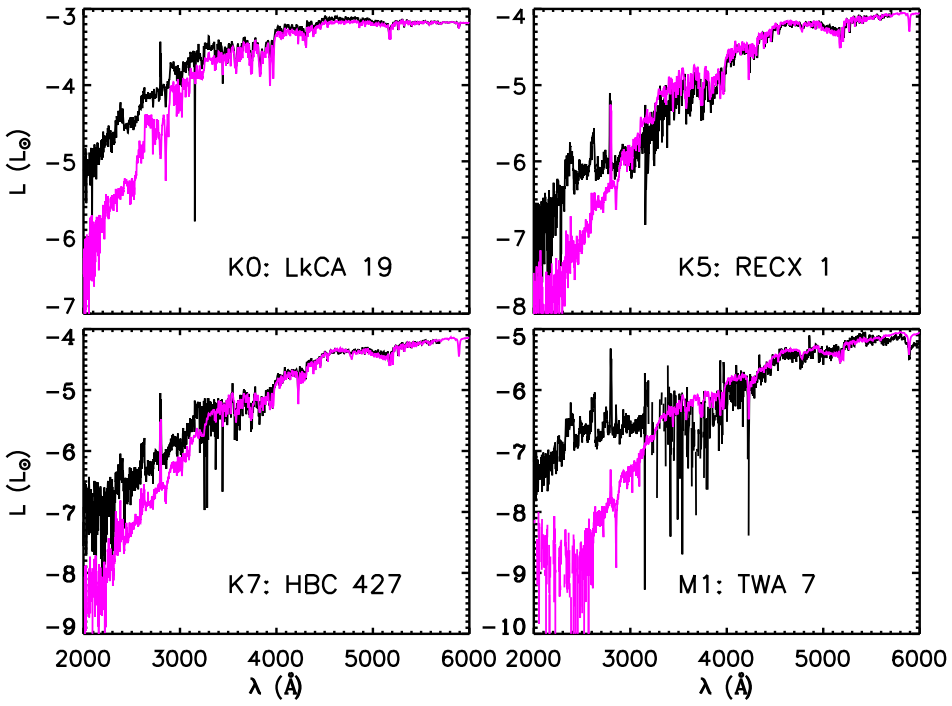

Figure 6.1. Comparison of WTTS and dwarf star templates. In each panel the black line is the WTTS observed as part of the DAO sample and the magenta line is a dwarf standard of the same spectral type, taken from the STIS Next Generation Spectral Library. The WTTS excess in the NUV is produced by an active chromosphere in young stars.

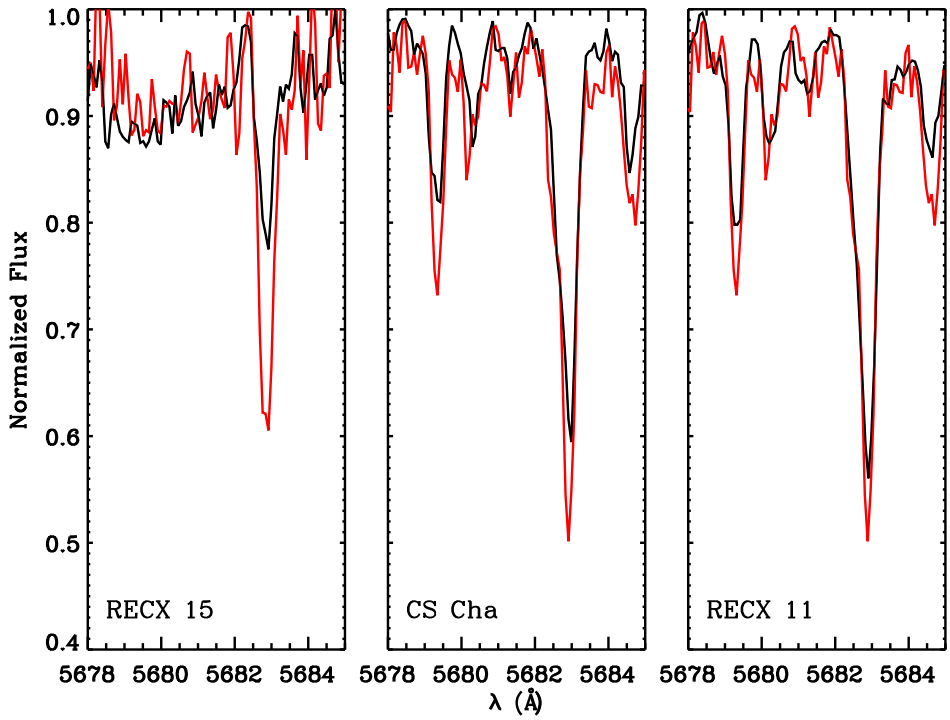

Figure 6.2. Veiling in MIKE spectra. The panels show three CTTS (black) observed with MIKE which have different degrees of veiling compared to a WTTS of the same spectral type (red). RECX 15 (left panel) has significantly more veiling than RECX11 (right panel), observed as very shallow absorption lines.

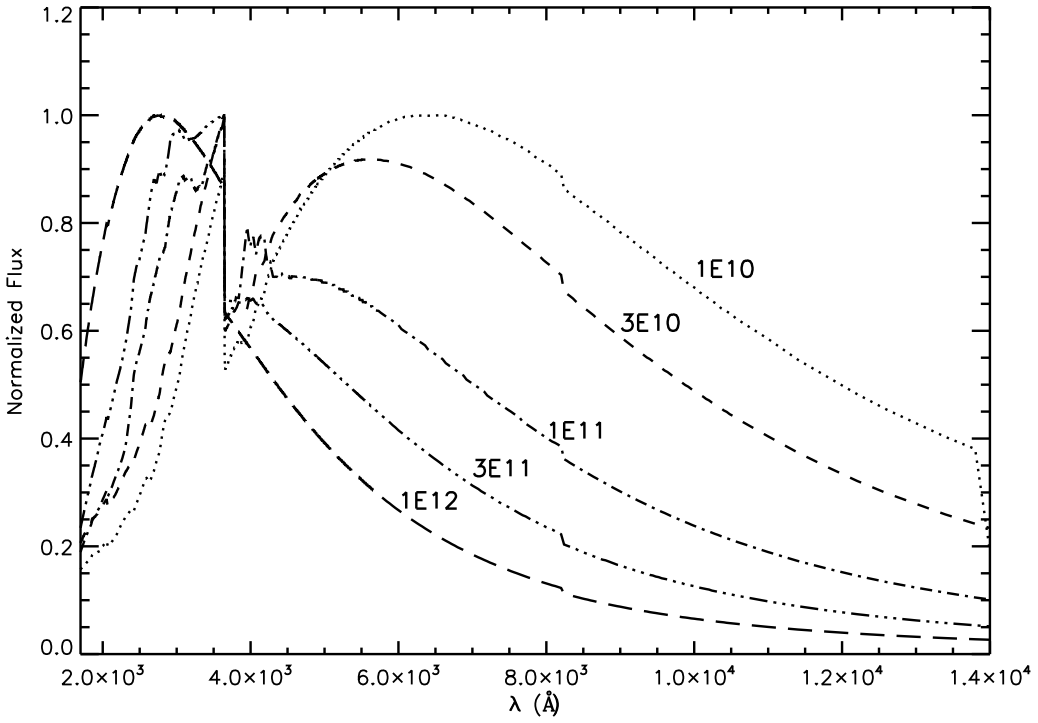

Figure 6.3. Fluxes of accretion shock models with varying energy flux ($\mathcal{F}$). Each line shows the normalized emission from an accretion column with a different value of $\mathcal{F}$, listed next to each spectrum, spanning the range from $\mathcal{F} = 10^{10} - 10^{12}$ erg s^{-1} cm^{-3}. The low $\mathcal{F}$ models have shock emission which peaks at longer wavelengths.

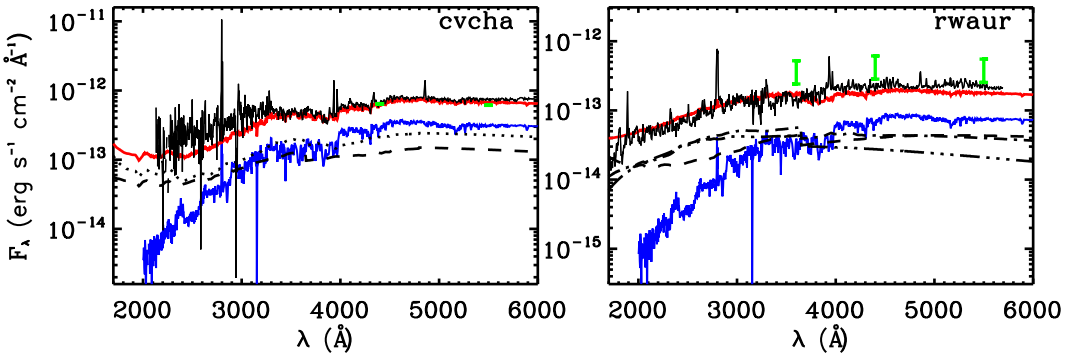

Figure 6.4. Spectra of late G, early K spectral type CTTS in the DAO sample: CV Cha and RW Aur. We fit the STIS NUV and optical spectra with emission from accretion columns plus a WTTS spectrum. In each panel the black spectrum is the CTTS and the blue spectrum is the WTTS, LkCa 19. The broken black lines represent accretion shock models with different $\mathcal{F}$ values, defined as in Figure 6.3. The red line is the best model fit to the data, adding the emission from the different shock models to the WTTS spectrum. The green error bars indicate non-simultaneous photometry, representing the range observed in multi-epoch observations when available.

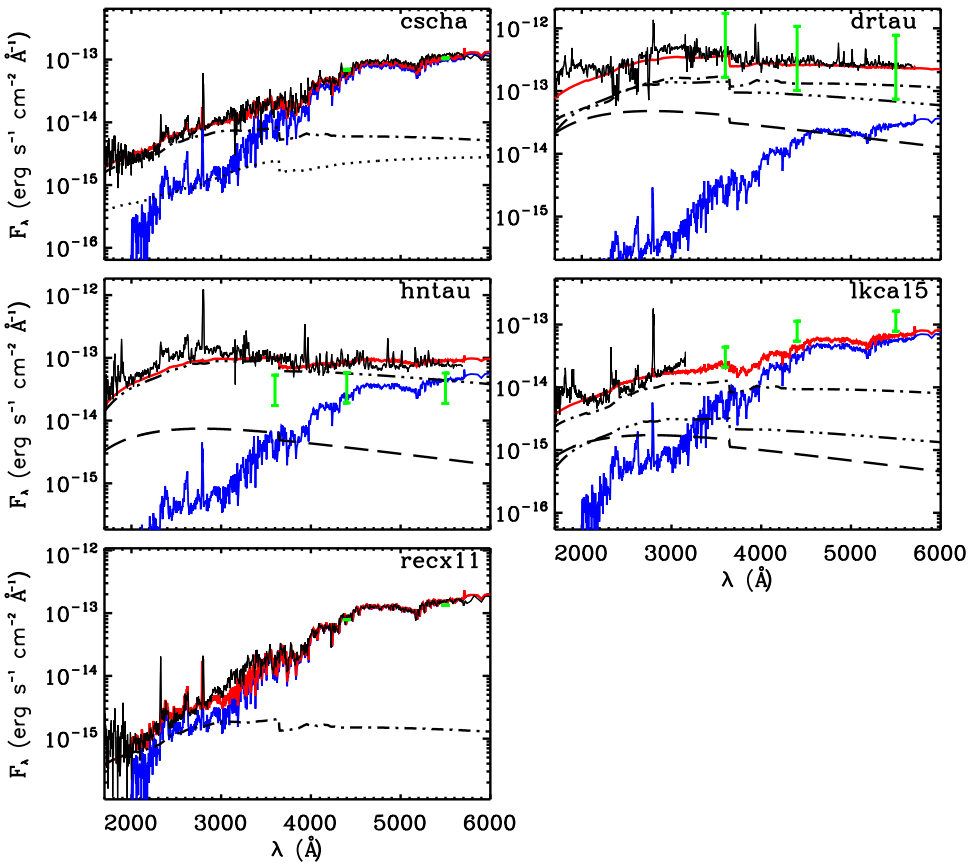

Figure 6.5. Spectra of mid K CTTS in the DAO sample: CS Cha, DR Tau, HN Tau, LkCa 15 and RECX 11. Lines are defined as in Figure 6.4, except the blue spectrum is the WTTS, RECX 1.

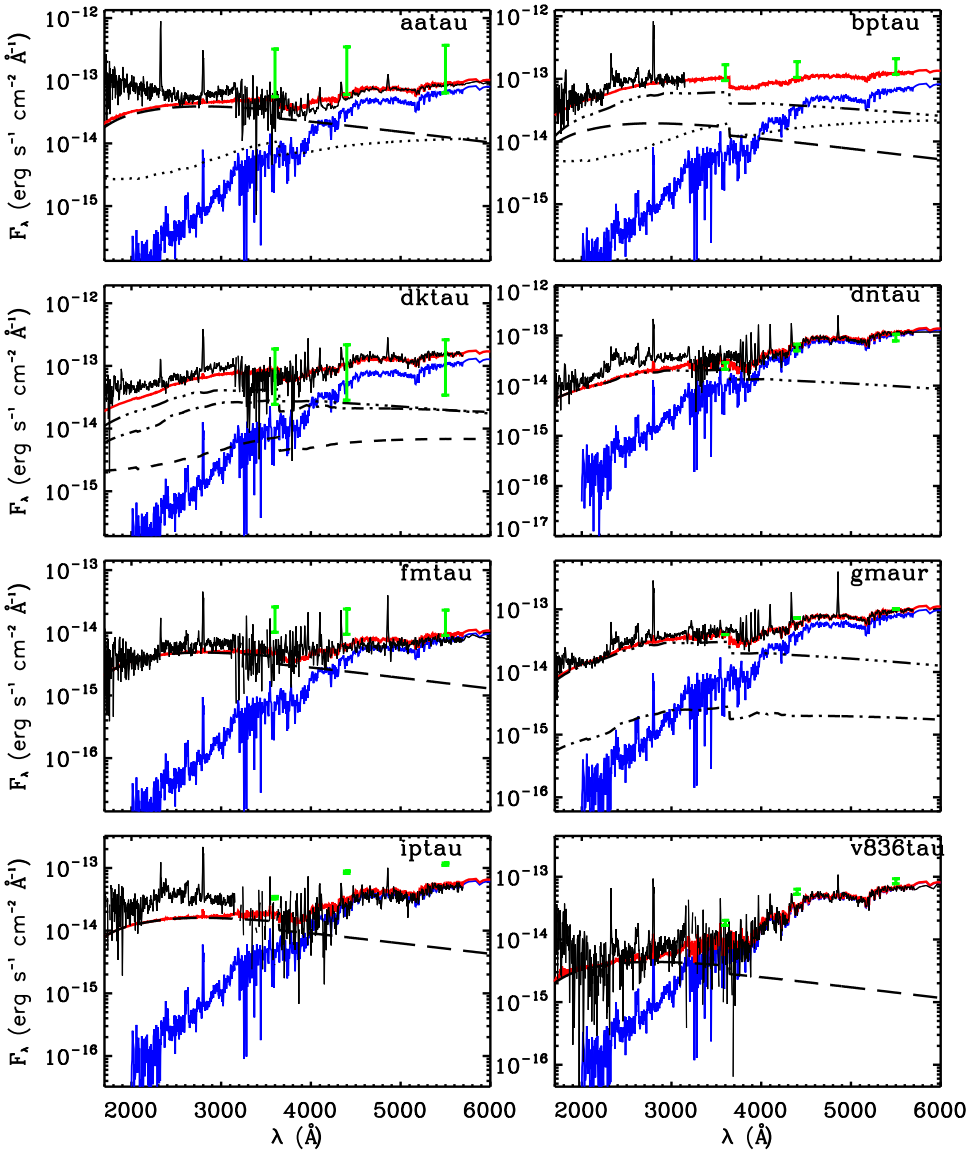

Figure 6.6. Spectra of late K, early M CTTS in the DAO sample: AA Tau, BP Tau, DK Tau, DN Tau, FM Tau, GM Aur, IP Tau and V836 Tau. Lines are defined as in Figure 6.4, except the blue spectrum is the WTTS, HBC 427.

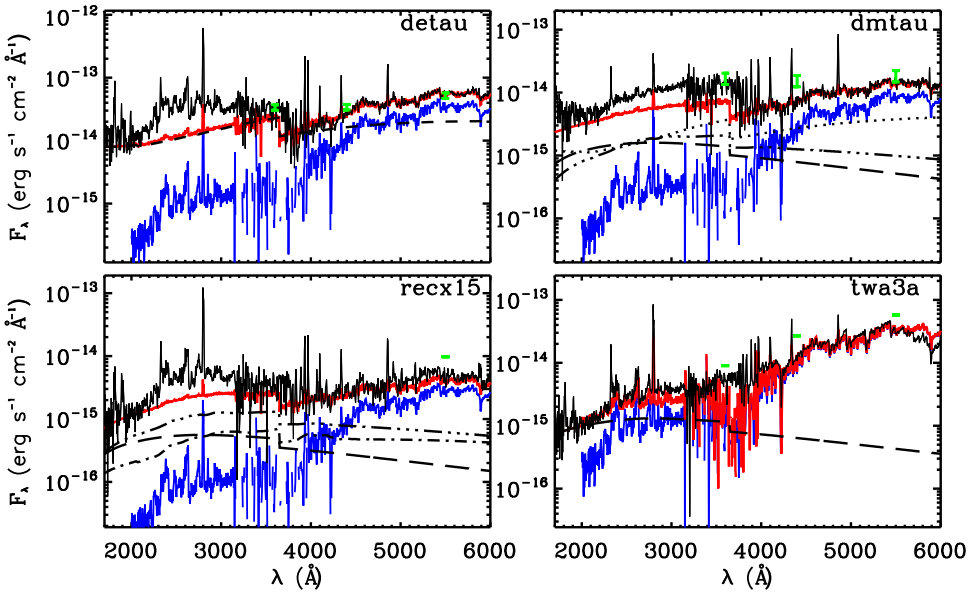

Figure 6.7. Spectra of mid M CTTS in the DAO sample: De Tau, DM Tau, RECX 15 and TWA 3a. Lines are defined as in Figure 6.4, except the blue spectrum is the WTTS, TWA 7.

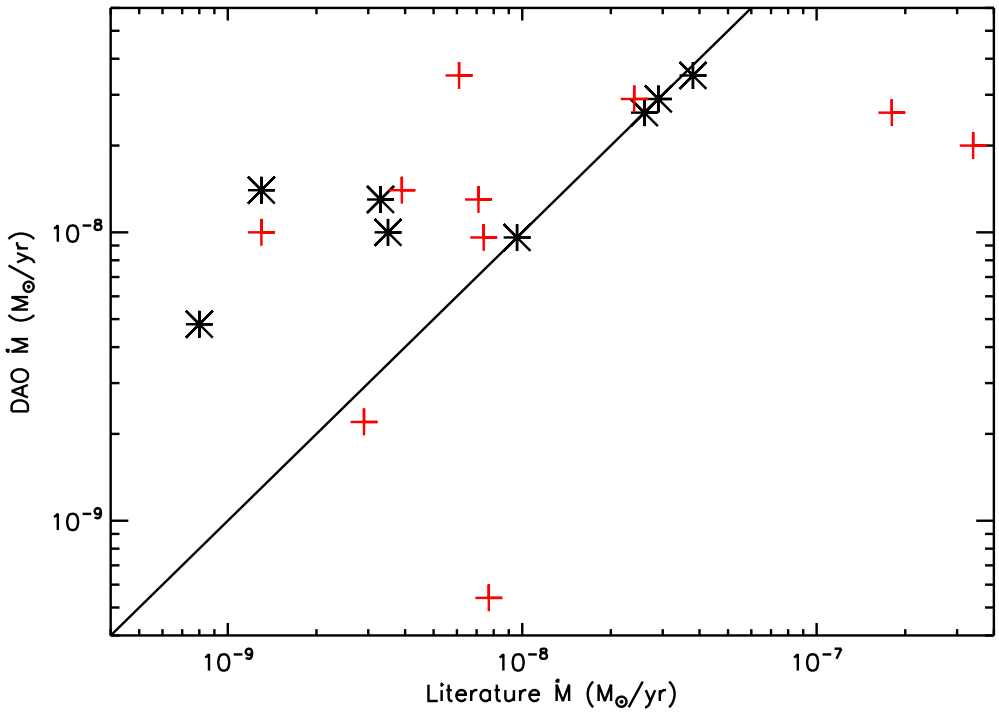

Figure 6.8. DAO accretion rates versus accretion rates from the literature. We compare our estimates of $\dot{M}$ to those from Valenti et al. (1993) in red and Gullbring et al. (1998) in black. Most sources fall on the left of the solid line, where the DAO $\dot{M}$s are higher than those found in the literature.

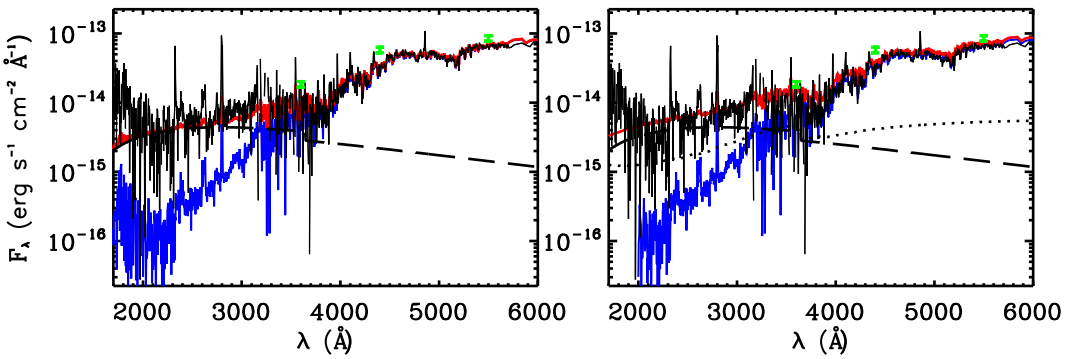

Figure 6.9. Range of possible accretion shock models for V836 Tau. In each panel the lines are defined as in Figure 6.4. The left panel shows the best fit model of the accretion shock to the optical spectra. The right panel shows the fit if we assume that some accretion flux is hidden by the stellar photosphere. The luminosity of the second, low F accretion column (dotted line) is equal to that of the column which fits the NUV excess (long dashed line), doubling $\dot{M}$.

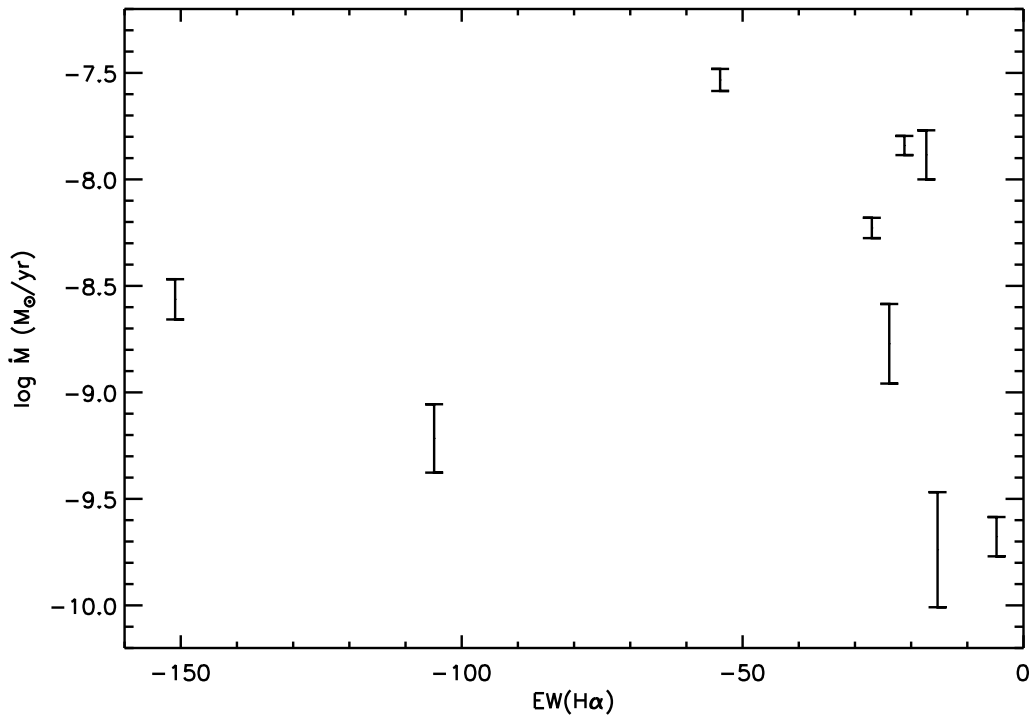

Figure 6.10. $\dot{M}$ versus EW(Hα). We compare the range of $\dot{M}$s given in Table 6.5 to the EW(Hα) measured from the nearly simultaneous SMARTS spectra. We see no correlation between the two.

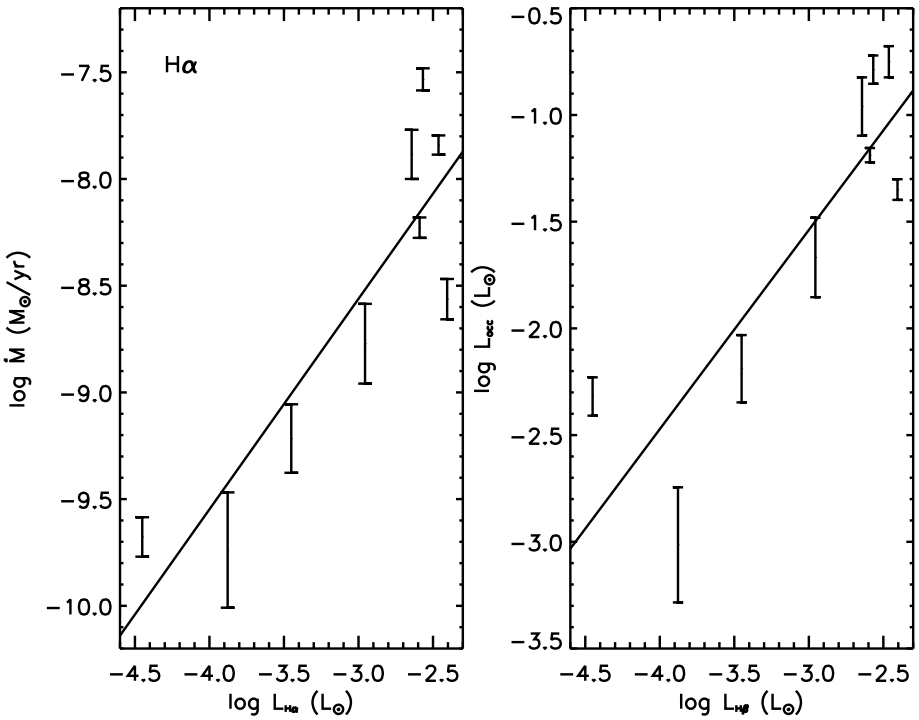

Figure 6.11. $\dot{M}$ and L_{acc} versus Hα line luminosity. The luminosity of Hα, measured in the low resolution SMARTS spectra, is correlated with the accretion properties. The error bars represent the range of $\dot{M}$ from Table 6.5. Fits to the data are given in Equations 6.9 and 6.10.

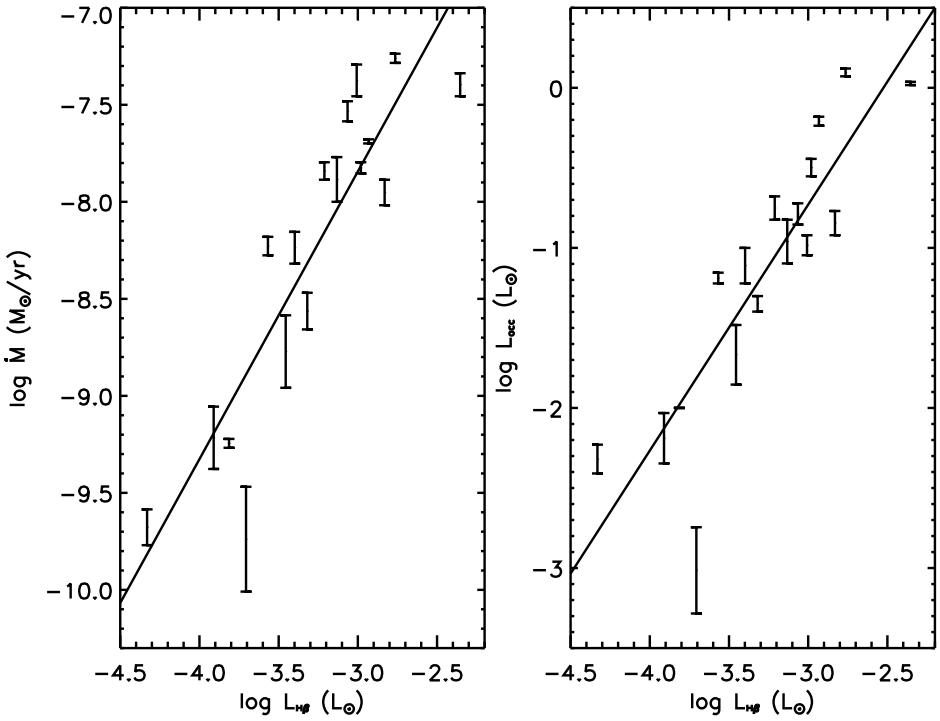

Figure 6.12. $\dot{M}$ and L_{acc} versus Hβ line luminosity. Accretion rates and luminosities are plotted as in Figure 6.11. We measured the luminosity of Hβ from the simultaneous STIS spectra. Hβ clearly traces the accretion properties of the source. Fits to the data are given in Equations 6.11 and 6.12.

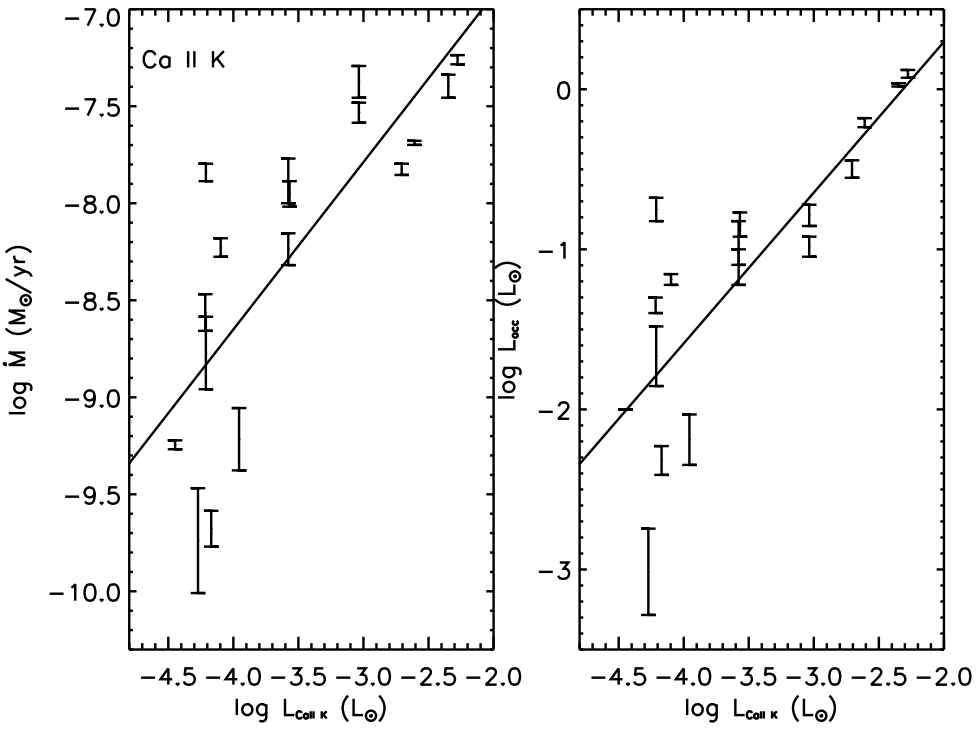

Figure 6.13. $\dot{M}$ and L_{acc} versus the Ca II K line luminosity. Accretion rates and luminosities are plotted as in Figure 6.11. We measured the luminosity of the Ca II K line from the simultaneous STIS spectra. Like the infrared triplet lines of Ca II, the K line luminosity correlates with the accretion properties. Fits to the data are given in Equations 6.13 and 6.14.

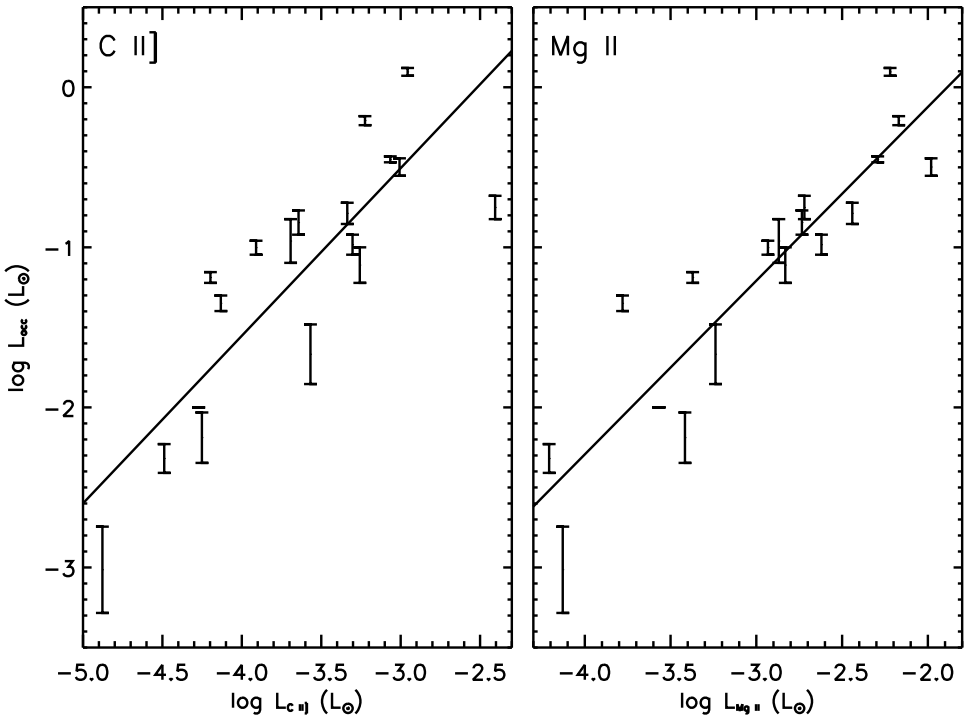

Figure 6.14. Accretion luminosity versus luminosity of NUV emission lines. We compare the luminosity of C II] λ2325 Å (left panel) and Mg II λ2800 Å (right panel) to the range of accretion luminosities calculated from the $\dot{M}$s in Table 6.5. We find strong correlations between both C II] and Mg II and L_{acc}. Fits to the data are given in Equations 6.15 and 6.16.

Table 6.1: Log of DAO Observations

Object	RA (J2000)	DEC (J2000)	Telescope/ Instrument	Date of Obs
AA Tau	04 34 55.42	+24 28 52.8	HST/ STIS G230L/G430L	2011-01-07
			CTIO/ SMARTS RC Spectrograph	2010-12-30
			CTIO/ SMARTS RC Spectrograph	2010-12-31
			CTIO/ SMARTS RC Spectrograph	2011-01-02
			CTIO/ SMARTS RC Spectrograph	2011-01-03
			CTIO/ SMARTS RC Spectrograph	2011-01-04
			CTIO/ SMARTS RC Spectrograph	2011-01-05
BP Tau	04 19 15.86	+29 06 27.2	HST/ STIS G230L	2002-01-12
CS Cha	11 02 25.20	-77 33 36.3	HST/ STIS G230L/G430L	2011-06-01
			CTIO/ SMARTS RC Spectrograph	2011-05-30
			CTIO/ SMARTS RC Spectrograph	2011-05-31
			CTIO/ SMARTS RC Spectrograph	2011-06-02
			Magellan/ MIKE	2012-02-16
CV Cha	11 12 27.65	-76 44 22.1	HST/STIS E230M/G430L	2011-04-13
			CTIO/ SMARTS RC Spectrograph	2011-04-08
			CTIO/ SMARTS RC Spectrograph	2011-04-13
			CTIO/ SMARTS RC Spectrograph	2011-04-15
			CTIO/ SMARTS RC Spectrograph	2011-04-17
			Magellan/ MIKE	2010-03-10
DE Tau	04 21 55.69	+27 55 06.1	HST/ STIS G230L/G430L	2010-08-20
			CTIO/ SMARTS RC Spectrograph	2010-08-15
			CTIO/ SMARTS RC Spectrograph	2010-08-18
			CTIO/ SMARTS RC Spectrograph	2010-08-20
			CTIO/ SMARTS RC Spectrograph	2010-08-21
DK Tau	04 30 44.25	+26 01 24.5	HST/ STIS G230L/G430L	2010-02-04
DM Tau	04 33 48.74	+18 10 09.7	HST/ STIS G230L/G430L	2010-08-22
			CTIO/ SMARTS RC Spectrograph	2010-08-15
			CTIO/ SMARTS RC Spectrograph	2010-08-18
			CTIO/ SMARTS RC Spectrograph	2010-08-20
			CTIO/ SMARTS RC Spectrograph	2010-08-21
			Magellan/ MIKE	2011-01-04

Continued on Next Page...

Table 6.1 – Continued

Object	RA	DEC	Telescope/ Instrument	Date of Obs
DN Tau	04 35 27.44	+24 14 59.1	HST/ STIS G230L/G430L	2011-09-10
			CTIO/ SMARTS RC Spectrograph	2011-09-07
			CTIO/ SMARTS RC Spectrograph	2011-09-09
			CTIO/ SMARTS RC Spectrograph	2011-09-11
DR Tau	04 47 06.22	+16 58 42.6	HST/ STIS G230L/G430L	2010-02-15
FM Tau	04 14 13.56	+28 12 48.8	HST/ STIS G230L/G430L	2011-09-21
			CTIO/ SMARTS RC Spectrograph	2011-09-21
			CTIO/ SMARTS RC Spectrograph	2011-09-27
GM Aur	04 55 10.98	+30 21 59.1	HST/ STIS G230L/G430L	2010-08-19
HBC 427	04 56 02.02	+30 21 03.2	HST/ STIS G230L/G430L	2011-03-30
HN Tau	04 33 39.37	+17 51 52.1	HST/ STIS G230L/G430L	2010-02-10
IP Tau	04 24 57.14	+27 11 56.4	HST/ STIS G230L/G430L	2011-03-21
LkCa 15	04 39 17.73	+22 21 03.8	HST/ STIS G230L	2003-02-13
			Magellan/ MIKE	2011-01-04
LkCa 19	04 55 36.97	+30 17 55.0	HST/ STIS G230L/G430L	2011-03-31
RECX 1	08 36 56.12	-78 56 45.3	HST/ STIS G230L/G430L	2010-01-22
RECX 11	08 47 01.28	-78 59 34.1	HST/ STIS G230L/G430L	2009-12-12
			CTIO/ SMARTS RC Spectrograph	2009-11-26
			CTIO/ SMARTS RC Spectrograph	2009-11-27
			CTIO/ SMARTS RC Spectrograph	2009-12-15
			CTIO/ SMARTS RC Spectrograph	2009-12-19
			CTIO/ SMARTS RC Spectrograph	2009-12-21
			Magellan/ MIKE	2010-03-10
RECX 15	08 43 18.43	-79 05 17.7	HST/ STIS G230L/G430L	2010-02-05
			CTIO/ SMARTS RC Spectrograph	2010-02-01
			CTIO/ SMARTS RC Spectrograph	2010-02-04
			CTIO/ SMARTS RC Spectrograph	2010-02-06
			Magellan/ MIKE	2010-03-11
RW Aur	05 07 49.51	+30 24 04.8	HST/ STIS G230L/G430L	2011-03-25
TWA 3a	11 10 27.80	-37 31 51.2	HST/ STIS G230L/G430L	2011-03-26
			CTIO/ SMARTS RC Spectrograph	2011-03-18
			CTIO/ SMARTS RC Spectrograph	2011-03-22
			CTIO/ SMARTS RC Spectrograph	2011-03-25

Continued on Next Page...

Table 6.1 – Continued

Object	RA	DEC	Telescope/ Instrument	Date of Obs
			CTIO/ SMARTS RC Spectrograph	2011-03-29
			Magellan/ MIKE	2010-03-10
TWA 7	10 42 29.94	-33 40 16.7	HST/ STIS G230L/G430L	2011-05-05
V836 Tau	05 03 06.62	+25 23 19.6	HST/ STIS G230L/G430L	2011-02-05
			CTIO/ SMARTS RC Spectrograph	2011-01-28
			CTIO/ SMARTS RC Spectrograph	2011-02-01
			CTIO/ SMARTS RC Spectrograph	2011-02-03
			CTIO/ SMARTS RC Spectrograph	2011-02-08

Table 6.2: DAO WTTS Properties

Object	A_V mag	Luminosity ($L_\odot$)	Radius ($R_\odot$)	Mass $M_\odot$	SpT
HBC 427	0.0	0.8	1.9	0.8	K7
LkCa 19	1.4	1.7	1.6	1.3	K0
RECX 1	0.0	1.0	1.8	0.9	K5
TWA 7	0.0	0.5	1.8	0.5	M1

Table 6.3: DAO CTTS Properties

Object	SpT	A_V	Luminosity ($L_\odot$)	Radius ($R_\odot$)	Mass ($M_\odot$)	Distance (pc)	r_V	r_Y
AA Tau	K7	1.9	1.0	2.1	0.8	140	0.3	0.2
BP Tau	K7	1.1	1.0	2.1	0.8	140	0.7	0.3
CS Cha	K6	0.3	1.9	2.7	0.9	160	0.2	–
CV Cha	G9	1.5	3.1	2.0	1.5	160	1.4	–
DE Tau	M2	0.9	0.8	2.4	0.4	140	0.6	0.2
DK Tau	K7	1.3	1.6	2.6	0.7	140	0.5	0.5
DM Tau	M1	0.7	0.2	1.1	0.5	140	0.7	–
DN Tau	M0	0.9	1.5	2.8	0.6	140	0.1	0.0
DR Tau	K5	1.4	0.4	1.1	0.9	140	8.1	2.0
FM Tau	M0	0.7	0.1	0.7	0.6	140	–	–
GM Aur	K7	0.6	1.2	2.3	0.8	140	0.2	0.0
HN Tau	K5	1.1	0.7	1.5	1.1	140	0.8	0.5
IP Tau	M0	1.7	0.7	1.9	0.6	140	–	–
LkCa 15	K5	1.1	0.8	1.6	1.1	140	0.2	–
RECX 11	K5	0.0	0.6	1.4	1.0	97	0.0	–
RECX 15	M3	0.0	0.1	0.9	0.3	97	0.8	–
RW Aur	K3	0.5	0.5	1.1	0.9	140	2.0	0.9
TWA 3a	M3	0.0	0.4	1.8	0.3	50	0.0	–
V836 Tau	K7	1.5	1.0	2.1	0.8	140	0.0	0.0

Note: A_V and SpT references: AA Tau, BP Tau, DE Tau, DN Tau, DR Tau, FM Tau, GM Aur, HN Tau, IP Tau, LkCa 15, RW Aur and V836 Tau (Furlan et al., 2011); DK Tau, DM Tau, CS Cha and CV Cha (Furlan et al., 2009); RECX 11 and RECX 15 (Luhman & Steeghs, 2004); TWA 3a (Webb et al., 1999)

Table 6.4: Filling Factors for Multi-Component Model

Object	$f(10^{10})$	$f(3\times10^{10})$	$f(10^{11})$	$f(3\times10^{11})$	$f(10^{12})$
AA Tau	0.05	0	0	0	0.001
BP Tau	0.09	0	0	0.008	0.0007
CS Cha	0.008	0	0.003	0	0
CV Cha	0.45	0.20	0	0	0
DE Tau	0	0.04	0	0	0
DK Tau	0	0.009	0.009	0.004	0
DM Tau	0.08	0	0	0.001	0.0002
DN Tau	0	0	0	0.002	0
DR Tau	0	0	0.3	0.07	0.006
FM Tau	0	0	0	0	0.002
GM Aur	0	0	0.001	0.003	0
HN Tau	0	0	0	0.02	0.0005
IP Tau	0	0	0	0	0.0007
LkCa 15	0	0	0.01	0.0007	0.0001
RECX 11	0	0	0.001	0	0
RECX 15	0	0	0.0009	0.0004	5×10^{-5}
RW Aur	0	0.2	0.09	0.02	0
TWA 3a	0	0	0	0	8×10^{-6}
V836 Tau	0	0	0	0	0.0002

Table 6.5: Accretion Rates for the DAO Sample

Object	WTTS	$\dot{M}^a$ ($M_\odot\,yr^{-1}$)	f^a	$\dot{M}^b_{max}$ ($M_\odot\,yr^{-1}$)	f^b_{max}
AA Tau	HBC 427	1.3×10^{-8}	0.05	–	–
BP Tau	HBC 427	2.9×10^{-8}	0.10	–	–
CS Cha	RECX 1	5.3×10^{-9}	0.01	–	–
CV Cha	LkCa 19	3.5×10^{-8}	0.65	–	–
DE Tau	TWA 7	2.6×10^{-8}	0.04	–	–
DK Tau	HBC 427	3.5×10^{-8}	0.02	–	–
DM Tau	TWA 7	2.2×10^{-9}	0.08	–	–
DN Tau	HBC 427	1.0×10^{-8}	0.002	$\leq 1.7\times10^{-8}$	≤ 0.06
DR Tau	RECX 1	5.2×10^{-8}	0.37	–	–
FM Tau	HBC 427	5.4×10^{-10}	0.002	$\leq 6.0\times10^{-10}$	≤ 0.02
GM Aur	HBC 427	9.6×10^{-9}	0.004	$\leq 1.3\times10^{-8}$	≤ 0.04
HN Tau	RECX 1	1.4×10^{-8}	0.02	–	–
IP Tau	HBC 427	4.8×10^{-9}	0.0007	$\leq 7.0\times10^{-9}$	≤ 0.03
LkCa 15	RECX 1	3.1×10^{-9}	0.01	$\leq 6.0\times10^{-9}$	≤ 0.13
RECX 11	RECX 1	1.7×10^{-10}	0.001	$\leq 2.6\times10^{-10}$	≤ 0.006
RECX 15	TWA 7	4.2×10^{-10}	0.001	$\leq 8.8\times10^{-10}$	≤ 0.03
RW Aur	LkCa 19	2.0×10^{-8}	0.33	–	–
TWA 3a	TWA 7	9.8×10^{-11}	8×10^{-6}	$\leq 3.4\times10^{-10}$	≤ 0.002
V836 Tau	HBC 427	1.1×10^{-9}	0.0002	$\leq 2.6\times10^{-9}$	≤ 0.02

[a] Values which give the best χ^2_{red} fit of the model to the data which also reproduces the observed 1 μm veiling, when known. The filling factors are the sum of the contributions from each column in Table 6.4.

[b] Values calculated when allowing for a low $\mathcal{F}$ column which produces emission not detectable above the intrinsic stellar emission.

CHAPTER 7

Summary and Conclusions

In this thesis, we studied the evolution of pre-main sequence stars by tracing the high energy emission produced in energetic phenomena. We focused on X-ray and UV emission which originate in coronae and chromospheres heated by strong magnetic fields and fast stellar rotation, accretion shocks onto the stellar surface and hot gas in the inner circumstellar disk. During pre-main sequence evolution a young star transitions from a CTTS to a WTTS as accretion ceases and the inner disk gas is depleted. This transition likely occurs during the first 10 Myr, a timescale relevant to disk dispersal and planet formation. Both are strongly influenced by high energy emission which is essential for circumstellar disk evolution, providing the heating mechanism for photoevaporation of disk material and acting as a source of ionization, which is important for inducing magneto-rotational instabilities and driving disk chemistry. After 10 Myr the WTTS spins down as it evolves towards the main sequence, decreasing the heating of the corona and chromosphere, observed as a decline in X-ray and UV radiation. In this chapter, we summarize our results from Chapters 2–6 regarding high energy emission from T Tauri stars and discuss possibilities for future research in this area in Section 7.4.

7.1 Evolution of X-rays and FUV Emission

With new X-ray and FUV observations of young stars we followed the decline in high energy emission for the first 1–100 Myr of pre-main sequence evolution. *Chandra* X-ray observations of the well populated, 7–10 Myr, 25 Ori stellar aggregate confirmed previous results from Mercer et al. (2009) that the X-ray emission remains

constant for the first 10 Myr (Section 2.3), beginning its decay between 10 and 30 Myr. A new, large sample of FUV spectra of T Tauri stars and debris disks revealed a similar decline in FUV emission with age. Our sample included both accreting and non-accreting sources and therefore, many had contributions to the FUV from the accretion shock and circumstellar H_2. There is a large range in FUV luminosities for a given age because there is a similarly large scatter in accretion luminosities for sources of the same age (Calvet et al., 2005), with the FUV luminosity of the accreting sources always exceeding that of the WTTS and debris disks. In Section 4.4, we increased our FUV sample to include observations of 12 young (1–3 Myr) WTTS, used to establish the FUV contribution of the chromosphere alone. The FUV emission appears to saturate around 10 Myr, like the X-ray emission; however, there is a significant spread in the measured luminosities for the small number of sources, making this analysis difficult. If the same mechanism is heating both the chromosphere and corona, which seems likely based on correlations between tracers of the two (Maggio et al., 1987; Mamajek & Hillenbrand, 2008), then it would be reasonable to assume that X-rays and FUV saturate at the same age. It is important to note that although the X-ray emission for a population is saturated, individual objects will still exhibit variability due to stellar flares, for an example (Stelzer et al., 2000).

While the reason for X-ray (and FUV) saturation is not completely understood, the eventual decline occurs as the rotation period of the source increases (Preibisch et al., 2005). The drop in short wavelength radiation for stars as they evolve towards and even along the main sequence was shown by Ribas et al. (2005) who found that the decay for > 1 Gyr solar type stars followed a power law. We compared the expected emission from their power laws to X-ray and FUV emission for 10–100 Myr G type debris disks in nearby star forming regions (Section 2.4) and found that the Ribas et al. (2005) predictions provided a reasonable fit to our observations of much younger stars. Therefore, the dimming of high energy radiation appears to transition smoothly from the T Tauri to main sequence phases of stellar evolution, with the rate of decline described by a constant power law.

7.2 Dissipation of Circumstellar H_2

Due to the difficulty of observing circumstellar gas, dust emission has been used to study the evolution and removal of disk material thus far (Dullemond & Dominik, 2004; D'Alessio et al., 2006; Dutrey et al., 2008). Although a lot can be learned from the dust, the gas comprises the majority of the mass of the disk, and much of the gas is in H_2. In Chapter 3 we showed that FUV spectra of T Tauri stars, even at low resolution, provide crucial information regarding H_2 in the disk, very close to the star. We compared the H_2 emission properties between sources with full disks and those with no evidence for a disk, as traced by the dust, which also covered a variety of accretion properties. The data showed that the H_2 is dissipated from the inner disk when sources have reached the debris disk stage of dust evolution. We also found that H_2 is not detected when a source is no longer accreting. As the X-ray emission necessary to produce an H_2 feature near 1600 Å is present in all young stars this indicates that it is likely the complete dissipation of the inner disk which eventually halts magnetospheric accretion.

In Chapter 4 we included young (1–3) Myr WTTS to search for the last traces of gas in circumstellar disks. The spectra had no evidence for remaining H_2, indicating that some young stars get rid of their entire disks in very short timescales. This is important for studies of planet formation, because it shows that some disks (up to 20%) do not last more than 1 Myr, limiting the time available for planets to form (Hernández et al., 2008). It is likely that these disks are telling us something about the initial conditions of star formation, perhaps the angular momentum distribution of molecular cloud cores, as cores with very low angular momenta may form geometrically small disks (Hartmann, 2009). Disks with small radii will accrete quickly onto the star, within the 1–3 Myr timescale of the young WTTS.

7.3 Characterization of Accretion at Different Stages

In Chapter 6 we analyzed the accretion properties of a large sample of T Tauri stars, ranging in $\dot{M}$ from 10^{-11} to 10^{-7} $M_\odot\,yr^{-1}$. The dataset included simultaneous FUV

through optical spectra, necessary because T Tauri stars are known to be variable (Herbst et al., 1994). These accretion rates were derived using appropriate stellar templates, WTTS, instead of dwarf stars which have been used in the past because they are more readily available. We fit the spectra using the Calvet & Gullbring (1998) treatment of the emission from the accretion columns, which accurately describes the UV excess, but as a next-order approximation, we allow for multiple accretion components. Including the emission from accretion columns with different energy fluxes is motivated both by models which describe the geometry of the magnetosphere (Donati et al., 2008; Gregory & Donati, 2011) and observations of a red wavelength excess (Edwards et al., 2006; Fischer et al., 2011). Models predict that the accretion footprints of complex field geometries will have a variety of filling factors and densities. We assume columns with different energy fluxes, defined as $\mathcal{F} = (1/2)\rho v_s^3$, where v_s is approximately the free fall velocity, represent accretion spots with a range of densities (ρ). A major impact of this addition to the models is that filling factors are much larger than in the initial models which fit the UV excess alone. Low $\mathcal{F}$ columns which peak at redder wavelengths have large filling factors, $\sim$10%, similar to those predicted by the magnetospheric geometry models (Romanova et al., 2012). When calculating $\dot{M}$, two new assumptions in our treatment offset; 1) using the WTTS stellar template which has a UV excess compared to a dwarf star reduces the UV shock excess, while 2) fitting the observed red excess with low $\mathcal{F}$ columns increases the shock emission.

In Chapter 5, we focused on one source from Chapter 6 with a very low $\dot{M}$, RECX-11, to explore accretion at the final stages. Several accretion indicators, like the Ca II infrared triplet lines, the O I λ6300 Å accretion-related wind diagnostic and even the NUV excess, which reveal ongoing accretion at high $\dot{M}$ do not work at low $\dot{M}$. High resolution and multi-epoch observations of Hα and He I λ10830Å do provide the needed evidence, displaying complex and variable accretion features. In addition, FUV observations of H_2 in the disk are sensitive to remaining inner disk gas, which we have shown to be linked to ongoing accretion. With confirmed accretion, we estimate the upper limit on the mass accretion rate as 3×10^{-10} $M_\odot\,yr^{-1}$. RECX-11 has no indication of a gap or hole in the circumstellar disk, so it is unlikely

that photoevaporation is occurring at rates predicted by X-ray and FUV models, up to 10^{-8} $M_\odot\,yr^{-1}$ (Owen et al., 2010; Gorti et al., 2009; Gorti & Hollenbach, 2009). Even considering the "photoevaporation- starved accretion" discussed in Owen et al. (2012b), where the mass accretion rate may drop to an order of magnitude below the mass loss rate for a brief period of time before the disk gap opens, the upper limit on the accretion rate of RECX-11 is still well below 10^{-9} $M_\odot\,yr^{-1}$ and contradicts predicted high mass losses. Using low accretion rate objects, like RECX-11, we can provide constraints on mass loss rates that may be eroding the circumstellar disk.

7.4 Directions for Future Observations and Theory

There are still considerable advances to be made in understanding the evolution of circumstellar disk gas and its relation to high energy processes in pre-main sequence objects. For one, the evolution of the non-accretion related contributions to the UV should be better constrained, and is important for understanding the chromosphere as a source spins down. Cardini & Cassatella (2007) showed that Mg II near 2800 Å, a tracer of chromospheric activity, is saturated for sources <300 Myr, but it appears that the FUV emission drops somewhere after 10 Myr; a bigger sample of FUV spectra is needed to confirm whether continuum and line tracers saturate at different ages. Right now this analysis is limited by the dearth of FUV observations of WTTS, especially high resolution observations. UV photons are easily absorbed and therefore it is difficult to detect weak UV emission from WTTS; however, the nearest and brightest are observable with COS.

Perhaps the most important unknown in theories of circumstellar disk chemistry is the Lyα radiation. Lyα may be up to 80% of the total FUV luminosity, but is difficult to observe. The best attempt to constrain the shape of the Lyα emission line uses H_2 emission lines produced by Lyα fluorescence of H_2 to reconstruct the Lyα fluxes that were seen by the disk. So far, only one Lyα profile has been reconstructed from H_2 observations, and that is of TW Hya (Herczeg et al., 2002). However, absorption at wavelengths corresponding to H_2 transitions were observed against the Lyα line profiles of DF Tau and V4046 Sgr (Yang et al., 2011), so there are good prospects

for probing the variety of Lyα profiles irradiating the disk, especially with the DAO sample which covers a large variety of accretion properties.

In this thesis, we used low resolution FUV spectra in an attempt to ascertain properties of hot gas in the inner circumstellar disk, but the ACS/SBC prism spectra provided very limited information. Ideally the combination of high resolution FUV spectra and models of the emission from hot molecular gas will provide temperatures and densities of gas in the inner disk, in addition to masses of the gas with those parameters. With large samples of FUV spectra from STIS or COS, we will be able to follow the properties of the gas through disk evolution, similar to what has been done for the dust. The high resolution FUV spectra of few sources have been modeled so far (France et al., 2011, 2012), but the number is increasing with the DAO sample.

To understand the different timescales of disk evolution, more young WTTS should be studied at UV and X-ray wavelengths. As shown by Hernández et al. (2007b), IR tracers of circumstellar dust are not observed in all of the stars in the youngest star forming regions; up to 20% of sources appear to have no disks at <1 Myr (Lada et al., 2000). Currently, we have confirmed that gas is completely gone in the disks of only twelve 1–3 Myr Taurus and Chamaeleon I WTTS, using sensitive FUV tracers of H_2. Further studies are needed to confirm that we are not missing small quantities of remaining gas (or accretion) which is not detectable above the stellar emission for sources which show some dust clearing but do not have accretion detected. These observations will provide constraints to models of the early stages of star formation, including the formation of young WTTS. We suggested one mechanism to get rid of a circumstellar disk quickly, by forming young stars from clouds with low angular momenta, but there are additional possibilities, for example dynamical interactions, possibly due to a companion (Bate et al., 2003; Armitage et al., 2003), photoevaporation from the central star or external radiation by nearby hot stars (Adams et al., 2004).

With the aging of *HST* and no solid plans for future UV space missions, it is important to accumulate as much UV data of young stars as possible now. The ongoing study of dust and cool molecules is promising given the advent of the Atacama

Large Millimeter Array (ALMA) and the James Web Space Telescope (JWST) but the complete picture (dust + hot gas and accretion) cannot be completed without UV and X-ray observations. An important result that will come from the DAO and similar samples are correlations between accretion rates or luminosities and accretion proxies, like Hα, Hβ and the Ca II lines. These will be necessary when the space based UV observations are not possible and studies of young stars are limited to optical or IR spectra. Perhaps key to our understanding of young stars will be similar proxies for the coronal and chromospheric contributions, as access to X-ray and FUV instruments becomes increasingly competitive. Examples of chromospheric proxies include the Ca II H and K lines in the optical; calibrating these lines with the observed UV excess produced in the active chromosphere of WTTS may provide an estimate of that excess when no UV observations are available. With accurate correlations between properties of high energy processes and easily accessible tracers, large samples of young stars with observed accretion and heated chromospheric/ coronal indicators may be accumulated quickly to advance our understanding of these processes.

BIBLIOGRAPHY

Abgrall, H., Roueff, E., Liu, X., & Shemansky, D. E. 1997, ApJ, 481, 557

Adams, F. C., Hollenbach, D., Laughlin, G., & Gorti, U. 2004, ApJ, 611, 360

Adams, F. C., Lada, C. J., & Shu, F. H. 1987, ApJ, 312, 788

Adams, F. C., & Shu, F. H. 1985, ApJ, 296, 655

Agnor, C. B., & Ward, W. R. 2002, ApJ, 567, 579

Alcala, J. M., Terranegra, L., Wichmann, R., et al. 1996, A&AS, 119, 7

Alcalá, J. M., Spezzi, L., Chapman, N., et al. 2008, ApJ, 676, 427

Alencar, S. H. P., Bouvier, J., Walter, F. M., et al. 2012, A&A, 541, A116

Alexander, R. D., & Armitage, P. J. 2007, MNRAS, 375, 500

Alexander, R. D., Clarke, C. J., & Pringle, J. E. 2005, MNRAS, 358, 283

—. 2006, MNRAS, 369, 229

Allen, A., Li, Z.-Y., & Shu, F. H. 2003, ApJ, 599, 363

Andrews, S. M., & Williams, J. P. 2005, ApJ, 631, 1134

Ardila, D. R., Basri, G., Walter, F. M., Valenti, J. A., & Johns-Krull, C. M. 2002, ApJ, 566, 1100

Ardila, D. R., & Johns-Krull, C. M. 2009, in American Institute of Physics Conference Series, Vol. 1094, American Institute of Physics Conference Series, ed. E. Stempels, 309–312

Argiroffi, C., Flaccomio, E., Bouvier, J., et al. 2011, A&A, 530, A1

Armitage, P. J. 2011, ARA&A, 49, 195

Armitage, P. J., Clarke, C. J., & Palla, F. 2003, MNRAS, 342, 1139

Arnaud, K. A. 1996, in Astronomical Society of the Pacific Conference Series, Vol. 101, Astronomical Data Analysis Software and Systems V, ed. G. H. Jacoby & J. Barnes, 17

Artymowicz, P., & Lubow, S. H. 1994, ApJ, 421, 651

Bary, J. S., Weintraub, D. A., Shukla, S. J., Leisenring, J. M., & Kastner, J. H. 2008, ApJ, 678, 1088

Bate, M. R., Bonnell, I. A., & Bromm, V. 2003, MNRAS, 339, 577

Bergin, E., Calvet, N., D'Alessio, P., & Herczeg, G. J. 2003, ApJ, 591, L159

Bergin, E., Calvet, N., Sitko, M. L., et al. 2004, ApJ, 614, L133

Beristain, G., Edwards, S., & Kwan, J. 2001, ApJ, 551, 1037

Bernstein, R., Shectman, S. A., Gunnels, S. M., Mochnacki, S., & Athey, A. E. 2003, in Society of Photo-Optical Instrumentation Engineers (SPIE) Conference Series, Vol. 4841, Society of Photo-Optical Instrumentation Engineers (SPIE) Conference Series, ed. M. Iye & A. F. M. Moorwood, 1694–1704

Bethell, T., & Bergin, E. 2009, Science, 326, 1675

Bitner, M. A., Richter, M. J., Lacy, J. H., et al. 2008, ApJ, 688, 1326

Bohlin, R. 2007

Bouvier, J., Alencar, S. H. P., Boutelier, T., et al. 2007, A&A, 463, 1017

Brandeker, A., Jayawardhana, R., Khavari, P., Haisch, Jr., K. E., & Mardones, D. 2006, ApJ, 652, 1572

Briceño, C., Calvet, N., Hernández, J., et al. 2005, AJ, 129, 907

Briceño, C., Hartmann, L., Hernández, J., et al. 2007, ApJ, 661, 1119

Briceño, C., Vivas, A. K., Calvet, N., et al. 2001, Science, 291, 93

Briceno, C., Hartmann, L. W., Stauffer, J. R., et al. 1997, AJ, 113, 740

Brickhouse, N. S., Cranmer, S. R., Dupree, A. K., Luna, G. J. M., & Wolk, S. 2010, ApJ, 710, 1835

Briggs, K. R., & Pye, J. P. 2003, MNRAS, 345, 714

Byrne, P. B., & Doyle, J. G. 1989, A&A, 208, 159

Calvet, N., Briceño, C., Hernández, J., et al. 2005, AJ, 129, 935

Calvet, N., D'Alessio, P., Hartmann, L., et al. 2002, ApJ, 568, 1008

Calvet, N., & Gullbring, E. 1998, ApJ, 509, 802

Calvet, N., Hartmann, L., Kenyon, S. J., & Whitney, B. A. 1994, ApJ, 434, 330

Calvet, N., Muzerolle, J., Briceño, C., et al. 2004, AJ, 128, 1294

Cardini, D., & Cassatella, A. 2007, ApJ, 666, 393

Carmona, A., van den Ancker, M. E., Henning, T., et al. 2007, A&A, 476, 853

Carpenter, J. M., Bouwman, J., Silverstone, M. D., et al. 2008, ApJS, 179, 423

Carpenter, J. M., Bouwman, J., Mamajek, E. E., et al. 2009, ApJS, 181, 197

Carr, J. S., & Najita, J. R. 2008, Science, 319, 1504

Chen, C. H., Patten, B. M., Werner, M. W., et al. 2005, ApJ, 634, 1372

Clarke, C. J., Gendrin, A., & Sotomayor, M. 2001, MNRAS, 328, 485

Cranmer, S. R. 2009, ApJ, 706, 824

Currie, T. M. 2008, PhD thesis, University of California, Los Angeles

D'Alessio, P., Calvet, N., Hartmann, L., Franco-Hernández, R., & Servín, H. 2006, ApJ, 638, 314

D'Alessio, P., Calvet, N., Hartmann, L., Lizano, S., & Cantó, J. 1999, ApJ, 527, 893

Danforth, C. W., Keeney, B. A., Stocke, J. T., Shull, J. M., & Yao, Y. 2010, ApJ, 720, 976

Dib, S., Hennebelle, P., Pineda, J. E., et al. 2010, ApJ, 723, 425

Dickey, J. M., & Lockman, F. J. 1990, ARA&A, 28, 215

Donati, J.-F., Jardine, M. M., Gregory, S. G., et al. 2008, MNRAS, 386, 1234

Dullemond, C. P., & Dominik, C. 2004, A&A, 421, 1075

—. 2005, A&A, 434, 971

Dullemond, C. P., & Monnier, J. D. 2010, ARA&A, 48, 205

Dupree, A. K., Brickhouse, N. S., Cranmer, S. R., et al. 2012, ApJ, 750, 73

Dutrey, A., Guilloteau, S., Piétu, V., et al. 2008, A&A, 490, L15

Edwards, S., Fischer, W., Hillenbrand, L., & Kwan, J. 2006, ApJ, 646, 319

Edwards, S., Hartigan, P., Ghandour, L., & Andrulis, C. 1994, AJ, 108, 1056

Eisner, J. A. 2012, ArXiv e-prints

Ercolano, B., Clarke, C. J., & Hall, A. C. 2011, MNRAS, 410, 671

Ercolano, B., Drake, J. J., Raymond, J. C., & Clarke, C. C. 2008, ApJ, 688, 398

Espaillat, C. 2009, PhD thesis, University of Michigan

Espaillat, C., Calvet, N., D'Alessio, P., et al. 2007, ApJ, 670, L135

Espaillat, C., Muzerolle, J., Hernández, J., et al. 2008, ApJ, 689, L145

Espaillat, C., D'Alessio, P., Hernández, J., et al. 2010, ApJ, 717, 441

Evans, II, N. J. 1999, ARA&A, 37, 311

Fedele, D., van den Ancker, M. E., Henning, T., Jayawardhana, R., & Oliveira, J. M. 2010, A&A, 510, A72

Feigelson, E. D., Broos, P., Gaffney, III, J. A., et al. 2002, ApJ, 574, 258

Feigelson, E. D., Casanova, S., Montmerle, T., & Guibert, J. 1993, ApJ, 416, 623

Feigelson, E. D., Getman, K., Townsley, L., et al. 2005, ApJS, 160, 379

Fernández, R., Brandeker, A., & Wu, Y. 2006, ApJ, 643, 509

Findeisen, K., & Hillenbrand, L. 2010, AJ, 139, 1338

Findeisen, K., Hillenbrand, L., & Soderblom, D. 2011, AJ, 142, 23

Fischer, W., Edwards, S., Hillenbrand, L., & Kwan, J. 2011, ApJ, 730, 73

Fischer, W., Kwan, J., Edwards, S., & Hillenbrand, L. 2008, ApJ, 687, 1117

Font, A. S., McCarthy, I. G., Johnstone, D., & Ballantyne, D. R. 2004, ApJ, 607, 890

France, K., Linsky, J. L., Brown, A., Froning, C. S., & Béland, S. 2010, ApJ, 715, 596

France, K., Schindhelm, E., Burgh, E. B., et al. 2011, ApJ, 734, 31

France, K., Burgh, E. B., Herczeg, G. J., et al. 2012, ApJ, 744, 22

Franchini, M., Morossi, C., & Malagnini, M. L. 1998, ApJ, 508, 370

Fruscione, A., McDowell, J. C., Allen, G. E., et al. 2006, in Society of Photo-Optical Instrumentation Engineers (SPIE) Conference Series, Vol. 6270, Society of Photo-Optical Instrumentation Engineers (SPIE) Conference Series

Furlan, E., Hartmann, L., Calvet, N., et al. 2006, ApJS, 165, 568

Furlan, E., Watson, D. M., McClure, M. K., et al. 2009, ApJ, 703, 1964

Furlan, E., Luhman, K. L., Espaillat, C., et al. 2011, ApJS, 195, 3

Gálvez, M. C., Montes, D., Fernández-Figueroa, M. J., De Castro, E., & Cornide, M. 2009, AJ, 137, 3965

Gauvin, L. S., & Strom, K. M. 1992, ApJ, 385, 217

Getman, K. V., Feigelson, E. D., Broos, P. S., Micela, G., & Garmire, G. P. 2008, ApJ, 688, 418

Gómez de Castro, A. I., & Ferro-Fontán, C. 2005, MNRAS, 362, 569

Gorti, U., Dullemond, C. P., & Hollenbach, D. 2009, ApJ, 705, 1237

Gorti, U., & Hollenbach, D. 2009, ApJ, 690, 1539

Grankin, K. N., Melnikov, S. Y., Bouvier, J., Herbst, W., & Shevchenko, V. S. 2007, A&A, 461, 183

Gregorio-Hetem, J., Lepine, J. R. D., Quast, G. R., Torres, C. A. O., & de La Reza, R. 1992, AJ, 103, 549

Gregory, S. G., & Donati, J.-F. 2011, Astronomische Nachrichten, 332, 1027

Grosso, N., Audard, M., Bouvier, J., Briggs, K. R., & Güdel, M. 2007, A&A, 468, 557

Güdel, M., & Telleschi, A. 2007, A&A, 474, L25

Güdel, M., Briggs, K. R., Arzner, K., et al. 2007, A&A, 468, 353

Gullbring, E., Calvet, N., Muzerolle, J., & Hartmann, L. 2000, ApJ, 544, 927

Gullbring, E., Hartmann, L., Briceno, C., & Calvet, N. 1998, ApJ, 492, 323

Günther, H. M., Schmitt, J. H. M. M., Robrade, J., & Liefke, C. 2007, A&A, 466, 1111

Hartigan, P., Edwards, S., & Ghandour, L. 1995, ApJ, 452, 736

Hartigan, P., Hartmann, L., Kenyon, S., Hewett, R., & Stauffer, J. 1989, ApJS, 70, 899

Hartigan, P., Kenyon, S. J., Hartmann, L., et al. 1991, ApJ, 382, 617

Hartmann, L. 2001, Accretion Processes in Star Formation

—. 2003, ApJ, 585, 398

—. 2009, Accretion Processes in Star Formation: Second Edition (Cambridge University Press)

Hartmann, L., Calvet, N., Gullbring, E., & D'Alessio, P. 1998, ApJ, 495, 385

Hartmann, L., Hewett, R., & Calvet, N. 1994, ApJ, 426, 669

Hartmann, L., Megeath, S. T., Allen, L., et al. 2005, ApJ, 629, 881

Hartmann, L., Schmidtke, P. C., Davis, R., et al. 1979, ApJ, 233, L69

Heap, S. R., & Lindler, D. J. 2007, in Astronomical Society of the Pacific Conference Series, Vol. 374, From Stars to Galaxies: Building the Pieces to Build Up the Universe, ed. A. Vallenari, R. Tantalo, L. Portinari, & A. Moretti, 409

Herbst, W., Herbst, D. K., Grossman, E. J., & Weinstein, D. 1994, AJ, 108, 1906

Herczeg, G. J., & Hillenbrand, L. A. 2008, ApJ, 681, 594

Herczeg, G. J., Linsky, J. L., Valenti, J. A., Johns-Krull, C. M., & Wood, B. E. 2002, ApJ, 572, 310

Herczeg, G. J., Linsky, J. L., Walter, F. M., Gahm, G. F., & Johns-Krull, C. M. 2006, ApJS, 165, 256

Herczeg, G. J., Wood, B. E., Linsky, J. L., Valenti, J. A., & Johns-Krull, C. M. 2004, ApJ, 607, 369

Hernández, J., Briceño, C., Calvet, N., et al. 2006, ApJ, 652, 472

Hernández, J., Calvet, N., Hartmann, L., et al. 2009, ApJ, 707, 705

Hernández, J., Hartmann, L., Calvet, N., et al. 2008, ApJ, 686, 1195

Hernández, J., Morales-Calderon, M., Calvet, N., et al. 2010, ApJ, 722, 1226

Hernández, J., Hartmann, L., Megeath, T., et al. 2007a, ApJ, 662, 1067

Hernández, J., Calvet, N., Briceño, C., et al. 2007b, ApJ, 671, 1784

Higdon, S. J. U., Devost, D., Higdon, J. L., et al. 2004, PASP, 116, 975

Hillenbrand, L. A., Carpenter, J. M., Kim, J. S., et al. 2008, ApJ, 677, 630

Hollenbach, D., Johnstone, D., Lizano, S., & Shu, F. 1994, ApJ, 428, 654

Holmberg, J., Nordström, B., & Andersen, J. 2009, A&A, 501, 941

Houdebine, E. R., Mathioudakis, M., Doyle, J. G., & Foing, B. H. 1996, A&A, 305, 209

Huenemoerder, D. P., Lawson, W. A., & Feigelson, E. D. 1994, MNRAS, 271, 967

Ingleby, L., Calvet, N., Herczeg, G., & Briceño, C. 2012, ApJ, 752, L20

Ingleby, L., Calvet, N., Hernández, J., et al. 2011a, AJ, 141, 127

Ingleby, L., Calvet, N., Bergin, E., et al. 2009, ApJ, 703, L137

—. 2011b, ApJ, 743, 105

Jayawardhana, R., Coffey, J., Scholz, A., Brandeker, A., & van Kerkwijk, M. H. 2006, ApJ, 648, 1206

Johns-Krull, C. M., Valenti, J. A., & Linsky, J. L. 2000, ApJ, 539, 815

Kalas, P., Graham, J. R., Clampin, M. C., & Fitzgerald, M. P. 2006, ApJ, 637, L57

Kalberla, P. M. W., Burton, W. B., Hartmann, D., et al. 2005, A&A, 440, 775

Kastner, J. H., Crigger, L., Rich, M., & Weintraub, D. A. 2003, ApJ, 585, 878

Kastner, J. H., Zuckerman, B., Weintraub, D. A., & Forveille, T. 1997, Science, 277, 67

Kenyon, S. J., & Bromley, B. C. 2006, AJ, 131, 1837

Kenyon, S. J., & Hartmann, L. 1987, ApJ, 323, 714

—. 1995, ApJS, 101, 117

Kim, K. H., Watson, D. M., Manoj, P., et al. 2009, ApJ, 700, 1017

Köhler, R., & Petr-Gotzens, M. G. 2002, AJ, 124, 2899

Kominami, J., & Ida, S. 2002, Icarus, 157, 43

Kraus, A. L., Ireland, M. J., Hillenbrand, L. A., & Martinache, F. 2012, ApJ, 745, 19

Kraus, A. L., Ireland, M. J., Martinache, F., & Hillenbrand, L. A. 2011, ApJ, 731, 8

Kriss, G. A. 2011, Improved Medium Resolution Line Spread Functions for COS FUV Spectra, Tech. rep.

Kurosawa, R., Harries, T. J., & Symington, N. H. 2006, MNRAS, 370, 580

Lada, C. J., Muench, A. A., Haisch, Jr., K. E., et al. 2000, AJ, 120, 3162

Lada, C. J., Muench, A. A., Luhman, K. L., et al. 2006, AJ, 131, 1574

Larsen, S. 2006

Lawson, W. A., Crause, L. A., Mamajek, E. E., & Feigelson, E. D. 2001, MNRAS, 321, 57

Lawson, W. A., Feigelson, E. D., & Huenemoerder, D. P. 1996, MNRAS, 280, 1071

Lawson, W. A., Lyo, A.-R., & Muzerolle, J. 2004, MNRAS, 351, L39

Lima, G. H. R. A., Alencar, S. H. P., Calvet, N., Hartmann, L., & Muzerolle, J. 2010, A&A, 522, A104

López-Santiago, J., Albacete Colombo, J. F., & López-García, M. A. 2010, A&A, 524, A97

Low, F. J., Smith, P. S., Werner, M., et al. 2005, ApJ, 631, 1170

Luhman, K. L. 2004, ApJ, 602, 816

—. 2007, ApJS, 173, 104

Luhman, K. L., Allen, P. R., Espaillat, C., Hartmann, L., & Calvet, N. 2010, ApJS, 186, 111

Luhman, K. L., & Steeghs, D. 2004, ApJ, 609, 917

Luhman, K. L., Allen, L. E., Allen, P. R., et al. 2008, ApJ, 675, 1375

Lyo, A.-R., Lawson, W. A., & Bessell, M. S. 2004, MNRAS, 355, 363

Maggio, A., Sciortino, S., Vaiana, G. S., et al. 1987, ApJ, 315, 687

Mamajek, E. E., & Hillenbrand, L. A. 2008, ApJ, 687, 1264

Mamajek, E. E., Lawson, W. A., & Feigelson, E. D. 1999, ApJ, 516, L77

—. 2000, ApJ, 544, 356

Manoj, P. 2010, in Astronomical Society of the Pacific Conference Series, Vol. 432, New Horizons in Astronomy: Frank N. Bash Symposium 2009, ed. L. M. Stanford, J. D. Green, L. Hao, & Y. Mao, 49

Marshall, J. L., Burles, S., Thompson, I. B., et al. 2008, in Society of Photo-Optical Instrumentation Engineers (SPIE) Conference Series, Vol. 7014, Society of Photo-Optical Instrumentation Engineers (SPIE) Conference Series

Martínez-Arnáiz, R., Maldonado, J., Montes, D., Eiroa, C., & Montesinos, B. 2010, A&A, 520, A79

Mathis, J. S. 1990, ARA&A, 28, 37

Matsuyama, I., Johnstone, D., & Murray, N. 2003, ApJ, 585, L143

McClure, M. K., Furlan, E., Manoj, P., et al. 2010, ApJS, 188, 75

Meijerink, R., Glassgold, A. E., & Najita, J. R. 2008, ApJ, 676, 518

Mercer, E. P., Miller, J. M., Calvet, N., et al. 2009, AJ, 138, 7

Muzerolle, J., Allen, L. E., Megeath, S. T., Hernández, J., & Gutermuth, R. A. 2010, ApJ, 708, 1107

Muzerolle, J., Calvet, N., & Hartmann, L. 1998a, ApJ, 492, 743

—. 2001, ApJ, 550, 944

Muzerolle, J., Hartmann, L., & Calvet, N. 1998b, AJ, 116, 455

Muzerolle, J., Hillenbrand, L., Calvet, N., Briceño, C., & Hartmann, L. 2003, ApJ, 592, 266

Najita, J. R., Ádámkovics, M., & Glassgold, A. E. 2011, ApJ, 743, 147

Najita, J. R., Carr, J. S., Strom, S. E., et al. 2010, ApJ, 712, 274

Najita, J. R., Crockett, N., & Carr, J. S. 2008, ApJ, 687, 1168

Nakajima, T., Morino, J.-I., & Fukagawa, M. 2010, AJ, 140, 713

Natta, A., Testi, L., Muzerolle, J., et al. 2004, A&A, 424, 603

Nguyen, D. C., Brandeker, A., van Kerkwijk, M. H., & Jayawardhana, R. 2012, ApJ, 745, 119

Nguyen, D. C., Jayawardhana, R., van Kerkwijk, M. H., et al. 2009, ApJ, 695, 1648

Owen, J. E., Clarke, C. J., & Ercolano, B. 2012a, MNRAS, 422, 1880

—. 2012b, MNRAS, 422, 1880

Owen, J. E., Ercolano, B., Clarke, C. J., & Alexander, R. D. 2010, MNRAS, 401, 1415

Paardekooper, S.-J., & Mellema, G. 2004, A&A, 425, L9

Padgett, D. L., Cieza, L., Stapelfeldt, K. R., et al. 2006, ApJ, 645, 1283

Pascucci, I., Apai, D., Luhman, K., et al. 2009, ApJ, 696, 143

Pascucci, I., Gorti, U., Hollenbach, D., et al. 2006, ApJ, 651, 1177

Pascucci, I., Sterzik, M., Alexander, R. D., et al. 2011, ApJ, 736, 13

Pinte, C., Woitke, P., Ménard, F., et al. 2010, A&A, 518, L126

Preibisch, T., & Feigelson, E. D. 2005, ApJS, 160, 390

Preibisch, T., Kim, Y.-C., Favata, F., et al. 2005, ApJS, 160, 401

Rayner, J. T., Cushing, M. C., & Vacca, W. D. 2009, ApJS, 185, 289

Rebull, L. M., Hillenbrand, L. A., Strom, S. E., et al. 2000, AJ, 119, 3026

Ribas, I., Guinan, E. F., Güdel, M., & Audard, M. 2005, ApJ, 622, 680

Rigliaco, E., Natta, A., Randich, S., Testi, L., & Biazzo, K. 2011, A&A, 525, A47

Robberto, M., Song, J., Mora Carrillo, G., et al. 2004, ApJ, 606, 952

Roberge, A., Feldman, P. D., Weinberger, A. J., Deleuil, M., & Bouret, J.-C. 2006, Nature, 441, 724

Robitaille, T. P., Whitney, B. A., Indebetouw, R., & Wood, K. 2007, ApJS, 169, 328

Robrade, J., & Schmitt, J. H. M. M. 2006, A&A, 449, 737

Rodriguez, D. R., Bessell, M. S., Zuckerman, B., & Kastner, J. H. 2011, ApJ, 727, 62

Romaniello, M., Robberto, M., & Panagia, N. 2004, ApJ, 608, 220

Romanova, M. M., Ustyugova, G. V., Koldoba, A. V., & Lovelace, R. V. E. 2012, MNRAS, 421, 63

Sacco, G. G., Argiroffi, C., Orlando, S., et al. 2008, A&A, 491, L17

Salyk, C., Pontoppidan, K. M., Blake, G. A., et al. 2008, ApJ, 676, L49

Sargent, B., Forrest, W. J., D'Alessio, P., et al. 2006, ApJ, 645, 395

Shkolnik, E. L., Liu, M. C., Reid, I. N., Dupuy, T., & Weinberger, A. J. 2011, ApJ, 727, 6

Shu, F. H., Adams, F. C., & Lizano, S. 1987, ARA&A, 25, 23

Shu, F. H., Johnstone, D., & Hollenbach, D. 1993, Icarus, 106, 92

Sicilia-Aguilar, A., Hartmann, L. W., Fürész, G., et al. 2006, AJ, 132, 2135

Sicilia-Aguilar, A., Henning, T., & Hartmann, L. W. 2010, ApJ, 710, 597

Sicilia-Aguilar, A., Bouwman, J., Juhász, A., et al. 2009, ApJ, 701, 1188

Siess, L., Dufour, E., & Forestini, M. 2000, A&A, 358, 593

Skrutskie, M. F., Cutri, R. M., Stiening, R., et al. 2006, AJ, 131, 1163

Song, I., Caillault, J.-P., Barrado y Navascués, D., Stauffer, J. R., & Randich, S. 2000, ApJ, 533, L41

Spezzi, L., Alcalá, J. M., Covino, E., et al. 2008, ApJ, 680, 1295

Spitzer, Jr., L., & Tomasko, M. G. 1968, ApJ, 152, 971

Stelzer, B., Neuhäuser, R., & Hambaryan, V. 2000, A&A, 356, 949

Strom, K. M., Strom, S. E., Edwards, S., Cabrit, S., & Skrutskie, M. F. 1989, AJ, 97, 1451

Takeda, G., Ford, E. B., Sills, A., et al. 2007, ApJS, 168, 297

Telleschi, A., Güdel, M., Briggs, K. R., Audard, M., & Palla, F. 2007, A&A, 468, 425

Tody, D. 1993, in Astronomical Society of the Pacific Conference Series, Vol. 52, Astronomical Data Analysis Software and Systems II, ed. R. J. Hanisch, R. J. V. Brissenden, & J. Barnes, 173

Uchida, Y., & Shibata, K. 1984, PASJ, 36, 105

Valenti, J. A., Basri, G., & Johns, C. M. 1993, AJ, 106, 2024

Valenti, J. A., Fallon, A. A., & Johns-Krull, C. M. 2003, ApJS, 147, 305

Valenti, J. A., Johns-Krull, C. M., & Linsky, J. L. 2000, ApJS, 129, 399

Verrier, P. E., & Evans, N. W. 2008, MNRAS, 390, 1377

Voges, W., Aschenbach, B., Boller, T., et al. 1999, A&A, 349, 389

—. 2000, VizieR Online Data Catalog, 9029, 0

Wahhaj, Z., Cieza, L., Koerner, D. W., et al. 2010, ApJ, 724, 835

Walter, F. M. 1999, in Astronomical Society of the Pacific Conference Series, Vol. 158, Solar and Stellar Activity: Similarities and Differences, ed. C. J. Butler & J. G. Doyle, 87

Watson, D. M., Leisenring, J. M., Furlan, E., et al. 2009, ApJS, 180, 84

Webb, R. A., Zuckerman, B., Platais, I., et al. 1999, ApJ, 512, L63

Weidenschilling, S. J. 1997, Icarus, 127, 290

White, R. J., & Basri, G. 2003, ApJ, 582, 1109

White, R. J., & Ghez, A. M. 2001, ApJ, 556, 265

White, R. J., & Hillenbrand, L. A. 2004, ApJ, 616, 998

Whittet, D. C. B., Shenoy, S. S., Clayton, G. C., & Gordon, K. D. 2004, ApJ, 602, 291

Wichmann, R., Schmitt, J. H. M. M., & Hubrig, S. 2003, A&A, 399, 983

Wilking, B. A. 1989, PASP, 101, 229

Woitke, P., Riaz, B., Duchêne, G., et al. 2011, A&A, 534, A44

Wright, N. J., Drake, J. J., Mamajek, E. E., & Henry, G. W. 2011, ApJ, 743, 48

Yang, H., Linsky, J. L., & France, K. 2011, ApJ, 730, L10

Yang, H., Herczeg, G. J., Linsky, J. L., et al. 2012, ApJ, 744, 121

Zhu, Z., Nelson, R. P., Hartmann, L., Espaillat, C., & Calvet, N. 2011, ApJ, 729, 47